SCIENTIFIC NOTEBOOK

by

Stuart A. Stothoff

SCIENTIFIC NOTEBOOK

by

Stuart A. Stothoff

Southwest Research Institute
Center for Nuclear Waste Regulatory Analyses
San Antonio, Texas

August 4, 1998

Initial Entries

Scientific NoteBook: # 163

Issued to: S. A. Stothoff

Issue Date: Tuesday, November 16, 1993

By agreement with the CNWRA QA this NoteBook is to be printed at approximate quarterly intervals. This computerized Scientific NoteBook is intended to address the criteria of CNWRA QAP–001.

Table 0-1: Computing Equipment

Machine Name	Type	OS	Location
sierra.cnwra.swri.edu	Sun SPARC 20	SUNOS 4.1.3_U1	desk Rm A-212, Bldg. 189
sisyphus.cnwra.swri.edu	Sun SPARC 20	SUNOS 4.1.3_U1	network
dopey.cnwra.swri.edu	Sun SPARC 10	SUNOS 4.1.3_U1	network
performer.cnwra.swri.edu	SGI Onyx	IRIX 5.3	network
yosemite.cnwra.swri.edu	SGI Onyx	IRIX 5.3	network
bemore.cnwra.swri.edu	SGI Onyx	IRIX 6.2	network
redwood.cnwra.swri.edu	SGI Indy	IRIX 6.2	network
bigbend.cnwra.swri.edu	Sun Ultra-2	SUNOS 5.5.1	network
scratchy1.cnwra.swri.edu	Sun Ultra-2	SUNOS 5.5.1	network
hornet.cnwra.swri.edu	Sun Ultra-2	SUNOS 5.5.1	network

Contents

List of Figures

List of Tables

1. Ambient Hydrology KTI – Infiltration

Account Number: **20-5708-861**
Collaborators: **Amvrossios Bagtzoglou, Gordon Wittmeyer**
Directories: **$SubRegBreath and as noted**

Objective: Perform detailed analysis of the spatial and temporal distribution of infiltration at Yucca Mountain (YM). A good deal of previous work is documented in the Scientific Notebook for the Subregional Flow and Transport Processes Research Project (subregional project) and various publications under the subregional project and the umbrella of the Iterative Performance Assessment and Performance Assessment Research projects. The research projects were closed out due to reorganization of the NRC and consequently CNWRA; infiltration work is largely being subsumed under the Ambient Hydrology KTI, with some applications possible under the Thermal Effects on Flow KTI in order to examine heating effects on infiltration. Initial efforts in the new project are to be directed towards documenting the work already completed in journal articles. Future work will depend very much on funding and time availability, but several avenues that may be explored include: (i) the impact of matrix-fracture interactions; (ii) watershed-scale modelling, with vegetation and lateral flow accounted for; (iii) geochemical tracer verification; and (iv) "shallow" diversion of infiltration due to the PTn layer.

4/12/98 Documentation of future-climate analog trip.

The following is a nearly verbatim copy of a trip report discussing a visit to potential future-climate analog sites in southern Nevada. The trip took place April 5 through 8, 1998, and was reported by S. Stothoff.

Background and purpose of trip

The majority of work characterizing infiltration at YM has assumed that present-day conditions exist and relatively little work has been performed that addresses infiltration under future climatic conditions. The infiltration model used in the NRC's TPA3 exercises conservatively neglects transpiration. Under current climatic conditions, the atmospheric evaporation demand is so much larger than precipitation that neglecting transpiration provides infiltration estimates that are only moderately conservative. However, under the cooler and moister conditions that are anticipated to

occur in future glacial cycles, neglecting transpiration is expected to have a much more significant impact on infiltration predictions.

An infiltration model incorporates transpiration by specifying total soil-water uptake and the distribution of that uptake with depth. In order to calibrate an infiltration model, it is necessary to identify the vegetation expected for the particular climate and geomorphic environment. Given the expected vegetation, it may be possible to estimate appropriate plant rooting depths and uptake patterns from the literature.

Analogs to YM under future climatic conditions, if found, will be used to calibrate the vegetative patterns used as input to the infiltration model. As information on the hydrologic behavior of the sideslopes at YM is least well characterized of all environments at YM, the washes are the primary analog environment that is sought. Analogs to the caprock environment are also sought, with secondary importance. Analog sites were identified within sight of YM in earlier fieldwork (i.e., the Prow, Shoshone Mountain), but the analogs are not sufficient to characterize the range of climatic and geomorphic environments encountered at YM under a glacial cycle. Additional potential analog locations were identified from topographic maps, geologic maps, and aerial surveys. These locations include Rainier Mesa, on the Nevada Test Site (NTS); Timber Mountain and the North Pahroc Range (both in Lincoln County); the Grapevine Range (near Beatty, NV); and the Montezuma Range (near Goldfield). The current trip assessed the viability of these potential sites for future field work, with particular regard to matching bedrock, soil, vegetation, slope, annual precipitation, and mean air temperature to expected future conditions at YM. It is expected that not all of these characteristics will be matched perfectly.

Summary of activities

The fieldwork was intended to quickly identify potential sites for subsequent follow-up studies in greater depth. It is difficult to characterize soil and bedrock characteristics from aerial surveys, so the primary emphasis for this trip was to identify appropriate soil and bedrock characteristics. A primary criterion was that elevations were generally in the range of 6,000 to 8,000 ft, providing precipitation and temperatures similar to anticipated future climates at YM. After elevation, the next criterion used in screening was to identify formations with densely welded tuffs, which are fairly rare. Appropriate slopes and soil depths were secondary criteria for matching.

Several good analog locations were identified, in the Grapevine Mountains, Timber Mountain, and Rainier Mesa. The North Pahroc Range was found less useful for analog work, while the

Montezuma Range was not investigated due to time constraints.

The geomorphic characteristics of portions of lower Phinney Canyon, in the Grapevine Mountains, are strongly analogous to YM washes, featuring densely welded and quite fractured tuffs, north- and south-facing slopes, and thin soils with plentiful rock shards. The Phinney Canyon site may have slightly lower fracture densities and slightly thicker soils than YM. Ground access requires 4WD vehicles and nearly 1-1/2 hr driving from pavement; however, within the canyon access is equivalent to that obtained in YM washes. Air access is unlimited.

Timber Mountain, north of Hiko in Lincoln County, offers outcrops of moderately welded tuff, nonexistent to shallow soils, and general characteristics strongly reminiscent of the caprock at YM. The soils appear to be developing in situ, with perhaps less æolian component than apparent at YM. Ground access requires 4WD vehicles and 10 mi driving from pavement. The last 1/2 mi was hiked, due to mud and uncertain conditions; it should be possible to move closer later in the year. Moderate hiking (1/2 mi) may be required to visit prime sites. Air access is unlimited.

Rainier Mesa, approximately 1 hr drive north of Gate 100 in the NTS, is capped by moderately welded tuffs strongly reminiscent of Yucca Crest. Below the mesa top, sequences of densely welded to nonwelded tuffs form long slopes reminiscent of the west flank of YM. Soil thicknesses also appear to be similar to YM, although the soils appear to have much greater organic contents. Further, infiltration estimates are available, based on measurements of dripping into the N tunnel. Ground access is on pavement, perhaps with some dirt roads. Unlike the other sites, air access may be limited or unavailable due to NTS restrictions, and camping is not an option, requiring 1-1/2 hr drive to the nearest motel.

The North Pahroc Range, between Hiko and Caliente in Lincoln County, offers north- and south-facing sideslopes at angles similar to YM washes and soils generally similar to YM soils. However, the bedrock is not as densely welded as the Tiva Canyon welded units, thereby is less fractured. Also, the easily accessible slopes are generally at a lower elevation than the other sites, yielding an analog to a warmer and drier future climate than the other sites. Areas with what appears to be densely welded tuff are visible from the road, but access would require extensive hiking on steep terrain. Ground access requires 4WD vehicles, but is better than either Timber Mountain or Phinney Canyon. Air access is unlimited.

Impressions/conclusions

Overall impressions

The trip was useful in identifying analog sites. The trip successfully identified several good analogs for future work, although it is desirable to have additional reconnaissance from the air (particularly at Timber Mountain and Rainier Mesa). Fieldwork will not be possible for some time, however, as snow exists at higher elevations (up to 1 m thicknesses were observed) and soils are frozen.

Juniper and piñon pine are efficient at extracting soil moisture due to the large rooting systems for these plants. Packrat midden studies (Brown et al., 1997) indicate that juniper was present at elevations below 500 m in the Great Basin during the last glacial period (significantly lower than the base of YM). During the visit to Nevada, juniper was found at elevations less than 6,000 ft in some locations but piñon/juniper associations were absent at significantly higher elevations in other locations along the periphery of the NTS and Nellis AFB. If the 6,000-ft elevation represents a representative future-climate analog, both cases with and lacking vegetation should be examined to ascertain whether YM would be expected to have these species present in future conditions.

The presence in April of significant amounts of snow and frozen soil, with snowdrifts of up to 1 m in depth, suggests that it may be important to consider snow when modeling infiltration under future climates. None of the YM infiltration modeling to date has considered snow, as snow is not important at YM under current climatic conditions. Under current conditions, most infiltration occurs during the winter; if the ground is frozen, however, infiltration would be expected to peak when the snow melts. It may be that larger infiltration pulses would occur under such conditions, if the total winter precipitation infiltrated over a few weeks.

Summary of field observations

Timber Mountain

Timber Mountain is located approximately 35 mi northwest of Caliente and 40 mi north of Alamo, in Lincoln County, Nevada. Timber Mountain is located far enough east to significantly attenuate the effects of the Sierra Nevada rain shadow. Ground access to the Timber Mountain site is via a 4WD dirt road proceeding 10 mi northwest from the White River Narrows. Air access is not restricted.

The Shingle Pass Tuff (Tsp) unit, identified as densely welded by du Bray et al. (1987), is of primary interest for analog studies. The Tsp unit, described as pinkish-gray to pale-red-purple by du Bray et al. (1987), is a crystal-rich tuff similar in welding and fracturing to the caprock at YM. The peak of Timber Mountain is 8,600 ft in elevation. Areas with Tsp outcrops range from 6,000 to 8,100 ft in elevation, with the most accessible areas (within 1/2 mi of the roadway) roughly 6,600 to 7,000 ft in elevation. Areas outside this range in elevation would require hiking several miles, although the hiking does not appear to be strenuous. A northeast-southwest trending ridge, at approximately latitude 37° 57'30" N and longitude 115° 5' W, appears to be a good analog site for the YM crest.

Soils in the Tsp outcrop areas are thin to nonexistent. Much of the soil appears to be forming in situ, and first impressions suggest that a smaller æolian component is present than at YM. Frost heave is evident in spots. Traces of overland sheet flow were also observed. Plentiful piñon and juniper are present.

North Pahroc Range (Boundary Wash)

The Pahroc area is also in Lincoln County. The North and South Pahroc Ranges are separated by US Route 93 approximately 25 mi west of Caliente. The primary ground access to higher elevations in the Pahroc ranges is through Boulder Wash Road, a 4WD road cutting through the North Pahroc Range from Dry Lake Valley to White River Narrows roughly 25 mi southwest of Timber Mountain. Accessible areas are all less than 7,000 ft in elevation, with the roadway less than 6,000 ft in elevation. Air access is unlimited.

Sideslopes north and east of the roadway feature moderately welded crystal-rich tuffs, and slopes that are generally shallower than the washes at YM. Two types of bedrock were observed within 1/4 mi of the road, a pale lavender tuff and a reddish-brown tuff, with the reddish-brown tuff appearing more welded and more suitable for future work. Fractures appear to be more widely spaced than the Tiva Canyon welded (TCw) unit at YM. Soils appear to be fairly comparable to those at YM. Appearing and disappearing streams where soil pinches out were observed, providing evidence of downslope lateral subsurface flow. Juniper were present, but much more sparsely than at Timber Mountain. Ground access to the base of the slopes is easy, but significant uphill hiking is required to reach higher elevations.

A bowl at higher elevations was noted south of Boundary Wash Road, with bedrock apparently more welded than the sideslopes northeast of the road. Snow was present, particularly

on north-facing slopes at the bowl elevation. A hike to the bowl was abandoned partway due to time constraints, but portions of the hike were quite steep and strenuous and would be difficult to attempt with significant equipment. Other ridges south of the road might serve as an analog, but again would require significant effort to reach.

The Boundary Wash area is an adequate analog site, although other analog sites were identified with better characteristics. Unattractive features of the site include significant hiking, moderate welding, and low elevation. It may be worthwhile to consider limited study of the area as a supplemental analog for partial glaciation. Any studies would be likely be most practical if aerial analysis were the primary study mode, with limited ground confirmation.

Grapevine Mountains (Phinney Canyon)

Phinney Canyon, an east-draining canyon in the Grapevine Mountains, is located between Scotty's Castle (in Inyo County, California) and Beatty, Nevada. Phinney Canyon is in Nye County, several miles east of the junction between Inyo County, Esmeralda County (Nevada), and Nye County. The Grapevine Mountains are likely to feel significant effects of the Sierra Nevada rain shadow. Ground access to the Grapevine Mountain site is via a series of 4WD dirt road proceeding west from Rhyolite, north past Bullfrog Mountain to Sarcobatus Flat, and west to Phinney Canyon. Travel time from Beatty to Phinney Canyon is between 1-1/4 to 2 hr. Air access is not restricted.

Portions of the lower Phinney Canyon appear to be rather analogous to the washes at YM, especially two stretches of south-facing slope and at least one stretch of north-facing slope between the elevations of 6,000 and 6,600 ft. In these areas, the tuff is densely welded, with shards exhibiting the characteristic clinkstone clatter. Fracture patterns are quite reminiscent of densely welded TCw sideslopes, as best as can be ascertained from outcrop observations. Soils were also quite reminiscent of the YM washes, with similar sizes and percentages of rock shards, although the soils may be somewhat thicker.

A small snowmelt stream on the southfacing side of the canyon was located along a small fault, forming a waterfall. Under the waterfall, a cave was hollowed out to perhaps 2-m depth. Dripping from ceiling fractures was observed at numerous locations within the cave, apparently arising from stream infiltration several meters above.

The vegetation was somewhat anomalous in the lower portions of Phinney Canyon. Typically, juniper is observed at lower elevations than piñon, but in Phinney Canyon juniper was much sparser at the lower elevations than was piñon. Juniper was primarily observed on sideslopes, with

thin soils. Piñonwas quite dense in the wash bottom, reaching several meters in height.

The roadway was impassable due to snow at roughly 6,200 ft elevation. Drifts were as deep as 1 m at higher elevations, although deep depressions in the snow cover were formed at the base of most plants.

The Phinney Canyon site appears to be an excellent analog to YM washes, certainly the best of any site examined. Fractures may be slightly further apart than at YM, and soils may be somewhat thicker, but overall the site is highly recommended.

Rainier Mesa

Rainier Mesa, in the north-central portion of the NTS, rises to an elevation of roughly 7,000 ft. Rainier Mesa is topped with a moderately welded tuff caprock quite reminiscent of Yucca Crest with more boulders. Estimates of fluxes into the N-tunnel drifts provide information on net infiltration at Rainier Mesa, which can be used to calibrate infiltration models. Access to Rainier Mesa is by paved road, although camping at the site is unlikely to be allowed so that roughly 3 hr of driving will be required each day. Also, air access is strictly controlled and it may not be possible to obtain the aerial photographs required to quantify vegetation densities.

A carpet of snow up to 1/2 m thick covered the top of Rainier Mesa, closing the road and limiting observational opportunity. It appears that soils are similar to Yucca Crest, albeit with much greater organic content. Piñon, juniper, and mountain oak were found on the mesa caprock.

Long slopes extend from the mesa caprock to the valleys below, featuring hundreds of meters of densely welded through nonwelded tuffs. These slopes are reminiscent of the portions of the western flank of YM that lie above the Paintbrush Tuff nonwelded (PTn) outcrop. Densely welded tuffs, visible in road cuts, appear to be almost identical to the densely welded portions of the TCw tuff. These slopes may serve as an analog to the Solitario Canyon side of YM, although the lack of gully formation limits the analogy to Topopah Spring welded (TSw) exposures at YM. The slopes may also serve as an analog to the washes, but may suffer from the lack of a wash bottom collecting water. Perhaps the contrast between Rainier Mesa slopes and Phinney Canyon slopes may provide insight into lateral flow processes in the washes.

Conditions are currently very moist on the NTS. Yucca Lake is currently full to beyond the playa dimensions, and the alluvium at various locations on the Test Site is essentially saturated.

Problems encountered

None.

Pending actions

None.

Recommendations

Use the Phinney Canyon site for an analog to the YM washes, concentrating resources into evaluating the relatively poorly characterized sideslope environments. The Phinney Canyon studies should receive the highest priority for fieldwork. Analysis of aerial photography should be the primary study tool for the remaining sites, with limited ground confirmation of aerial observations. As much use should be made of aerial observations as is possible, as data acquisition is relatively fast, informative, and inexpensive.

Attachments

Annotated photographs of the potential analog sites examined during the trip were attached to the trip report. These are not included here.

4/28/98 Observations of rainfall/temperature variability.

As I was replying to comments on the UZFLOW module of the TPA code, it occurred to me that the variability about the bulk climate actually should incorporate all variability above the decade scale. Probably several scales are of interest: (i) decade, (ii) century, and (iii) millenial. Perhaps incorporating fine-scale Milankovich cycles would take care of the longer-scale perturbations.

The Beatty data is the most readily available for quick analysis of decadal scale perturbations. The Beatty data extends from 1945 through 1995, with daily observations of precipitation, maximum temperature, and minimum temperature. Unfortunately, the data appears to have gaps, with between 7 and 17 years missing at least 5 days of observations (up to 3 months were missing)

and one year appearing to have repeated observations (which are removed during the analysis). In addition, the weather station was moved once or twice, which Nichols (1987) suggests affected the readings significantly. Nevertheless, some useful information can be extracted from the data. As a quick and dirty estimate, all years (except the first and last) were used, even partial years. The values for variability derived from the data are biased too high because of the missing data and station relocation.

The decadal mean values for mean annual infiltration were extracted for each combination of ten years (35 combinations) and for consecutive decades (3 sets). The mean precipitation was about 5 in., with a standard deviation of 2.3 in. for annual variability and 1 in. for decadal-averaged variability (both methods) The average of the maximum and minimum temperature was used for mean annual temperature, yielding a mean of about 15.2 °C and standard deviations of 1, 0.46, and 0.53 °C for the annual, 35-combination, and 3-decade sets, respectively. The correlation coefficient between mean annual precipitation (MAP) and mean annual temperature (MAT) is -0.24, -0.89, and -0.92 for these three cases. Some of the correlation is likely due to weather-station relocation.

I would suspect that the coefficient of variation is more appropriate for the precipitation ($CV = \sigma/\mu$), so that the projection to YM would give a rough decadal variability of 0.2 times MAP, or about 30 to 35 mm/yr (assuming 150 to 175 mm/yr). Temperature variability should be roughly equivalent, so that appropriate decadal variability is 0.45 to 0.55 °C.

The longer-term variability is likely to be intermediate in magnitude between the decadal variability and the glacial-maximum variability. I suspect that the higher values of effective moisture reported by paleoclimatologists may represent a muted bulk variability with relatively short-term fluctuations (centuries) imposed on the bulk signal. If a reasonable multiplier of current MAP for bulk MAP is 2 (sampled 1.5 to 2.5), then microglacial perturbations with a CV of 1.5 would give peak glacial maxima of 3 times current MAP. An improved perturbation model might consist of short-term MAP oscillations with CV of about 0.2 (sampling 0.1 to 0.3) and mid-term MAP oscillations with CV of about 1.5 (sampling about 1 to 2). Note that the exponential dependence of mean annual infiltration (MAI) on MAP will give a larger expected MAI when perturbations are considered.

Temperature effects might be reasonably handled with short-term oscillations sampled between 0.4 and 0.6 °C and mid-term oscillations sampled between 2 and 4, and full-glacial maximum change sampled between 4 and 7 °C.

5/21/98 Trip report. SAS

The following is an excerpt from my trip report to YM from the period of May 13 through 18, 1998, in which characterization fieldwork was performed. My field documentation for the trip is in CNWRA notebook 175.

Persons Present

The trip to Yucca Mountain (YM) and Phinney Canyon (PC) (a potential climate-analog site), on May 13 through 18, 1998, was undertaken by R. Fedors (CNWRA) and consultants S. Stothoff, D. Groeneveld, D. Or, D. Woolhiser, and O. Chadwick.

Background and Purpose of Trip

CNWRA is working with S. Stothoff to refine model estimates of mean annual infiltration (MAI) over the repository performance period. The modeling to date has considered one-dimensional (1D) simulations of coupled heat and moisture transport, with the results of the simulations abstracted to grid blocks covering the repository footprint. The approach is limited by neglect of lateral flow, transpiration, soil genesis, and snow dynamics. The other consultants were retained to help refine the infiltration model to incorporate these processes appropriately. O. Chadwick provides expertise in soil genesis processes. D. Groeneveld provides expertise in Great Basin plant ecology. D. Or provides expertise in soil physics and field-measurement techniques. D. Woolhiser provides expertise in watershed modeling in the arid southwest.

Split Wash is strategically located above the path that the east-west exploratory drift is following. D. Woolhiser will be performing watershed-scale modeling for the north branch of Split Wash, and D. Or will be performing hillslope-scale modeling. These newly initiated activities require data on soil depth and other factors affecting overland flow and interflow, and are intended to consider both current and potential future climatic conditions. Much of the data collected on the trip is intended to feed these activities.

S. Stothoff, D. Groeneveld, and D. Or are attempting to characterize the impact of vegetation upon MAI over the next glacial cycle. Transpiration is a process included in DOE models but not considered in CNWRA modeling efforts to date. The intent of the CNWRA work is to incorporate vegetation into infiltration-modeling efforts in a plausible and defensible manner. The trip was

inspired by the need for field-checking hypothesized relationships between vegetation and bedrock type, soil cover, slope, and solar loading.

Soil depth and composition are significant factors influencing infiltration over the period of repository performance. Although soil depth and composition at YM are reasonably well understood under current conditions, significant changes in these factors may occur as climatic conditions change. O. Chadwick was retained for his expertise in soil genesis, with the anticipation that he may be able to identify likely past and future soil conditions. The field trip served as Chadwick's orientation to YM, with the trip to PC serving as an orientation to a site with climatic conditions similar to postulated future conditions at YM.

Summary of Activities

The fieldwork at YM was split into the following activities, performed primarily within Split Wash: (i) vegetation transects verifying the more-detailed TRW vegetation work and examining factors governing the distribution of individual species (D. Groeneveld and S. Stothoff); (ii) permeability measurements to characterize bedrock-fracture and soil properties (D. Or and R. Fedors), (iii) channel-characteristic measurements for the upper portions of Split Wash (D. Or and S. Stothoff), (iv) alluvial-terrace measurements (D. Or, D. Groeneveld, and S. Stothoff), (v) soil depth and composition measurements (O. Chadwick and R. Fedors), and (vi) field identification of potential infiltration hotspots in upper washes (S. Stothoff).

The fieldwork during the one-day trip to PC was split into the following activities: (i) orientation to the site (new to all but Stothoff), (ii) identification of vegetation study locations, and (iii) examination of soil characteristics.

Overall Impressions

The trip was extremely useful in orienting Chadwick to the YM site and in identifying and refining hypotheses regarding the soil depths and genesis processes. Soil and vegetation measurements taken during field activities will provide direct input into modeling activities. The trip was also useful in planning future activities with Chadwick, Groeneveld, Or, Stothoff, and Woolhiser.

Soil Genesis Interpretations Based on Field Observations

Significant insight was gained into the depth and composition of soils that might be expected over a glacial cycle at YM, both based on observations at YM (primarily in Split Wash) and at PC. The selection of Split Wash as a study location was fortuitous, as Split Wash may have the best-preserved deep alluvial terraces of all washes above the repository footprint. The stream channel has cut the terraces as much as 20 m to reach bedrock. In other washes, clearcut traces of deeper soils are not evident, having been nearly obliterated by erosion, but colluvial lobes along the sideslope toes are suggestive of soils that were deeper by up to 1 m. Similar erosional activities have been observed across the arid southwest that are dated to 8 to 15 ka, coincident with removal of vegetation as the climate became warmer and drier following the last peak in glaciation. The soils now present across YM are predominantly æolian in origin, and are relatively shallow and unweathered. At PC (roughly 700 m higher than Yucca Crest), on the other hand, soils are deeper, moister, more weathered, and have greater organic content.

Yucca Mountain soils are typically sandy loams in texture, while Phinney Canyon soils are more characteristic of silty loams. Simulations using the 1D BREATH code have been performed using properties similar to sandy loams and silty loams, allowing MAI to be roughly compared for YM and PC. The simulations predict that MAI may increase by 1 to 1.5 orders of magnitude as climatic change proceeds, if the soils are characteristic of those presently at YM. However, assuming that soil increases in depth from 25 to 50 cm, rock fragments decrease from 50 percent to 33 percent by volume, and the fine component changes from a sandy loam to a silty loam, predicted MAI is approximately 2.5 orders of magnitude smaller at PC for the current climatic conditions. Most of the decrease is due to the textural change of the soil. It would be expected that the PC soils are more sensitive to changing climate than the YM soils, but even so the predicted net effect would almost certainly be a reduction in MAI. The predicted decrease in MAI does not account for vegetation, lateral flow, or snow dynamics. Due to the colder winter temperatures, substantial snow cover may develop and the ground may freeze. These effects would dramatically change the dynamics of recharge during the winter and spring and would likely substantially increase MAI.

The potentially significant impact on MAI of changing soil texture and depth points out the importance of soil genesis characterization. Without observations of remnant soils similar to those at PC, however, the existence of soil change is arguable. Buried soils similar to those at PC were observed at three locations, once on the ridgetop separating the uppermost forks of the north branch of Split Wash and twice on the caprock upgradient of Split Wash. These soil-texture observations are extremely suggestive that textural changes might be expected over a glacial cycle

at YM, and these textural changes would be expected to reduce MAI. The rapidity of the textural changes is open to question, as it takes extended periods of time to weather sands into clays.

The rapidity of soil depth changes is also quite uncertain. Erosive tendencies vary with available moisture, with erosion occurring slowly when little moisture is available. Erosion increases with available moisture, but so does vegetation, until a point is reached where the increased stabilizing presence of vegetation counteracts the destabilizing influence of erosion. One would expect that changes in soil depth might respond exponentially to changes in climate, with rapid change decaying into a stable system. Soil texture also responds exponentially, but over a longer time span.

If the observations regarding soil depth and texture changes are correct, one might expect that MAI would increase relatively quickly as conditions become cooler and wetter, then would gradually decrease as transpiration increases, soil depths increase and soil textures become finer. As conditions become warmer and drier after the glacial maximum, one would expect that MAI might respond to shallower soils quickly but relatively slowly change due to textural change.

During the field work, enhancements to the existing CNWRA model for soil depth genesis were discussed. These enhancements would be intended to examine potential rates of soil depth and soil texture change at YM. The current model considers one generic soil in equilibrium with the environment, with soil generated through weathering and moving due to creep and ephemeral streamflow. Potential enhancements would include time stepping, several soil-particle sizes, an æolian source of dust, and chemical weathering.

Observations of Potential MAI Hotspots

The remnant channel terraces in Split Wash are not the only anomalous feature of the watershed. The northern branch of Split Wash terminates with a small channel fork. The southern of the two channels is choked with talus and alluvium, and there is no sign of stream activity for several hundred meters. Evidence of streamflow is present above the area choked with alluvium. The Tcpmn unit (middle nonlithophysal unit of the Tiva Canyon formation) crops out along the walls in areas with gaping fractures and talus. In this area, the rocks appear to be washed clean of dust and fractures tend not to have carbonate fillings. The vegetation in this area is particularly dense.

The combination of copious talus, nonexistent channel flow, gaping fractures, and dense vegetation are all factors suggesting that substantial infiltration may occur in this portion of the

watershed. A total area of roughly 10^4 m^2 might be classified as a potential infiltration hot spot. Interestingly, the east-west drift currently under construction will pass close to this wash. If the drift passes under the wash, it would not be surprising to find that *in situ* water fluxes are much larger than elsewhere in the repository footprint.

The observation that this particular wash area appears to be an infiltration hot spot while nearby washes do not appear to have such overt infiltration potential engendered lively discussion of the features that infiltration hotspots might exhibit. The existence of talus slopes is an obvious indicator, as evaporation is greatly reduced by talus. The presence of gaping fractures, particularly with minimal carbonate filling, is another indicator. Both talus and gaping fractures can be linked to the particular rock type cropping out. Densely welded units tend to form talus, as erosion removes blocks along fracture planes rather than removing grain by grain. The lithophysal units have fewer and finer fractures than nonlithophysal units, as the presence of lithophysae during cooling relieves some of the strain that forms cooling joints. Lithophysal units tend to spall, forming plate-like talus, while the nonlithophysal units tend to form bulkier talus. The lithophysal talus appears to be somewhat less resistant to further breakdown than the nonlithophysal units. Accordingly, locations with nonlithophysal units cropping out provide a heuristic indicator for both gaping fractures and talus, which are both strong indicators for high infiltration.

S. Stothoff examined eight of the sixteen upper-wash channels between Highway Ridge and Antler Ridge, all of which feature Tcpmn outcrops, to see if they also have other features indicative of high infiltration. Two of the washes, the Split Wash fork already mentioned and the north branch of WT-2 Wash (just south of Whaleback Ridge), appear to have notable high-infiltration areas while the remaining washes appear to be more typical. The WT-2 Wash area shares with Split Wash the characteristics of no recent runoff, copious talus, gaping fractures, dense vegetation, and minimal fracture fillings (at least near the bedrock surface). The nonlithophysal-unit outcrop areas in all of these washes appear to be generally more conducive to infiltration than the lithophysal areas, but the potential for infiltration is mitigated in many of the washes by limited outcrop area, shallow channel slopes, or shallow sideslopes.

In general, talus was more common on north-facing slopes and exposed bedrock fractures were more common on south-facing slopes. Densely welded nonlithophysal units in the examined washes rarely had exposed bedrock in the actual channel, while the lithophysal units often exposed channel bedrock for significant portions of the upper wash.

With the notion that deeper soils are indicators of reduced MAI, due to increased storage and opportunity for evapotranspiration, clues regarding soil depth during glacial periods were also

sought during the infiltration hotspot survey. Many of the washes featured concave-down slopes to the channel, which indicates that the most recent activity has been degradational. Colluvial lobes are apparent along many of the washes, suggestive that deeper soils may have existed in the past. If these washes become aggradational in the future, it would be expected that the deeper covers would reduce MAI and thereby reduce the hotspot activity.

References

Brown, T., S. Conrad, S. Wirth, J. Cochran, and J. Emery. 1997. *Plausible Future Climate States at the Area 5 Radioactive Waste Management Site, Nevada Test Site.* SNL-?, Sandia National Laboratories, Albuquerque, NM.

du Bray, E. A., D. O. Hurtubise, and C. A. Bannister. 1987. *Geologic Map of the Weepah Spring Wilderness Study Area, Lincoln and Nye Counties, Nevada 1:50,000.* Miscellaneous Field Studies Map MF-1922, United States Geological Survey, Denver, CO.

Nichols, W. D. 1987. *Geohydrology of the Unsaturated Zone at the Burial Site for Low-Level Radioactive Waste Near Beatty, Nye County, Nevada.* Water-Supply Paper 2312, United States Geological Survey, Denver, CO.

2. Ambient Hydrology KTI – Model Development

Account Number: **20-1402-861**
Collaborators: **Randy Fedors, Gordon Wittmeyer, Jim Winterle**
Directories: **$HomeTwo/Numeric/Breath and as noted**

Objective: Perform documentation of conceptual model and code development for subsurface flow and transport, particularly regarding infiltration. Work documenting coding work and bug fixes is documented elsewhere in the Scientific Notebook. Conceptual model development may include: (i) enhanced one-dimensional (1D) simulation capability (i.e., vegetation uptake, matrix-fracture interactions, true N-phase simulation, snow and ice, transport of tracers); (ii) two-dimensional (2D), 2.5D, or three-dimensional (3D) watershed-scale modelling; (iii) 2D, 2.5D, or 3D hillslope-scale modelling; (iv) diversion of infiltration due to the PTn layer; (v) discrete-fracture simulations.

2/9/98 Initial entry. SAS

Work exploring results from infiltration studies performed under the Ambient Hydrology KTI is documented elsewhere in this Scientific Notebook. In order to improve the transparency of computational model development, conceptual-model development is documented in one or more separate chapters. This particular chapter documents the development of enhancements to the *breath* code. It may be that the resulting code is so significantly changed that a new name is required, although politically it would probably be better to call it *breath*. I have a fondness for calling a new code VaporWare (Vapor for short), and enhancements that result in at least 2D simulations may be renamed.

The overarching developmental philosophy for new code is to maintain extensibility from 1D through 3D applications. Accordingly, some of the TOUGH and MODFLOW ideas will be followed. In particular, strict segregation between physics and computation should be followed. Thus, modules for equations of state should not be dependent on the computational scheme or dimensionality.

As dimensionality is added it should be possible to use previously defined lower-dimensionality schemes as plug-ins. For example, a 2D model should be able to have locally 1D segments overlain using the same variables (e.g., fractures within a matrix, overland flow). Similarly, a 3D model should be able to accommodate both 1D and 2D elements.

Ideally, the code should end up able to accommodate a wide variety of temperatures, ranging from below freezing to above boiling. It should also be possible to accommodate several simultaneous phases (air, water, oil) and several simultaneous components. Despite the generality in desirable physics, reduced complexity should also be accommodated with no lack of computational efficiency.

At its most complex, YM should only require the following elements: (i) 1D finite element, (ii) 1D finite volume, (iii) 2D triangle finite element, (iv) 2D quad finite element, (v) 2D finite volume, (vi) 3D prism (2.5D triangle) finite element, (vii) 3D brick finite element, and (viii) 3D finite volume. The difference between finite element and finite volume is in the definition of the unknown. In finite elements, the unknowns are located at the nodes (and edges, for mixed finite elements) and the elements are responsible for handling flow processes. In finite volumes, the unknowns are located at the center of the volume (and connections, for mixed finite volumes) and connections are responsible for handling flow processes. Finite volumes are simpler and arguably more accurate when they can be applied, but sharp discontinuities are difficult to accommodate. Finite elements are more complex to code and use, but can easily handle sharp discontinuities. The finite element approach allows adjacent elements, with different material properties, to share unknown values. The finite volume approach, on the other hand, must smear material properties over the distance between element centers.

The biggest mistake made during the coding of *breath* was made at the outset of the project. There was a choice between using C and Fortran. I selected Fortran for the possible benefits of sharing software and possible efficiencies if *breath* were to be used on supercomputers. So far, no sharing has occurred and workstations are approaching the capacity of supercomputers. There are several benefits of using C that have not been realized from this decision, including: (i) strong organizational capabilities (e.g., structures, pointers to functions), (ii) portable error-catching capabilities, and (iii) strong development tools for program input (e.g., flex, bison). Fortran-90 includes most C and C++ functionality, with far stronger array operations, but does not have the input-language tools.

Significant additional development should abandon the Fortran-77 language due to the above shortcomings. The fastest and most extensible procedure for development would be to base further code on *Matlab*, as there is a wealth of tools already developed and available as part of the *Matlab* package. *Matlab* is based on a very strong programming language, with many of the best features of both C and Fortran-90, was originally designed for numeric operations on arrays, and has a built-in Graphical User Interface (GUI) builder. The array-based nature of the *Matlab* language is easy to program in; code that is inefficient in the interpreted *Matlab* language can be replaced with compiled C code using a code translator supplied by *Matlab* or by independent programming.

Matlab is able to support standalone executable programs written in C or Fortran without requiring *Matlab* to be invoked, although I have not done so and do not know what would be required for porting applications. *Matlab* is used on numerous operating systems, so portability may not be a tremendous issue.

Coding in C/C++ overcomes questions about portability and is the second most favored approach. Using an environment called Jacquard, which I developed at UVM before joining the Center for Nuclear Waste Regulatory Analyses (CNWRA), much of the functionality of *Matlab* can be recovered and portability assured. At the time Jacquard was developed, there were several features that *Matlab* couldn't easily duplicate, but they are gradually being included in *Matlab*. The current version of Jacquard requires an SGI workstation for graphics, but is modular enough to adapt to OpenGL with minimal disruption.

2/10/98 Vegetation modelling. SAS

Model Rationale and Background

The intent of the plant uptake model is to plausibly take up water from the soil and from within fractures at YM under climatic conditions ranging from slightly drier than current to full glacial maximum. The model is intended to be an add-on to *breath*, and the implementation will be 1D to start. Ideally, a minimum of information should be required by the model, and that information should be readily estimated. It is not desirable that the characteristics of individual plants (e.g., a sagebrush or a juniper) are specified in detail; rather, the simulation should reflect the aggregate behavior of several plants within a community (i.e., the lateral extent captured by the 1D model should be on the order of a grid block within the Geographic Information System (GIS) model, or approximately 30 m x 30 m).

Typical models within the literature tend to provide a static distribution of root density or maximum root density with depth, and link uptake to the root density. The simplest approach is to proportionately take up water to satisfy transpiration requirements according to the maximum root density. A slightly more complex approach takes into account the relative soil moisture when apportioning uptake with depth. A final approach is to treat the plant as a continuum and take account of potential variation within the plant. The plant-continuum approach is easily extended into a dual-continuum formulation, representing the plant and the soil as two continua linked by leakage across the root hairs. A far more complex approach is to discretely model the individual roots, requiring the use of a 3D simulator. My experience is that this approach is extremely

slow, although this may be due in part to inefficient coding. Adaptive calculation of root-density distributions is not common, although the agricultural literature should account for changing uptake patterns during the growing season.

As the model increases in complexity, there are tradeoffs with both computational efficiency and data requirements. For example, the simplest model requires only the root density function and the transpiration rate, while as the model increases in complexity additional information such as soil-root uptake parameters and plant-transport parameters are required, and the calculations increase in complexity. On the other hand, as the models increase in complexity, the burden of appropriately apportioning rates of uptake with depth increasingly is shifted to the simulator, enabling increased plausibility. More is known or can be inferred about plant responses in general than uptake in the complex fractured-bedrock system at YM, so that there is real benefit in transferring as much burden as possible to the simulator within the bounds of feasible computational effort. For example, providing the root density function for soil overlying fractured bedrock is quite difficult to determine and would be required for each climatic scenario considered, while reasonable uptake and transport parameters are available in the literature or can be calculated. If the model adaptively calculates a root density function based on allowable growth rates and uptake information during the simulation, this function can not only be examined for plausibility (thereby providing ground-truth capability) but could provide basic information for the scientific community.

Two simple conceptual models for roots might be appropriate: (i) the vertical stem with horizontal roots branching at each node, and (ii) the cloud-o'-roots, with all roots branching from the main stem. Both models would split the plant into 3 conceptual regimes: (i) hair roots, where uptake from the soil takes place; (ii) transport system; and (iii) leaf system. The second model does not exclude the multiple root branching that plants exhibit; it does assume, in essence, that transport from hair to leaf occurs along independent channels within the same root. The first model would require that a separate set of plant potentials be simultaneously determined at each node point, resulting in a set of simultaneous equations to solve, while the second model can determine the nodal potentials without requiring a set of simultaneous equations to be solved. The computationally more complex first model would enable leakage of water from roots into dry soil. The second model may tend to overestimate the amount of biomass committed to roots by not accounting for the transmission efficiency gained by larger roots. Operationally, there may be little difference between the two models, as resistance losses in the transport system are typically small relative to losses across the root hairs and within the leaves, so that potentials within the transport system are relatively uniform. Uptake fluxes in both models would be controlled by resistance loss across the leaf area. Accordingly, the simpler model should be explored.

One area that requires a good deal of thought is the appropriate transpiration parameterization. This area is common to all of the models and will likely be difficult to resolve. Typically one parameterizes potential transpiration according to leaf area, and modifies this by the ability of the root system to deliver at the potential rate. Key information required for this approach is potential transpiration rate per leaf area, potential rates of change of leaf area with time, and modifications of the potential rates according to environmental conditions. Values of these parameters are likely species dependent, but it may be possible to regress some sort of relationship between climatic variables and plant uptake parameters if there is strong variability between species.

The potential rates are partly seasonal, but are also partly dependent upon plant-devised heuristic strategies. For example, shrubs may require adequate rainfall in the fall for growth in the spring (Beatley, 1974), otherwise remaining dormant. Different shrubs have a different tolerance for fall rainfall, so that there is a spectrum of responses to account for. Shrubs may emit a water-soluble growth-inhibiting compound that must be washed away before dormancy is averted. It should be simple to incorporate a module that simulates this behavior. A simple model would be

$$\frac{\partial c}{\partial t} = \alpha(c - c_{max}) - \beta q_{rain}, \tag{2-1}$$

where α and β represent seasonally dependent rate constants such that a good fall rain would remove any accumulated buildup and a poor fall rain would result in significant concentration, c, of the growth-inhibiting substance. Any potential rate, G, might then be dependent on the depletion in c, so that $G = G_{min} + G_{max}(1 - c/c_{max})$.

Adaptive modification of biomass distributions according to environmental conditions is another area that requires significant effort to resolve plausibly. Plants tend to allocate roots adaptively to maximize uptake of a growth-limiting resource (typically nitrogen, phosphorus, or water). The strategy is to grow and respond rapidly to environmental conditions at the end-member locations (hair roots, leaves) and grow slowly in major transport systems. Thus, there are numerous time scales to resolve: (i) minute-to-minute transpiration, (ii) growth and death of end members within days to weeks, and (iii) growth and death of transport systems within seasons or years. Simple parameterization will be key, but allocation of the resource within the plant should be taken into account in order to limit growth according to environmental constraints.

Model Overview

The following model provides a tight linkage between transpiration, temperature, soil moisture, and vegetation biomass, and should be able to resolve uptake at any time scale of interest. There are

relatively few parameters, and most of them can be estimated fairly easily. The model is formulated in terms of a single limiting nutrient, which could be either moisture or some chemical compound. Modelling the nutrient transport serves as a surrogate for detailed consideration of the details of transpiration, storage, and respiration. Transport of the chemical compound in the porous matrix must be modelled. If the limiting compound is not water, this will require an additional transport simulation, and sources must be considered. I would expect that the transport simulation might use a time-averaged flow field and a larger time step than the water simulation.

The model presupposes that vegetation will preferentially allocate growth to maximize uptake of the limiting nutrient, but not transpire more than required to satisfy respiration and possibly cooling requirements. Note that cooling requirements are not necessarily an issue for the sparse vegetation of desert shrubs as the leaves are well coupled with the atmosphere, according to David Groeneveld, but might be for the piñon-juniper association due to its denser vegetation. Vegetation is assumed to have built-in rate limits on the growth of the three modelled plant-system components (root hairs, transport, and leaves). Given ample supplies of the nutrient, any one of the three components may limit transpiration rates, although usually either transfer across the root hairs or stomatal resistance should be rate-limiting. While the nutrient is not available in sufficient quantities to support the biomass, vegetation biomass is trimmed at characteristic rates.

The interplay between growth, death, and uptake provides the adaptivity to environmental conditions that can capture vegetation adaptation to climatic change. The parameters are fairly general, but must be tuned to match observed conditions. Some of the parameters may depend on climate; for example, it may be that growth rates are slower under cooler conditions.

Nutrient allocation is assumed to follow a strict hierarchy. The demands of the current biomass are satisfied first. Any surplus nutrient goes into storage. If surplus nutrient exists once the storage is at capacity, growth occurs to maximize nutrient uptake. Nutrient-inspired transpiration is limited once maximal growth rates are achieved, so that there is no surplus nutrient uptake unless cooling is needed.

If there is a deficit in nutrient uptake, so that not even current biomass demands are satisfied, the nutrient is removed from storage to satisfy demands. If this is still not sufficient, biomass is trimmed until the available nutrient is sufficient for biomass demands. Note that storage should be large enough to supply biomass demands for one to several days. Also note that the growth and death rates should be much slower for the transport system than for either root hairs or leaves, as there is much greater capital expense involved in growing the transport system.

In actuality, both water and one or more nutrients may be limiting at any particular time.

The above conceptual model could be easily extended to account for multiple potentially limiting factors, by assuming that only one factor at a time is limiting. Such work is beyond the immediate scope of the analysis.

Soil System

The soil system is conceived of as being penetrated by roots spaced more-or-less uniformly. Within the soil, moisture flow is modelled as usual, except for the uptake term. Uptake from the soil is controlled by average distance from root to bulk soil center as

$$q_{uptake} = \frac{K(\theta)\Delta\phi}{\tau_{soil}\lambda_s/2}. \tag{2-2}$$

where $K(\theta)$ is the soil hydraulic conductivity, $\Delta\phi$ is the drop in potential from soil to root-hair wall, and $\tau\lambda_s/2$ represents an average length from soil to root hair including tortuosity effects (such as might occur with fractures). The λ_s parameter might be determined by

$$\lambda_s = A_{plant}/(\lambda_h + \lambda_t), \tag{2-3}$$

which shows that the distance travelled in the soil is inversely proportional to the length of the root system. The A_{plant} (area encountered by the plant) parameter is problematic, as it is an absolute area and the parameter of interest in the leaf system is leaf area per unit area. Perhaps A_{plant} can be parameterized in terms of a maximum leaf area index (LAI) coefficient, maximum leaf area, and root/shoot ratio.

Root-Hair System

The root-hair system is extremely dynamic. Vegetation does not invest heavily in creating root hairs, so they tend to be quite opportunistic. Root hairs are only present where horizontal lateral roots exist. In the model, root hairs are parameterized by λ_h, the length of root hair per unit cross-sectional area, and θ_h, the ratio of λ_h to the maximum able to be accommodated by the transport system. The maximum that the transport system can accommodate is proportional to lateral transport-system length, λ_t, according to

$$\lambda_h = \kappa_{ht}\theta_h\lambda_t. \tag{2-4}$$

It is assumed that root-hair growth is affected by nutrient-uptake availability, transport-root

capacity, and temperature. A format of such a root-growth model is

$$\frac{\partial \lambda_h}{\partial t} = \gamma_h(T, S_{soil})\kappa_{ht}(1-\theta_h)\lambda_t U_{soil}. \tag{2-5}$$

Note that this model accounts for temperature effects, soil strength, transport-system support capacity, and nutrient-uptake availability. The temperature dependence should be such that no growth occurs above and below cutoff temperatures and maximal growth occurs in some optimal range. Soil strength reflects both soil moisture and soil resistance.

Uptake into the root-hair system is dependent on the soil conditions and the root-hair conditions. Uptake across the hair interface is proportional to the gradient from the soil to the hair,

$$q_{hair} = C(\theta_h)\Delta\phi, \tag{2-6}$$

where q_{hair} is flux into the hair, $C(\theta_h)$ is the conductance (conductivity divided by wall thickness) of the hair wall, and $\Delta\phi$ is the drop in potential from soil to hair interior. The conductance should drop to zero as θ_h approaches zero.

Transport System

The transport system is conceptually divided into a main vertical stem and a continuum of horizontal lateral roots. Each 1D element has a stem. Stems can be inactive (i.e., below the rooting depth), but there are no gaps in the active stem system. Each stem element has the potential for horizontal lateral roots. The highest inactive stem element retains the potential for growing horizontal lateral roots, so that the rooting zone can extend downwards.

The vertical system is parameterized by A_{stem}, the area of the active stem. Growth of the vertical stem is dependent on time-averaged flux of water through the stem. As any chemical nutrient is very dilute and does not affect flow, the stem capacity is independent of any chemical nutrient. Fluxes within the stem are described by

$$q_{stem} = -\kappa_{stem} A_{stem} \nabla\phi, \tag{2-7}$$

where κ_{stem} is the conductivity per unit area. Note that flux is also linearly dependent on the stem area.

The lateral component of the transport system consists of nominally horizontal roots, parameterized by λ_t (length of lateral root per unit area) and A_{stem}. Fluxes within the lateral component

of the transport system are described by

$$q_{lat} = \frac{\kappa_{stem} A_{stem} \Delta\phi}{\tau\lambda_t/2}. \tag{2-8}$$

where κ_{stem} is the conductivity per unit area, $\Delta\phi$ is the drop in potential from hair to stem, and $\tau\lambda_t/2$ represents an average distance from hair to stem.

It is assumed that transport-root growth is affected by root-hair usage, soil strength, and temperature. A format of such a root-growth model is

$$\frac{\partial\lambda_t}{\partial t} = \gamma_t(T, S_{soil})\theta_h\lambda_t \tag{2-9}$$

Note that this model accounts for temperature effects, soil strength, transport-system support capacity, and nutrient-uptake availability. The temperature dependence should be such that no growth occurs above and below cutoff temperatures and maximal growth occurs in some optimal range. Soil strength reflects both soil moisture and soil resistance.

In both the vertical and lateral components of the transport system, flux is proportional to the active cross-sectional area. The evolution of the cross-sectional area might be described by

$$\frac{\partial A_{stem}}{\partial t} = \gamma_{stem}(T)(\nabla\phi - \nabla\phi_{opt}), \tag{2-10}$$

where it is assumed that there is some optimal gradient in potential and time-averaged potentials are used. The assumption is that active stem area handles average flows. It is not clear where the optimal gradient in potential will come from, perhaps by using estimates of typical active-stem area, time-averaged transpiration rate, and conductivity for some shrubs.

Leaf System

The leaf system controls the transpiration rate, manipulating the potential within the plant by changing the stomatal conductance. By adjusting stomatal conductance, transpiration rates are adjusted, the potential at the top of the stem is adjusted, and fluxes across the roots are adjusted.

Flux across the leaf/atmosphere boundary is controlled by

$$q_{leaf} = A_l C_{leaf} \Delta\phi, \tag{2-11}$$

where A_l represents the leaf area exposed to the atmosphere per unit area, C_{leaf} is the leaf/atmosphere interface conductance, and $\Delta\phi$ is the drop in potential from leaf to atmosphere. C_{leaf} is controlled by the stomates.

A_l is the product of plant cover and LAI, and is the parameter of interest when describing leaves.

Transpiration Observations

In this section, all observations (with corresponding citations) are collected by Kozlowski and Pallardy (1997).

Respiration has been found to be strongly dependent on temperature. Typically, respiration varies linearly with temperature below about 10 °C, exponentially with temperature between 10 and 25 °C, and may decrease above 35 °C. The rate of increase in the exponential range is characterized by the Q_{10} value (relative change in respiration for a 10 °C change in temperature), which ranges from 1.4 to 3.4 for cypress, 2 for scotch pine, and 2.9 for loblolly pine.

Respiration tends to be reduced by water stress but does not appear to be as strongly impacted as by temperature. Respiration demand is roughly halved at -48 bar for loblolly pine, but stress actually increases respiration to 150 percent at about -28 bar. Respiration decreases, increases, and decreases, as stress becomes successively more negative. Kozlowski and Pallardy (1997) state that respiration generally decreases somewhat with drying.

Respiration tends to be greater with young vegetation parts and parts with high proportions of living tissue (e.g., leaves, root hairs). Leaves were found to account for 50 percent of transpiration in a 60-year-old beech forest, 60 percent in a tropical rain forest, and 32 percent in a young loblolly stand. Respiration from all branches has been found to be about half of the total autotrophic respiration in a loblolly pine plantation. Almost all of the root respiration is in the fine roots; more than 95 percent of root respiration for pine and birch stands is in the fine roots. Seasonal production of CO_2 in a loblolly pine plantation peaked at 0.05, 0.2, 1, and 14 $gCO_2\ m^{-2}\ hr^{-1}$ for roots, branches, stem, and foliage; the first three dropped to about 0.02 during winter while foliage bottomed out at about 3.

Moisture uptake is reduced as the soil temperature drops (although it is not clear what confounding processes take place). A number of pines exhibit roughly linear decreases in uptake as the soil drops from 25 °C to 0 °C, ranging from roughly 15 to 40 percent of the 25 °C uptake. The reduction was greatest with the temperate pines. The reduction is attributed to permeability decrease of roots and viscosity increase in water.

Permeability varies within parts of vegetation. In northern white cedar, leaf specific conduc-

tivity (LSC), which is defined as the rate of flow in a stem or branch caused by a unit of pressure potential gradient, is about 30 times greater in stems than small twigs. Conductivity of red pine roots was about 50 times greater than in the stem and increased away from the stem. Resistance to water flow in whole shoots of maples is estimated as 50 percent in leaves and petioles, 35 percent in branches, and 15 percent in the trunk.

3/4/98 Vegetation modelling continued. SAS

Transport System

The λ_s parameter really represents a measure of space-fillingness. Perhaps a better parameterization would be something like

$$\lambda_s = \beta \left[\frac{(\rho_h + \rho_t)_0}{(\rho_h + \rho_t)} \right]^{\alpha}, \tag{2-12}$$

where β is a soil-dependent scaling constant [L], α is a plant-dependent fractal constant, and the root length densities [L/L^3] are normalized to a plant-dependent value. Root-length density is often used (Caldwell, 1994). Actually, probably only ρ_t need be considered, since hair roots are assumed not to venture far from the transport roots, leaving

$$\lambda_s = \beta \, (\rho_{to}/\rho_t)^{\alpha}. \tag{2-13}$$

The fractal constant captures the space-fillingness. A perfectly space-filling root system in 2D would have $\alpha = 1$, while a very poorly space-filling root system in 2D would have α close to 0. The point can be illustrated by considering a unit square with a root system represented by squares within the area. Each square has a root length of 4 times the side length. The boxes are placed so that the side length for each box is an integer multiple of the side length of the innermost box. In this case, the average distance from the furthest point in the soil from a box is approximately half the side length of the smallest box.

Consider the case where we halve the average soil/root distance each iteration. The inner-box side length has a sequence of (0.5, 0.25, 0.125, ...), or $1/2^n$. The corresponding soil-root distance has a sequence of $1/2^{n+1}$. The corresponding root length has a sequence of (2, 6, 14, 30, ...), or $2 \times (2^n - 1) \approx 2^{n+1}$. The sequence indicates that λ_s is proportional to the reciprocal of λ_t in this efficiently space-filling scheme, corresponding to $\alpha = 1$.

In a perfectly inefficient scheme, λ_s remains constant regardless of changes in λ_t. This situation corresponds to $\alpha = 0$.

The same ideas apply in 3D, except that a perfectly space-filling root system would have $\alpha = 2$ (i.e., $N - 1$, where N is the number of spatial dimensions. I would expect the root system to be fairly efficient in exploring the soil space, so values of α may be on the order of 1.3 to 1.5.

Fitter (1994) discusses architecture and biomass allocation of root systems. An interesting point is raised, that specific root length (length of root per unit mass) is a good correlate of root diameter, with finer roots having greater specific root length. This observation should be followed up; it may lead to a parametric relationship between ρ_t and A_{stem}.

3/27/98 Discrete-fracture ideas. SAS

Most of the flow modeling at the drift scale has assumed that fracturing occurs as a continuum. As a rough approximation, I think that 5 fractures per grid block should be sufficient for this assumption. Mapped fracture densities are between 0.5 and 5 per meter in the TSw unit (Sonnenthal et al., 1997), where mapping only accounts for fractures with traces of at least 1 m. Assuming that fracture densities are roughly 5 per meter, which should include some of the smaller, unmapped fractures, grid blocks need to be at least 1 m in dimension to make the continuum approximation valid. Incorporating discontinuities at this resolution may not be feasible in a continuum model, particularly if the details of the fractures are required. On the other hand, a flow-routing scheme similar to my geomorphic modeling work may enable extremely fine grids to be evaluated. I want to develop the ideas here for future reference.

The key idea that I used in the watershed modeling is that topography dominates flow routing. When this is true, it is possible to sort the grid blocks by elevation and calculate routings once and for all. When flows occur in films, in large apertures, this assumption is also valid. I expect that the assumption begins to break down once capillary forces are involved.

Several approaches might be tried. It may be possible to generate constitutive relationships for individual fractures. Very fine rough-aperture grids might be created, hooked together into a few intersections, and the characteristics of flow as features are modified might be examined. Perhaps the individual fractures could be upscaled into a continuum using a probability distribution to capture flow diversions. At some point it would be possible to incorporate matrix interaction using quasi-linear approaches and BEM methods, including the effects of fracture coatings on flow.

The first order of business is to identify the appropriate flow characteristics for an individual fracture. A fracture will generally have either a thin film of water covering both walls (perhaps only a few molecules thick) or will be filled with water. Note that relative humidities are likely to be

almost 1, which will mediate the thickness of the film as well. Some fractures may have carbonate or opal fillings.

In the case of a fracture filled with carbonate or opal, flow occurs through vapor transport and Darcy's law. Resistance to flow is due to the permeability of the filling material and the thickness of the aperture (no turbulence). In the case of a water-filled fracture, the resistance is due to viscous effects and is proportional to the cube of the aperture (no turbulence). In the case of film flow, capillary effects are dominant for thin films and become less important as the film gets thicker.

Let me recap flow laws in terms of 2D fracture flow of an incompressible fluid with local coordinates ξ and η. Flux is generally of the form

$$\mathbf{q} = -bK(\theta)\nabla(P + \rho g z), \tag{2-14}$$

where b is the fracture aperture, $K(\theta)$ is different for the different flows, and the remaining symbols are the usual suspects. For porous media, classical retention relationships (e.g., van Genuchten relationships) are appropriate. For laminar flow between two smooth plates,

$$\mathbf{q} = -\frac{b^3}{12\mu}\nabla(P + \rho g z), \tag{2-15}$$

where μ is viscosity and again b is the fracture aperture. For laminar film flow on a smooth plate,

$$\mathbf{q} = -\frac{b^3}{3\mu}\nabla(P + \rho g z), \tag{2-16}$$

where b is the film thickness. Note that a fracture can carry almost 4 times as much flow under gravity conditions if only one side of the fracture is wetted. For laminar flow in a capillary,

$$\mathbf{q} = -\frac{\pi r^4}{8\mu}\nabla(P + \rho g z), \tag{2-17}$$

where r is the capillary radius; average velocity is $\mathbf{q}/\pi r^2$. The laminar-flow expressions are presented in Chapter 2 of Bird et al. (1960).

Tetsu Tokunaga and Jiamin Wan presented studies of film flow on tuff surfaces to the UZFM Expert Elicitation panel on December 19, 1996, including an analysis of measured and theoretical velocities for film flow in partially filled capillary tubes (representing pores). It appears that pores of 5 μm and larger may contribute significant fluxes. A vertical capillary tube of radius r was considered full when the water surface had a radius of $2r$, corresponding to a matric head (m) of $-\gamma/2\rho g r$ and an average velocity of $\rho g r^2/15\mu$. It seems that the average velocity should actually be smaller than $\rho g r^2/16\mu$ (half-full capillary flow).

It seems to me that I have seen a derivation someplace that builds up film flow using the bundle-of-capillary tubes idea, similar to the approach used by van Genuchten. Certainly it should be straightforward to relate the van Genuchten α and m values to pore-size distributions. The velocity distribution in a capillary half-tube should be dependent on head through the curvature of the meniscus, which implies that the flux of the pore set can be obtained through integration. The bigger question is what happens when the flow is wet enough to have capillarity acting on asperities larger than pores.

The computational approach for a discrete fracture should be based on a rectangular or triangular grid, with two unknowns per grid point: the head for each wall averaged over the film thickness. When the aperture is filled with water, the two unknowns are equal. If there is a fracture coating, perhaps an additional unknown is needed.

4/22/98 System of equations for vegetation model. 

My current thinking on equations for the vegetation model is presented below. Much of the preliminary reasoning has been discussed before, so new ideas are the focus of the discussion. The equations have fairly well gelled, unless noted otherwise. Most of the basic ideas have been passed through Dani Or, with some discussion with David Groeneveld.

The vegetation model consists of four active types of variables. Three variables describe roots and are dispersed throughout the soil column, while one describes leaves (consisting of one layer). For current climatic conditions, the sparseness of the above-ground portion of the vegetation does not require much detail; however, the density of vegetation on higher-elevation sites suggests that it may be desirable to include multiple leaf layers to account for shading and cooling effects.

The four variables are all dimensionless, representing volume of biomass per unit volume [L^3/L^3]. Subscripts for variables are:

- l represents leaves
- v represents vertical roots
- t represents transverse roots
- h represents hair roots

The volume quantities for roots are straightforward to calculate. Each root has a length density (e.g., ρ_v represents the length of vertical roots per unit volume [L/L^3]). Each also consists of a characteristic cross-sectional area for a root (i.e., A_v is the vertical-root cross-sectional area

[L^2]). These are multiplied together to create the dimensionless variable (e.g., $\Theta_v = \rho_v A_v$). The unit volume is the 1D element thickness times the unit area.

The volume quantities for leaves are similarly straightforward to deal with. The typical quantity describing leaf density used by plant biologists is LAI, or the projected leaf surface area per unit ground surface area. To calculate Θ_l, LAI is multiplied by half of the typical leaf thickness (note each leaf has two sides). If the leaves are needles, LAI is multiplied by half of the typical radius to obtain Θ_l. The unit volume is a typical plant height times the unit area. If several leaf elements are used (when plant densities are greater), then the unit volume is the 1D leaf-element thickness times the unit area (similar to the root elements).

Length density and cross-sectional area should be related, with a greater length density also creating a greater cross-sectional area. I propose a relationship in the form

$$\left(\frac{\rho_i}{\rho_{io}}\right) = \chi \left(\frac{A_i}{A_{io}}\right)^{\beta}, \tag{2-18}$$

where χ and β are constants. The relationship between the two is not important for vertical roots, as only A_v has an impact on plant performance.

The contact between plant leaves and the atmosphere degrades as more leaves are present. For example, desert shrubs are well-connected to the atmosphere while the inner parts of piñon pines are not. Perhaps a similar relationship between LAI and leaf thickness will capture the less-efficient connection and increased cooling-transpiration demand as the leaf biomass increases.

The plant-dynamic scheme is broken into three broad components: (i) calculation of potential biomass growth and death rates, (ii) calculation of actual biomass growth and death rates, and (iii) calculation of plant-uptake rates (the quantity of interest). The scheme avoids complications of detailed consideration of photosynthesis, respiration, and plant growth. Instead, all interactions are translated into terms of one surrogate limiting nutrient, which might be water or might be a nutrient such as nitrogen or phosphorus. It would be possible to extend the approach to consider multiple limiting nutrients, but this will not be done in the near future.

A logical plant-growth time step is one day, thereby eliminating the considerations of detailed allocation under solar stress. Over the course of the day, the plant obtains a certain amount of the limiting nutrient through soil-moisture uptake. Conceptually, the nutrient is allocated between cell respiration, cell biomass, storage, wastage, and reproduction. Reproductive usage is implicitly handled by an efficiency factor taxing uptake. The plant is assumed to allocate the remaining nutrient so as to maximize the expected plant-available nutrient at the end of the next time step.

In order to impose the scheme, it is necessary to quantify the options available to the plant for nutrient allocation and the costs associated with each option. The options available for each plant component are straightforward. The plant can allocate just enough nutrient to the plant component to satisfy expected respiration demands (i.e., stand pat). The nutrient allocation can be increased beyond the stand-pat value, yielding plant growth proportional to the increased nutrient, up to the maximum-growth amount. Or the nutrient allocation can be decreased from the stand-pat value, down to no allocation, resulting in biomass death proportional to the shortfall in nutrient.

Net nutrient usage is the most important part of the cost structure. The direct cost of nutrient usage is straightforwardly calculated by taking into account how much nutrient is consumed by the biomass. Opportunity costs are also associated with nutrient allocation. In particular, transport roots are conduits for flow from the hair roots to the leaves. These roots are slow and expensive to grow. The roots reach a balance between uptake capacity during peak parts of the year (i.e., spring) and respiration demand during the remainder of the year. If the plant did not account for the opportunity cost required to grow them, the roots would be quickly killed during the offseason and the plant would diminish from year to year. Accordingly, it makes sense to incorporate the same penalty to killing roots as it does to growing them.

The second type of opportunity cost results from the dependence of one plant component on densities of another plant component. For example, there is a limit to how many root hairs can be supported by the transport system. Accordingly, there may be advantage to growing additional transport roots in order to support higher densities of hair roots. This advantage must be accounted for in nutrient allocation.

Potential growth and death rates are also straightforward to calculate. Some death is assumed to unavoidably occur due to old age, regardless of nutrient allocation. Growth is assumed to occur proportionally to the allocation of nutrient above the respiratory requirement, up to a limiting rate. Death is assumed to occur proportionally to the allocation of nutrient below that necessary for respiration, again up to a limiting value (complete death depends on the time constant).

A typical root-growth rate is formulated as

$$\frac{\partial \Theta_i}{\partial t} = \gamma_i(T, S_{soil}) \left(1 - \frac{\rho_i}{\chi_{ij}\rho_j}\right) \left(\frac{\Xi - \Xi_r}{\Xi_r}\right) - \omega_{age}\Theta_i, \tag{2-19}$$

where

Θ_i is dimensionless mass of root component i
ρ_i is length density of root component i
ρ_j is length density of root component j
χ_{ij} is the maximum length of root component i per unit length of root component j
γ_i is the maximum growth rate of component i
T is temperature
S_{soil} is soil strength
Ξ is allocated nutrient mass ($\Xi_r \leq \Xi \leq \Xi_r + \Xi_g$)
Ξ_r is the nutrient mass required to meet all respiration needs
Ξ_g is the nutrient mass required to provide full growth
ω_{age} is the death rate due to old age

The root-growth formulation exhibits a one-way dependence, with hair roots dependent on transverse roots and transverse roots dependent on vertical roots. Vertical roots do not have this growth limitation.

A typical root-death rate is formulated as

$$\frac{\partial \Theta_i}{\partial t} = \left(\omega_i(T) \frac{\Xi - \Xi_r}{\Xi_r} - \omega_{age} \right) \Theta_i, \tag{2-20}$$

where

Θ_i is dimensionless mass of root component i
ρ_i is length density of root component i
ω_i is the maximum death rate of component i
T is temperature
Ξ is allocated nutrient mass ($0 \leq \Xi \leq \Xi_r$)
Ξ_r is the nutrient mass required to meet all respiration needs
ω_{age} is the death rate due to old age

The leaf growth formulation has the same general format for growth

$$\frac{\partial \Theta_l}{\partial t} = \gamma_l(T) \left(1 - \frac{\Theta_l}{\chi_{lv} \Theta_v} \right) \left(\frac{\Xi - \Xi_r}{\Xi_r} \right) - \omega_{age} \Theta_l, \tag{2-21}$$

and death

$$\frac{\partial \Theta_l}{\partial t} = \left(\omega_l(T) \frac{\Xi - \Xi_r}{\Xi_r} - \omega_{age} \right) \Theta_l. \tag{2-22}$$

4/23/98 Continuation of equations for vegetation model.

Each plant component is assumed able to store some amount of the limiting nutrient in easily plant-available form. It is assumed that each plant component has the same relative saturation of the limiting nutrient, and each component changes the relative saturation at the same rate. When a plant component dies, the easily available nutrient in the component returns to the plant. The total plant-available storage of the nutrient is characterized by

$$\Xi_s = \sum_{i=1}^{N} C_{si}\rho_{Bi}\Delta z_i \Theta_i \theta_\eta, \tag{2-23}$$

where

- Ξ_s is total mass of plant-available nutrient [M/L^2]
- C_s is maximum mass of plant-available nutrient per unit biomass [M/M]
- θ_η is the fraction of the available plant-available nutrient storage used up [-]
- ρ_{Bi} is biomass density of root component i [M/L^3]
- Δz_i is the thickness of element i

Each plant component is assumed to require some amount of the limiting nutrient in non-retrievable form in order to grow. It is assumed that each plant component uses up a certain mass of nutrient per unit biomass. The total non-retrievable storage of the nutrient is characterized by

$$\Xi_b = \sum_{i=1}^{N} C_{bi}\rho_{Bi}\Delta z_i \Theta_i, \tag{2-24}$$

where

- Ξ_b is total mass of nutrient irretrievably used in biomass [M/L^2]
- C_b is mass of irretrievable nutrient per unit biomass [M/M]

Each plant component is assumed to require some amount of the limiting nutrient for respiration each time step. The total respiration of the nutrient is characterized by

$$\Xi_r = \sum_{i=1}^{N} C_{ri}(T)\rho_{Bi}\Delta z_i \Delta t \Theta_i, \tag{2-25}$$

where

- Ξ_r is mass of nutrient expended in respiration per unit biomass [M/L^2]
- C_r is rate of nutrient mass expenditure in respiration per unit biomass [M/M/t]

The limiting nutrient is taken up by the plant during the course of a time step, with plant components that are based on the choices made in the previous time step. The uptake of soil water

is based on potential flow within the plant, similar to the potential flow in the soil. There are two continua modeled, the vertical plant continuum and the soil continuum. There is leakage from one continuum to the next.

The flux from a soil node to a vertical-plant node is proportional to the head gradient. There are three legs: (i) soil to hair, (ii) across the hair boundary to the transverse root, and (iii) through the transverse root. Flow through a leg is through horizontal porous-media flow:

$$q_i = -\frac{K_i(T)}{\rho g}\frac{\partial P}{\partial x} \tag{2-26}$$

or

$$q_i = -\frac{C_i(T)}{\rho g}\Delta P, \tag{2-27}$$

where

- q is water flux [L/T]
- K is conductivity [L/T]
- C is conductance [1/T]
- T is temperature [K]
- ρ is water density [M/L^3]
- g is acceleration due to gravity [L/T^2]
- P is pressure [M/L T^2]

Within the soil, K is the soil conductivity, which is dependent on soil moisture and temperature. The characteristic length for the soil leg is hypothesized to be dependent on the length density of transverse roots, with the form

$$\lambda_s = \beta\left(\rho_{to}/\rho_t\right)^{\alpha}. \tag{2-28}$$

As with the following equations, a subscript with a o denotes a reference value.

Within the root hair, conductance is used rather than conductivity. The primary resistance to flow is assumed to be across the hair walls, so that resistance within the hair itself can be neglected. Resistance across the root hair is assumed to have a component that depends on soil moisture, and is proportional to surface area. The formulation for root-hair conductance is

$$C_h = C_{ho}\frac{\mu(T_o)}{\mu(T)}\left(\frac{A_t}{A_{to}}\right)^{1/2}\frac{\rho_h}{\rho_{ho}}f(\theta), \tag{2-29}$$

where

T is temperature [K]
μ is viscosity [M/L T]
A is characteristic cross-sectional root area [L^2]
$f(\theta)$ is a yet-undetermined function of soil moisture [-]

The reduction of the root-hair conductance as a function of soil moisture accounts for shrinkage of the root hair away from the soil, providing an air gap, when the soil is dry. The dependence on A_h and ρ_h is through the surface area available for uptake.

The most poorly defined conductivity/conductance is for the transverse roots. For the time being, a conductivity function,

$$K_t = \frac{k_t A_t}{\mu(T)} \tag{2-30}$$

and a characteristic length,

$$\lambda_t = \frac{\beta}{\tau}\left(\frac{\rho_t}{\rho_{to}}\right)^{\alpha}, \tag{2-31}$$

will be combined into a conductance,

$$C_t = \frac{K_t}{\lambda_t}, \tag{2-32}$$

where

k is a dimensionless coefficient [-]
τ is tortuosity [-]
β is a plant-dependent length factor [L]
α is a plant-dependent scaling factor [-]

The vertical roots use the same type of conductivity relationships as the transverse roots, except that the characteristic length is directly available from the numerical model, leading to the formulation

$$q_v = -\frac{k_v A_v}{\tau\mu}\frac{\partial}{\partial z}(P + \rho g z). \tag{2-33}$$

Leaves will be treated using a conductance, with the maximum conductance proportional to effective leaf surface area,

$$C_l = C_{lo}\frac{\mu(T_o)}{\mu(T)}\frac{\Theta_l}{\Theta_{lo}}. \tag{2-34}$$

The actual conductance can range from zero to this limit, based on projected nutrient uptake demand and the transpiration required to meet this goal. The conductance can increase arbitrarily as necessary to restrict transpiration, with no more transpiration occurring during a time step than is necessary to meet projected needs.

4/29/98 Continuation of equations for vegetation model. SAS

I have just read several chapters summarizing root behavior (Waisel et al., 1996). There are several points that I take away from the discussions.

- Root hairs are not the only source of uptake, but they do enlarge the available surface area. Some plants do without.
- New roots are more effective at uptake than old roots, but the respiratory requirements are larger as well.
- Radial conductivity is roughly two orders of magnitude smaller than axial conductivity, expressed in per-unit-area terms.
- There may be a reduction in conductivity at high flux rates. This may be due to multiple flow pathways, one primarily responding to hydraulic gradients and the other primarily responding to osmotic gradients.
- Root growth may be limited by solute-concentration requirements rather than water availability.
- Plants may be healthier when they transpire at greater rates than is required for peak growth.

The dependence of roots on temperature has two components: (i) growth and (ii) death. It is generally agreed that growth occurs when temperatures are within an optimal range and dies off for warmer or cooler temperatures. Similarly, there is a band of temperature that roots can endure within, with hotter or cooler temperatures causing death. The temperature dependence should be in relative terms.

The data presented by McMichael and Burke (1996) suggests shapes of relative growth rates as a function of temperature looking like a (i) (skewed) normal or lognormal, (ii) bi-exponential, or (iii) triangular distribution. These three shapes should be provided when considering the relative growth rate, with parameters of optimal temperature and (i) standard deviation, (ii) cool and warm extinction coefficients, and (iii) minimum and maximum temperatures. Reported optimum temperatures ranged from 5 to 37 °C, with desert succulents having optima of about 30 °C. I would expect that the optimum temperature of the indigenous plants within a climatic regime is related to MAT, simply because the plants are selected to adjust to the climatic conditions.

Death rates are also affected by temperature. Nobel (1996) reports that *Agave deserti* and *Ferocactus acanthodes* have complete root death occurring at roughly 56 to 63 °C. If the root growth occurs under 15 °C warmer temperatures, the temperature tolerance is extended slightly (4 to 5 °C). *A. deserti* started exhibiting root death at about 20 °C lower than complete death, while *F. acanthodes* was completely stressed in only 8 or 9 °C. Both species have a sigmoidal dropoff, commensurate with a normal distribution for stress resistance. Similarly, sufficiently cool temperatures kill roots. A sigmoidal increase in death rate might be modelled as

$$\Lambda = 3\varsigma^2 - 2\varsigma^3, \tag{2-35}$$

$$\varsigma = \frac{T - T_i}{T_d - T_i}, \tag{2-36}$$

where Λ is the relative temperature-dependent death rate and ς is the fraction of the distance the temperature has reached between incipient stress (T_i) and completely stressed (T_d). It is theoretically tempting to use the CDF for a normal distribution, which can be approximated by a 6th-order polynomial with an error of less than 1.5×10^{-7} using equation 26.2.19 in Abramowitz and Stegun (1972). In the absence of further information, this function might be used for both hot and cool extremes.

A plant would presumably operate best at a particular temperature, with both decay of growth rates and rise of death rates symmetric about the optimal temperature. However, there are absolute temperature bounds on plant capabilities, represented by some subfreezing temperature and some near-boiling temperature. I would postulate that plants with an optimal temperature somewhere near 20 °C (for example) might actually have symmetric rates about the optimal, with a tolerance range of perhaps 25 to 40 °C on either side of the optimal. However, as plants become adapted to temperatures further from this symmetry value, the tolerance band becomes skewed. For example, MAT significantly above the symmetry range may skew the distribution about the adapted plant's optimum so that the lower tail is stretched while the upper tail is compressed. Conversely, MAT significantly below the symmetry range may skew the distribution so that the lower tail is compressed and the upper tail is stretched. For both of these cases, the overall bounds are likely to be narrower. The few data in McMichael and Burke (1996) generated this concept. Taking it one step further, I would suggest that the optimal temperature is likely to occur for temperatures in seasons with predictable moisture-uptake availability (i.e., spring in warmer climates, summer in cooler climates).

The impact of mechanical impedance on root growth rates is discussed by Bennie (1996), in which it is proposed that relative root growth rate is exponentially dependent on mechanical

impedance, using the formula

$$\frac{R}{R_{max}} = e^{-0.6931 \frac{Q_p}{Q_{0.5}}}, \tag{2-37}$$

where R is the root elongation rate, R_{max} the maximum rate at very low impedance, Q_p is the penetrometer pressure [MPa], and $Q_{0.5}$ is the penetrometer pressure corresponding to $R/R_{max} = 0.5$. Bennie (1996) further suggest that the diameter of root laterals are proportional or nearly proportional to impedance.

Soil strength would appear to provide the linkage between root length density and root diameter. The average diameter is the quantity of interest. The average diameter is calculated using the balance equation,

$$(M_o - M_d + M_g)d_{ave}^{n+1} = (M_o - M_d)d_{ave}^{n} + M_g^n d_{grow}^n, \tag{2-38}$$

where M_o is mass of old roots, M_d is mass of dying roots, M_g is mass of new roots, d_{ave} is average diameter of the old roots, d_{grow} is average diameter of the new roots, and superscripts n and $n+1$ refer to the current and next time step. There is a need for soil-strength descriptions as a function of moisture content, however, for this to be useful.

Moreshet et al. (1996) summarize information on root permeability.

Nobel (1996) demonstrates that a cost-benefit analysis on root growth allocation, using carbon taken up through photosynthesis for costs and water transpiration as the benefit, predicts quite well the measured amounts of new and old roots for *A. deserti*. The new and old roots had identical relative distributions with depth. Note that *A. deserti* roots have low respiration costs, so that the ratio of water uptake costs to carbon costs are enhanced relative to other species. Although I had conceived of a soil nutrient as the limiting nutrient, carbon should also be a good way to approach the nutrient balance cost-benefit analysis.

4/30/98 Continuation of equations for vegetation model. SAS

Allocation of nutrients is an optimization problem that the plant must solve each time step. Actual plants are genetically programmed to respond to external stimuli such as season, light levels, temperatures, and soil-moisture availability. In the vegetation model, these stimuli are accounted for through their impact on nutrient utilization.

The nutrient optimization problem is solved through a mass-balance approach with coeffi-

cients based on the marginal benefit of the allocation. The mass balance equation is stated

$$\alpha\left(\frac{\mathrm{d}\Xi_s}{\mathrm{d}\alpha}+\sum_{i=1}^{N}c_i\frac{\mathrm{d}\Xi_i}{\mathrm{d}\alpha}+W\right)=\Xi_u-\sum_{j=1}^{M}\alpha_i\frac{\mathrm{d}\Xi_j}{\mathrm{d}\alpha_j}, \tag{2-39}$$

where

- α is an adjustable weight ($0 \le \alpha \le 1$),
- c_i is the benefit/cost ratio (allocation weight),
- $\mathrm{d}\Xi_i/\mathrm{d}\alpha$ is the rate of nutrient usage in plant element i per unit change in α,
- W is net nutrient wastage,
- Ξ_u is net nutrient uptake, and
- Ξ_j is a constrained value (0 or 1) for α,

The algorithm proceeds as follows:

- Initialize by setting W to zero and consider all plant elements ($M = 0$)
- Calculate the chord-slope approximation to c_i based on the difference between maximum and zero nutrient allocation
- Repeat until done
  - Calculate α
  - Select the case where αc_i is furthest outside the valid range of 0 to 1
  - If there is no invalid case, done
  - Set c_i to the corresponding limit and move that variable to the summation on the right-hand side
- Calculate the transpiration limit for the next step based on the nutrient allocation

The benefit/cost coefficient represents the expected benefit of allocating a unit of nutrient to the plant element. A generic benefit, B, is used in the following; a good candidate for the benefit might be the expected plant-available nutrient storage. The benefit to cost for nutrient allocation to plant element i is

$$\frac{\mathrm{d}B}{\mathrm{d}\Xi_i}=\left(\frac{\mathrm{d}B_r}{\mathrm{d}\Xi_i}+\frac{\mathrm{d}B_u}{\mathrm{d}\Xi_i}\right), \tag{2-40}$$

where Ξ_i is the nutrient mass allocated to plant element i and subscripts r and u refer to changes to the benefit due to respiration and uptake, respectively. There is an additional term for overall plant storage.

The nutrient used for respiration is calculated using the optimal respiration rate per unit biomass. The benefits for uptake are evaluated for two nutrient allocations, $\Xi_i = 0$ and $\Xi_i = \Xi_r + \Xi_g$ (i.e., maximal growth and maximal death of the biomass). Uptake benefits are generally due to changes in conductance.

5/1/98 Continuation of equations for vegetation model. SAS

The components I've been referring to as root hairs really better describe "new" roots. The formulation might be changed to have "old" lateral roots, "new" lateral roots, and root hairs. Each type has characteristic properties, and both take up water. I would consider effective uptake surface area to be much smaller than actual surface area for the old roots, effective surface area to be somewhat less than actual surface area for new roots, and effective surface area to be about equal to actual surface area for root hairs. The conversion between new and old roots follows a mass balance approach, with the conversion rate dependent on average new-root age. Average new-root age is calculated using

$$(M_n - M_d - M_c + M_g)a_{ave}^{n+1} = (M_n - M_d - M_c)(a_{ave}^{n} + \Delta t), \tag{2-41}$$

where M_n is mass of new roots, M_d is mass of dying roots, M_c is mass of roots switching from new to old, M_g is mass of newly generated roots, a_{ave} is average age of the new roots, Δt is size of the time step, and superscripts n and $n+1$ refer to the current and next time step. Note that newly generated roots have zero age.

Several other approaches might be used to handle conversions from new to old roots. A straightforward way to handle the problem would be to bin the ages. For example, if the time step was one day and roots switched from new to old after 60 dy, 10 6-dy bins might be constructed. Each time step, 1/6 of the contents of each bin might be passed to the next bin, with the contents of the last bin becoming old roots. Death is applied proportionately to each bin. Alternatively, the new root ages might be considered to have a normal distribution, with a mean and standard deviation. The mean and standard deviation could be used to calculate the conversion to old, updating both with the newly generated roots.

5/19/98 Equations for soil-genesis model. SAS

During the trip to YM the past several days, Oliver Chadwick and I had several discussions regarding appropriate soil-genesis models for YM. We agreed that an attractive approach is to lay out a general formulation, then emphasize the aspects that are more appropriate for YM in particular.

Table 2-1: Representative soil properties for YM and Phinney Canyon.

Parameter	Yucca Mountain	Phinney Canyon
K_{sat} (cm/d)	106	10.8
k (cm^2)	1.3×10^{-8}	2.2×10^{-9}
α (cm^{-1})	0.075	0.02
P_0 (gm/cm-s^2)	1.3×10^{4}	4.9×10^{4}
n	1.89	1.41
m	0.47	0.29
θ_s	0.41	0.45
θ_r	0.065	0.067

The issue is of considerable importance, as soil depth and composition have a significant impact on MAI. For example, consider two representative hillslopes, representing typical YM and typical Phinney Canyon hillslopes, with soil-filled fractured bedrock underlying a soil with rock fragments. The soil at YM is a sandy loam with roughly half rock fragments, while at Phinney Canyon the soil is a silty loam with about a third rock fragments and roughly twice the depth. Typical parameters for these soil types are in Table 2-1: Assume soil depth is 25 cm at YM and 50 cm at Phinney Canyon. Account for rock fragments by assuming that θ_s and θ_r are 0.205 and 0.0325 (YM) and 0.3015 and 0.449 (Phinney Canyon), yielding total pore space of 4.1 cm/cm^3 (YM) and 12.06 cm/cm^3 (Phinney Canyon).

Several simulations were presented in Table ??, with calcite- and soil-filled properties fairly similar in nature. With calcite-filled fractures, a base case of 25 cm cover and 0.2 porosity has MAI of 12 mm/yr, while 50 cm cover with 0.3 porosity has MAI of 4.9 mm/yr (approximate reduction of 0.4). A base case of 25 cm cover and P_0 of 10^4 has MAI of 18 mm/yr while 50 cm cover and P_0 of 5×10^4 gm/cm-s^2 has MAI of 0.13 mm/yr (approximate reduction of 0.0072). A base case of 25 cm cover and K_{sat} of 10^{-8} cm^2 has MAI of 8.6 mm/yr while 50 cm cover and K_{sat} of 10^{-9} cm^2 has MAI of 11 mm/yr (negligible increase expected if K_{sat} is 2×10^{-9} cm^2). Similarly, there is little impact due to van Genuchten m. If the effects of soil depth, porosity, and P_0 can be superimposed, the combination results in a decrease in MAI by about 2.5 orders of magnitude for the current climatic conditions.

The work will build upon the soil genesis model that I developed several years ago. That model was formulated before I had heard that most of the soil currently at YM is of æolian origin. The model assumes that soil is generated by weathering of the bedrock, with weathering exponentially decreasing with soil depth. Soil moves downslope according to creep, with rate of movement

proportional to bedrock slope. Soil is also moved according to overland flow, characterized by one steady-state storm and one sediment grain size. As there is only overland flow for a very short fraction of the time in the YM area, the sediment transport is time-weighted.

The structure and approach of the new model will be generally similar to the first model, only significantly more sophisticated in the physical processes considered. Instead of one generic soil, several size classes will be considered, each characterized by their respective mass fraction. Each size class will provide a source for every smaller size class as weathering occurs. Two types of external source material will be considered, æolian dust and rocks plucked from the bedrock. Downhill movement will occur through creep and overland flow, as before, but will also occur according to slump based on the critical angle. The soil profile may also be discretized into several computational layers.

Size classes

The preliminary discussion suggested that several size classes might be considered, including cobbles, gravel, coarse sand, fine sand and silt, clay (< 2 μm), and organic content. Dani suggested that it might be more attractive to use a particle-size distribution, characterized with perhaps a few means and standard deviations to capture modes. If weathering processes can be described as functionally dependent on particle size, the evolution of the statistical distribution can be recreated using a detailed histogram reconstructed from the statistics.

For example, assume that the particle-size distribution is lognormally distributed. Generating a histogram of perhaps a hundred bins, the weathering of the particles in each bin is straightforward, resulting in an output particle distribution for the bin. Each of the input bins creates an output distribution, which are accumulated into an overall output distribution. The statistics of the output distribution are then calculated and used for the next time step. The procedure is particularly useful if weathering-rate tables are formulated as a statistical description of the distribution of output particle sizes.

Weathering

The rates of the weathering and movement processes are typically dependent on temperature, moisture content, and perhaps organic content or vegetation density. The rate law for weathering

will be of the standard exponential form,

$$\frac{\partial \omega_i}{\partial t} = \alpha_{ij}\omega_j, \tag{2-42}$$

where subscripts i and j represent the finer classes and the larger class, respectively, ω represents the mass fraction of the size class, and α_{ij} represents the rate constant. The rate constant is formed by adding physical weathering and chemical weathering rates. Physical weathering is most important for the large particles, scaling with the inverse of particle volume, while chemical weathering scales with particle surface area.

As the rates are dependent on the number of freeze-thaw cycles (for physical weathering) and on temperature, moisture content, and organic content (for chemical weathering), all of which vary rapidly relative to the anticipated time steps of at least centuries, it is necessary to use effective rates. The effective rates will be calculated by (i) forming a table of weathering rate (combined physical and chemical) as a function of freeze-thaw cycles, temperature, moisture content, and organic content; and (ii) calculating the fraction of the time step that each rate is active. The effective rate for each size breakdown is then

$$\alpha_{eff} = \sum_{i=1}^{N} \alpha_i \Delta t_i / \sum_{i=1}^{N} \Delta t_i, \tag{2-43}$$

where α_{eff} is the effective weathering rate, α_i is the weathering rate for bin i, and Δt_i is the time spent in bin i during the time step ($\sum_{i=1}^{N} \Delta t_i = \Delta t$).

It may be impractical to try to solve for soil moisture and temperature in each computational element for thousands of years, although perhaps a simple bucket model (as used by A. Flint of the United States Geological Survey (USGS)) might do the trick and could be explored in future work. Instead, the results from the many 1D simulations already performed will be used to estimate seasonal mean effective moisture and mean soil temperature as a function of MAP, MAT, hydraulic properties, and solar aspect. In order to use the simulations, the hydraulic characteristics and pore volume for the fine fraction (< 2 mm) will be used to translate between the 1D simulations and the soil column. The simulations may also be used to estimate the number of freeze-thaw cycles as a function of soil depth, MAP, and MAT, or an analytic expression may be used for temperature in a 1D column as a function of a sinusoidal forcing at one end. A synthetic history of MAP and MAT will be required, but not at a finer scale than a decade (all simulations are valid for a decade). The primary difficulty is that the simulations performed to date may be somewhat wetter than they would have been if vegetation was considered. As the rates are more sensitive to temperature than moisture (when sufficient moisture is present), the discrepancy may not have a great deal of impact on soil genesis. Greater impact would be expected under cooler and wetter conditions, where evaporation is less efficient at drying the soil.

Creep

Creep is dependent on soil-component fractions, moisture content, temperature, and vegetation density. Creep is relatively slow when large fragments are present with minimal fines, but as the fine component increases the large fragments are lubricated and creep accelerates. Similarly, soil moisture lubricates creep by decreasing effective pressure. On the other hand, creep decreases as vegetation increases, since roots are effective at holding together soil masses. Creep is drastically reduced when soil moisture is frozen, but freeze-thaw cycles enhance creep by jiggling soil particles.

As with weathering, resistance to creep may be highly time-dependent relative to the size of the time step. An effective resistance may be calculated using the same time-averaging approach as in Equation 2-43.

Slumping

One of the primary components of downhill mass wasting is through sudden slumping (i.e., landslides). Obviously it is impractical to attempt to use a time step that resolves slumping. It is reasonable, however, to assume that the soil column saturates at least once during a time step of centuries. Accordingly, each time step the entire domain will be inspected for the critical angle under saturation and volumes where the critical angle is exceeded will be slumped. This approach succeeds when the time step is long relative to the intervals between saturation events. Assuming that saturation exists, soil composition is the primary determinant of critical angle.

One factor that may increase slumping is earthquakes during saturation conditions. Earthquakes are rare, as are saturation conditions (at least during current climatic conditions). Perhaps a small probability of having an earthquake could be factored in, which would result in a probability of having a decreased critical angle and slumping a somewhat greater proportion of the slopes.

Sources

Two soil-component sources will be considered, æolian dust and bedrock that physically weathers into soil components. The dust source has a regional component and a local component dependent on nearby playas. Dust input is dependent on climate, as cooler and moister conditions form lakes in playas, thereby decreasing dust production. Dust deposition is dependent on particle settling

rates and wind velocity, so that one would expect that dust accumulation might be greater in the relatively calm washes than on the windier ridgetops. As a first crack, a spatially uniform deposition will be considered.

The bedrock type will determine the generated particle-size distribution, with (i) the caprock forming a bimodal distribution (large boulders and lots of sands), (ii) non- to moderately welded units forming fines, (iii) nonlithophysal units forming large chunks, and (iv) lithophysal units forming smaller chunks. As discussed before, physical weathering depends on freezing and thawing. Accordingly, physical weathering decreases exponentially with depth, consistent with the exponential decrease in temperature variation with depth.

Overland flow and transport

The procedures followed in the first model, with one representative storm occurring for a representative length of time, may be modified to account for several storm sizes. Further, transport will be required to account for the range of particle sizes. Again, a time-weighting approach similar to Equation 2-43 will be used to create effective transport due to overland and stream flow. An estimate of storm frequency and flow duration will be required. It may be desirable to tap into Woolhiser's expertise here.

Carbonate modeling

Some of the discussion related to the deposition, dissolution, and redistribution of carbonates (caliche and fracture fillings). Carbonates strongly affect net infiltration. When carbonates or other fillings are present, simulations to date suggest that MAI is reduced in shallow soils but enhanced in deeper soils relative to the situation with unfilled fractures. Carbonates are present at many locations at YM but are lacking at others, and the team has not yet been able to develop a heuristic for predicting the carbonate level at any particular location. A predictive model may help to shed light on the issue.

This issue adds a significant level of complexity and would not be addressed until the soil model is fairly well developed. I suspect that it might be desirable to create a simple bucket model to handle the combination of soil moisture, temperature, wetting-pulse depth, soil carbon dioxide, and carbonate deposition.

Numerical issues

The first model used the 30 m by 30 m Digital Elevation Model (DEM) that is standard for YM. This resolution is quite coarse, particularly in upper washes where the stream channel is only 1 m wide. It may be more appropriate to create a mesh with triangles, which can easily be done with *Matlab*, with a line along the channel bottom. Flow routing is less ambiguous with triangles than with squares, and node spacing can be adjusted to fit the slope and/or curvature.

Vertical resolution of the profile has not been completely decided on. It may be appropriate to have a uniformly mixed profile for first experiments, with perhaps a few computational layers in later work. The uniformly mixed profile fits better with the idea of using the 1D simulations already generated. Vertical variation does occur due to the natural buoyancy of large rocks in the presence of fines, as was observed in talus-slope dissections. Perhaps we could consider the possibility of characterizing vertical variability with a distribution of particle-size distributions. One might assume that there is a parabolic distribution for particle sizes in talus, for example, with the mode shifting from large particles at the top to smaller particles at the bottom.

References

Abramowitz, M. and I. A. Stegun. 1972. *Handbook of Mathematical Functions.* New York, NY: Dover Publications, Inc.

Beatley, J. C. 1974. Phenological Events and Their Environmental Triggers in Mojave Desert Ecosystems. *Ecology 55*, 856–863.

Bennie, A. T. P. 1996. Growth and Mechanical Impedance. In Y. Waisel, A. Eshel, and U. Kafkafi (Eds.), *Plant Roots: The Hidden Half*, pp. 453–470. New York, NY: Marcel Dekker, Inc.

Bird, R. B., W. E. Stewart, and E. N. Lightfoot. 1960. *Transport Phenomena.* New York, NY: John Wiley & Sons.

Caldwell, M. M. 1994. Exploiting Nutrients in Fertile Soil Microsites. In M. M. Caldwell and R. W. Pearcy (Eds.), *Exploitation of Environmental Heterogeneity by Plants*, Chapter 12, pp. 325–347. San Diego, CA: Academic Press.

Fitter, A. H. 1994. Architecture and Biomass Allocation of Root Systems. In M. M. Caldwell and R. W. Pearcy (Eds.), *Exploitation of Environmental Heterogeneity by Plants*, Chapter 11, pp. 305–323. San Diego, CA: Academic Press.

Kozlowski, T. T. and S. G. Pallardy. 1997. *Physiology of Woody Plants* (Second ed.). New York, NY: Academic Press.

McMichael, B. L. and J. J. Burke. 1996. Temperature Effects on Root Growth. In Y. Waisel, A. Eshel, and U. Kafkafi (Eds.), *Plant Roots: The Hidden Half*, pp. 383–396. New York, NY: Marcel Dekker, Inc.

Moreshet, S., B. Huang, and M. G. Huck. 1996. Water Permeability of Roots. In Y. Waisel, A. Eshel, and U. Kafkafi (Eds.), *Plant Roots: The Hidden Half*, pp. 659–678. New York, NY: Marcel Dekker, Inc.

Nobel, P. S. 1996. Ecophysiology of Roots of Desert Plants, with Special Emphasis on Agaves and Cacti. In Y. Waisel, A. Eshel, and U. Kafkafi (Eds.), *Plant Roots: The Hidden Half*, pp. 823–844. New York, NY: Marcel Dekker, Inc.

Sonnenthal, E. L., C. F. Ahlers, and G. Bodvarsson. 1997. Fracture and Fault Properties for the UZ Site-Scale Flow Model. In G. S. Bodvarsson, T. M. Bandurraga, and Y. S. Wu (Eds.), *The Site-Scale Unsaturated Zone Model of Yucca Mountain, Nevada, for the Viability Assessment*, LBNL-40376, Berkeley, CA, pp. 7–1–7–33. Lawrence Berkeley Laboratory.

Waisel, Y., A. Eshel, and U. Kafkafi (Eds.). 1996. *Plant Roots: The Hidden Half* (Second ed.). New York, NY: Marcel Dekker, Inc.

3. Thermal Hydrology KTI

Account Number: **20-1402-661**
Collaborators: **Goodluck Ofoegbu, Ronald T. Green**
Directories: **As noted**

Objective: The overall objective of the thermal hydrology KTI is to assess the impacts of possible thermal loading due to the proposed YM repository on the subsurface hydrology. The near-field KTI also is investigating potential effects of the thermal loading, but with perhaps more of an emphasis on the impact on geochemistry and hence hydrology. Out of the entire hydrology-thermal-mechanical-chemical (HTMC) group, the thermal hydrology KTI is essentially HT while the near-field KTI is more HTC.

7/5/98 Initial entry. SAS

Background

Last week Goodluck contacted me regarding a modeling task with a milestone date at the end of August. The task evaluates two-phase flow within a fracture under thermal loads from the repository. The approach he has used thus far is to have detailed modeling in a fairly restricted area (roughly 20 m laterally by roughly 50 m vertically). Apparently the approach is extremely computationally demanding, due to the small elements (hence small time steps) required to accurately handle the fracture.

The idea that Goodluck had was to handle the rock matrix with a simplified approach, using a Boundary Integral Equation Method (BIEM) approach. A BIEM approach is most effective when the domain is not discretized, rather placing any mesh along discontinuities (boundaries are special cases of discontinuities). Elimination of domain discretization is accomplished by use of a Green's function specific to the equation. Such a Green's function is available for only a few (linear or quasi-linear) equations. The steady-state potential equation is particularly useful, as the Green's function is easy to use in 1D, 2D, and 3D. There are two approaches for time-dependent potential problems with fixed boundaries: (i) use a time-dependent Green's function (I recall from about ten years ago that this approach is fairly inaccurate and clumsy); or (ii) take the Laplace transform of the problem, solve in Laplace space with the appropriate Green's function, and (numerically) invert.

The steady-state potential equation is often used for thermal conduction or isothermal saturated flow. It should also be appropriate for isothermal vapor diffusion. At YM, unsaturated conditions exist. When the unsaturated conductivity is described by an exponentially decaying function of potential, the problem is quasilinear and can be handled using a special Green's function, at the cost of iteration when the boundaries are not completely first-type boundaries. If the range in potential within the domain is sufficiently small, any conductivity can be approximated using the exponential function. In the TSw, the matrix is essentially saturated but the fractures are quite unsaturated, so that one could either approximate the conductivity from the equivalent-continuum assumption or use K_{sat} in the matrix and provide discrete fractures to handle flows in excess of matrix K_{sat}.

The potential equation is most straightforward to use when all coefficients within the domain are constants (i.e., conductivities are spatially invariant) and all nonlinearities are confined to the discontinuity mesh. Piecewise-constant coefficients are straightforwardly handled by discretizing the boundaries between the discontinuities. Arbitrarily varying coefficients require domain discretization, negating much of the BIEM advantage, although some fairly restrictive conductivity distributions can be handled without domain integration.

For immiscible free-surface problems where the solution within the domain is rapid relative to the movement of the boundary (i.e., a quasi-steady state exists), the time-varying solution can be obtained by determining the velocity of the free surface at any instant and updating the position of the free surface. Classic examples of this approach are the phreatic-surface problem and the moving sharp-interface problem. The approach requires that two compatibility equations are available relating potential and the gradient of potential normal to the interface (e.g., $\phi_1 = \phi_2$, $q_1 = q_2$).

Definition of Problem

The particular problem that Goodluck is considering is a single vertical fracture within a porous matrix. At the top of the fracture, a liquid flux is applied. A drift with heat source is located at the bottom of the fracture, raising some portion of the domain to above boiling. It is desired to quantify the liquid flux into the drift as a function of time; if no liquid reaches the drift, the distance that the liquid penetrates in the fracture is desired as a function of time.

As noted above, the solution procedure using MULTIFLO is too computationally demanding for significant analysis. The original idea put forth by Goodluck is to approximate energy transport

in the matrix as occurring solely through conduction. Liquid (film flow) and vapor are considered in the fracture, but no mass is allowed to cross the matrix-fracture interface. A solution procedure was developed by Frank Dodge for liquid, vapor, and energy fluxes within the fracture given the thermal state of the matrix at the fracture boundary.

In addition to the numerical difficulties exhibited by MULTIFLO, Goodluck expressed dissatisfaction with some of the properties of the solver for the fracture system. Several actual or potential weaknesses with the approach are apparent after cursory examination (noting that it is quite possible I may have missed some point of the development). The method assumes that the fluid mixture in the fracture has a different temperature than the rock matrix, and the mixture has uniform temperature throughout the fracture. It appears that continuity of total water flux is not assured (i.e, liquid poured in the top of the fracture may not escape through the bottom of the fracture in the form of vapor). The proposed neglect of mass exchange across the matrix-fracture interface may seriously misrepresent vapor fluxes. No mention was made of the dependence of thermal conductivity on moisture content.

Goodluck expressed a desire to examine approaches that might be extended past the current problem. In addition, I have long wanted to develop a technique that could be used to examine discrete-fracture flows under ambient flow conditions, with particular interest in fracture-drift interactions. I believe that the BIEM can be developed into a powerful approach to handle both situations. The following approach can be used for both 2D and 3D simulations (although the equations will be specialized for 2D until further interest is expressed). The numerical approach can be applied to the thermal problem, the ambient problem, and discrete-fracture problems in the saturated zone (in order of increasing simplicity). The approach is developed for the 2D thermal problem, as the other physical scenarios represent simplifications of the overall method and the 3D scenarios are identical in general approach, simply swapping out the Green's functions for the 3D equivalent and using triangles instead of linear elements.

General Boiling-Isotherm Solution Approach

The philosophy of the BIEM approach developed here is to simplify the physics while hopefully not mutilating them.

Once boiling temperatures are widely reached there are three zones (upper nonboiling, middle boiling, and lower nonboiling) separated by two boiling isotherms. The top boundary condition for the upper nonboiling zone is specified flux and temperature, while the bottom boundary condi-

tion for the lower nonboiling zone is specified pressure and perhaps temperature. In all zones, the non-vapor component of the gas phase is assumed to be hydrostatically distributed (no bulk movement). It is assumed that the boiling isotherm represents a sharp transition between a dessicated zone with vapor movement but no liquid movement, and a nearly saturated zone with liquid movement but no vapor movement. Within discrete fractures, this restriction is lifted but the fracture only can exchange mass with the matrix based on the phase in the matrix (i.e., in the boiling zone only vapor can exchange while in nonboiling zones only liquid can exchange).

It is assumed that both temperature and fluids redistribute quickly relative to the movement of the isotherm, so that a quasi-steady state exists for all components. Drifts are modeled as point energy sources.

When discontinuities separate the region into bounded parcels, it can be advantageous to artificially separate the parcels at the penalty of doubling the unknowns along the discontinuity. If the Green's function is different in each region, then the separation must take place (e.g., if the discontinuity separates a saturated zone from an unsaturated zone). The resulting matrix equation is larger than before but no longer full. In this case, the BIEM for a given potential field requires that four variables are defined at a discontinuity: the potential on each side of the discontinuity and the gradient on each side of the discontinuity. Additional equations are included to the system to ensure compatibility of potential and flux. Typical compatibility equations ensure that potential is continuous and flux is continuous, although one can simulate impermeable or semipermeable features, highly permeable features, sources/sinks, and specified potentials.

It is also possible to treat the discontinuities as interior to the domain, but only the jump in potential and the jump in gradient remain as unknowns (one supplemental compatibility equation is required). The method results in a fully populated matrix.

One mass balance compatibility equation at the isotherm links liquid pressure to vapor pressure using the vapor-pressure reduction for unsaturated porous media. The other relates the velocity of the isotherm to the mass flux rates and mass transfer rate across the isotherm, which are in turn related to energy transfer across the isotherm. The primary unknowns are pressure and pressure gradient for a phase.

The temperature at the isotherm is specified on both sides of the isotherm to be the boiling temperature, so that the primary unknowns are the temperature gradients on either side of the isotherm or source strength along the line feature.

General Fracture Solution Approach

Fractures represent potential fast pathways for fluxes as well as discontinuities. It is assumed that pressure and temperature are continuous between the fracture and the matrix. The fracture is discretized into line segments (2D) or triangles (3D), with potential linearly varying between nodes, normal derivative of potential constant over an element, and source/sink terms constant over the portions of the element associated with a node (e.g., half the element for lines and one-third of the element for source/sink terms). If an unknown potential or source/sink term is required, a contour integral is performed with the base point at the node. If an unknown normal derivative is required, a contour integral is performed with the base point at the element centroid.

Within the fracture, standard equations for fluid and energy flow are used. It is assumed that liquid and vapor pressures are in equilibrium, both within the fracture and between fracture and matrix, and the equilibrium is a function of temperature. If necessary, it is possible to consider the effect of a skin between fracture and matrix limiting the mass exchange. It is further assumed that relative permeability and saturation within the fracture is a function of pressure and temperature.

Compatibility at the Boiling Isotherm

At the isotherm, pressure in the vapor is determined by saturated vapor pressure at the boiling temperature times the relative humidity (considered solely as a function of the liquid pressure). The compatibility of pressures at the boiling isotherm is nonlinear. A reasonable approach for this nonlinearity is to assume an initial liquid pressure distribution along the isotherm and solve for the increment in pressure. The procedure uses the linearization

$$P_v^{m+1} \approx P_v^m + \frac{\mathrm{d}P_v}{\mathrm{d}P_l}\Delta P_l, \tag{3-1}$$

where liquid and vapor are denoted by l and v, P is pressure, m represents the iteration level, and the unknown being determined is ΔP_l.

The temperature at the isotherm is specified as the boiling temperature. The boiling temperature might be considered a function of pressure, represented by the sum of air pressure and vapor pressure. Note that air pressure is assumed hydrostatic (a small correction).

The compatibility equations for mass and energy fluxes are coupled through the velocity of the isotherm. The velocity, V, of a discontinuity (shock) in a phase is

$$V = \frac{q_2 - q_1}{\varepsilon(\theta_2 - \theta_1)}, \tag{3-2}$$

where q is flux, ε is porosity, θ is saturation (or mass fraction times saturation, for vapor), and the subscript represents the side of the discontinuity. Note that as the flux equilibrates, the velocity of the discontinuity goes to zero. Similarly, the velocity of an energy discontinuity between liquid and vapor is

$$V = \frac{E_{UZ} - E_{TZ} - h_{fg} q_c}{C_{UZ} - C_{TZ}}, \tag{3-3}$$

$$E = c_l q_l + c_v q_v - K \frac{\partial T}{\partial n}, \tag{3-4}$$

where E represents total energy flux; UZ and TZ denote the unsaturated zone (liquid) and thermal zone (vapor), respectively; q_c is the mass flux across the interface (positive for condensation of vapor at the interface); c_l and c_v represent enthalpy per unit mass of liquid and vapor; K is the bulk thermal conductivity; h_{fg} is the enthalpy associated with phase change; and C represents total energy capacitance.

Assuming liquid is on side 2 and vapor on side 1, the velocity of the discontinuity can be represented as

$$V_l = R_l(q_l - q_c), \tag{3-5}$$

$$V_v = R_v(q_c - q_v), \tag{3-6}$$

$$V_e = C_l q_l - C_v q_v - C_c q_c + \epsilon, \tag{3-7}$$

$$R_l = 1/\varepsilon(\theta_{l2} - \theta_{l1}), \tag{3-8}$$

$$R_v = 1/\varepsilon(\theta_{v2} - \theta_{v1}), \tag{3-9}$$

$$C_l = c_l/(C_{UZ} - C_{TZ}), \tag{3-10}$$

$$C_v = c_v/(C_{UZ} - C_{TZ}), \tag{3-11}$$

$$C_c = h_{fg}/(C_{UZ} - C_{TZ}), \tag{3-12}$$

$$\epsilon = \left(K_{UZ} \frac{\partial T_{UZ}}{\partial n} - K_{TZ} \frac{\partial T_{TZ}}{\partial n} \right) / (C_{UZ} - C_{TZ}). \tag{3-13}$$

For compatibility, $V_l = V_v = V_e$.

Equating the velocities from liquid and vapor,

$$q_c = \frac{R_l q_l + R_v q_v}{R_l + R_v}. \tag{3-14}$$

Equating the velocities from liquid and energy, and substituting for q_c,

$$q_l[R_l(R_v - C_l + C_c)] = -q_v[C_v(R_l + R_v) + R_v(C_c - R_l)] + \epsilon(R_l + R_v). \tag{3-15}$$

The relationship between liquid flux in the nonboiling zone and vapor flux in the boiling zone depends on the temperature gradients on both sides of the isotherm as well as the storage capacities for mass and energy.

The energy-flux balance compatibility condition is not explicitly specified. The specified-temperature condition along the isotherm is equivalent to an energy source/sink along the isotherm, with the magnitude of the source determined in the solution process. The magnitude of the source is implicitly compatible with the mass fluxes through the velocity constraints.

Once the solution has been determined, the isotherm is updated using any of the expressions for velocity:

$$x^{n+1} = x^n + V\Delta t. \tag{3-16}$$

Note that the velocity solved for is actually the velocity magnitude in the direction normal to the isotherm.

Matrix Governing Equations

The quasisteady governing equation for vapor flow in the boiling zone is

$$\nabla \cdot [\rho_v k\lambda(\nabla P + \rho g \nabla z)] + \nabla \cdot D\nabla\rho_v = 0, \tag{3-17}$$

where P is gas pressure, k is intrinsic permeability, λ is mobility (relative permeability divided by viscosity), g is acceleration due to gravity, z is elevation, D is the diffusion constant, and ρ_v is vapor density.

Assuming the ideal gas law is valid,

$$P = \rho RT, \tag{3-18}$$

and the air component is pneumostatic ($\nabla P_a + \rho_a g \nabla z = 0$),

$$\rho_v \nabla P = \frac{R}{2}\nabla T \rho_v^2 = \frac{R}{2}(T\nabla\rho_v^2 + \rho_v^2 \nabla T). \tag{3-19}$$

Leaping to a gross approximation for the equation coefficients, by assuming that it is acceptable to use a representative mean value for T, k, λ, ρ, and D, the governing equation can be written

$$A_1\nabla^2\rho_v^2 + A_2\nabla^2 T + A_3\nabla^2 z + A_4\nabla^2\rho_v = 0, \tag{3-20}$$

$$A_1 = \left\langle \frac{RTk\lambda}{2} \right\rangle, \tag{3-21}$$

$$A_2 = \left\langle \frac{R\rho_v^2 k\lambda}{2} \right\rangle, \tag{3-22}$$

$$A_3 = \left\langle \rho_v^2 k\lambda \right\rangle, \tag{3-23}$$

$$A_4 = \langle D \rangle. \tag{3-24}$$

The braces denote the representative value. The representative values might be obtained by averaging several point values strategically located within the domain after each nonlinearity iteration. The new governing equation is a sum of Laplacians, each of which can be written as a boundary integral.

The governing equation for energy in the boiling zone can be written

$$\nabla \cdot (Cq) - \nabla \cdot (K_e \nabla T) = 0, \tag{3-25}$$

$$q = -A_1 \nabla \rho_v^2 - A_2 \nabla T - A_3 \nabla z, \tag{3-26}$$

where C is specific enthalpy for the air mixture, q is flux of the air mixture, and K_e is thermal conductivity. Assuming all coefficients are spatially invariant allows the energy equation to be calculated as a sum of Laplacians that can be solved using boundary integrals. Presumably the gradients of the variables are relatively small in the problem of interest so that the use of a representative value is not so bad.

Note that the Green's function for a Laplacian is (Liggett and Liu, 1983)

$$G = \ln r \qquad \text{in 2D}, \tag{3-27}$$

$$G = 1/r \qquad \text{in 3D}. \tag{3-28}$$

The mass and energy equations represent a coupled system of two equations with (essentially) two unknowns (ρ_v and T).

In the nonboiling zone, the mass balance equation is stated

$$\nabla \cdot K(\nabla P + \rho g \nabla z) = 0. \tag{3-29}$$

If $K = K_{sat} \exp(\alpha P)$, the governing equation can be converted to

$$\nabla^2 \phi = s^2 \phi, \tag{3-30}$$

which is quasilinear, with the following substitutions

$$\phi = \exp(-sz) \int_{-\infty}^{P} K \, dP = \frac{K_{sat}}{\alpha} \exp(\alpha P - sz), \tag{3-31}$$

$$s = \frac{\rho g \alpha}{2}. \tag{3-32}$$

The correspondence between fluxes is

$$\frac{\partial q}{\partial n} = K(P) \frac{\partial P}{\partial n} = \exp(sz) \left[\frac{\partial \phi}{\partial n} + s\phi \frac{\partial z}{\partial n} \right]. \tag{3-33}$$

The Green's function for the quasilinear case is (Pullan and Collins, 1987)

$$G = K_0(sr) \qquad \text{in 2D,} \tag{3-34}$$

$$G = \exp(-sr)/r \qquad \text{in 3D,} \tag{3-35}$$

where K_0 is the modified Bessel function of the second kind of order 0. Any effects of temperature on K and ρ are neglected.

The energy balance equation in the nonboiling zone is

$$\nabla \cdot (K_e \nabla T) = 0. \tag{3-36}$$

In the nonboiling zone, mass and energy fluxes are assumed independent. The restriction of independence is a consequence of the quasilinear approximation for unsaturated flow.

Fracture Governing Equations

The same governing equations apply in the fractures as in the matrix, except that mass fluxes are two-phase rather than one-phase. The approximations of constant coefficients need only be applied within each element. The fracture equations should be quite standard. However, it is desirable to have pressure and temperature continuity from fracture to matrix. If these are not continuous (a fracture coating, for example), the resistance of the layer must be characterized. If the connection is totally shut off, then the matrix and fracture must have twice as many unknown values.

Interchange with the matrix is handled through distributed sources/sinks centered on fracture nodes. These sources and sinks enter into the compatibility equations for the matrix and are directly applied in the fracture equations.

General BIEM Approach

The following section is modified from Stothoff (1991).

The Green's function, or direct boundary element, approach is followed herein, due to the generality of the approach and the ease of incorporating extensions to the basic formulation. An excellent derivation of the approach is presented by Liggett and Liu (1983), along with associated computer code.

The Green's function approach takes advantage of Green's theorem. The first form of Green's theorem states that, for a function V satisfying the divergence theorem

$$\int_{\Omega} \nabla \cdot V \, d\Omega = \int_{\sigma} n \cdot V \, d\sigma, \tag{3-37}$$

where V is represented by $V = \phi_1 \nabla \phi_2$, and both ϕ_1 and ϕ_2 are scalar functions of space,

$$\int_{\Omega} \nabla \cdot \phi_1 \nabla \phi_2 \, d\Omega = \int_{\sigma} n \cdot \phi_1 \nabla \phi_2 \, d\sigma. \tag{3-38}$$

A symmetric form of this is derived by applying the first form of the Green's theorem to the second part of the left hand side, reversing the role of ϕ_1 and ϕ_2, resulting in the second form of the Green's theorem

$$\int_{\Omega} (\phi_1 \nabla^2 \phi_2 - \phi_2 \nabla^2 \phi_1) \, d\Omega = \int_{\sigma} n \cdot (\phi_1 \nabla \phi_2 - \phi_2 \nabla \phi_1) \, d\sigma. \tag{3-39}$$

If an appropriate function G is found which satisfies the relationship

$$\nabla^2(G) = \delta(p - d), \tag{3-40}$$

where p represents a base point and d represents a field point, it is called the Green's function for the problem, and Equation 3-39 may be written in the form

$$\int_{\Omega} (\phi \nabla^2 G - G \nabla^2 \phi) \, d\Omega = \int_{\sigma} n \cdot (\phi \nabla G - G \nabla \phi) \, d\sigma. \tag{3-41}$$

The second part of the volume integral is identically zero, and the Laplacian in the first part of the volume integral may be replaced by the Dirac delta function, resulting in

$$\alpha \phi(p) = \int_{\sigma} \left(\phi(d) \frac{\partial G}{\partial n}(p, d) - G(p, d) \frac{\partial \phi}{\partial n}(d) \right) d\sigma, \tag{3-42}$$

where the notation $\partial\phi/\partial n$ is shorthand for the expression $n \cdot \nabla\phi$. This is the basic representation for the direct boundary integral method used herein. With this representation, ϕ may be found at any base point p by setting the field point d to the locus of points defining the surface. For the free space Laplace equation in two dimensions,

$$G = \frac{\ln(r)}{2\pi}; \tag{3-43}$$

and for the free space Laplace equation in three dimensions,

$$G = \frac{1}{4\pi r}, \tag{3-44}$$

where $r = |p - d|$. The coefficient α depends on the location of the point p relative to the jump in potential along σ, as it arises from the exclusion of the singular point $p = d$ from Ω; α is 0 if p is outside Ω, 1 if p is wholly within Ω, and $\frac{1}{2}$ if on a smooth portion of the boundary.

If p lies at a non-smooth portion of the boundary, α corresponds to the interior angle the boundary makes at the point. Note that $\partial\phi/\partial n$ does not have a unique value at points where the boundary is not smooth, as there is no well-defined normal direction! This difficulty is handled by defining $\partial\phi/\partial n$ by pieces, with discontinuities occurring at angle points.

Equation 3-42 expresses the value of potential at a point as a sum of a weighted integral of the potential around σ and a weighted integral of the normal derivative of the potential around σ. If both of these values are known, in theory the potential may be found at any internal or boundary point. Liggett and Liu (1983) report that solutions tend to deteriorate near σ, due to what is termed the "boundary layer" effect. This arises due to the sharp change in α at σ, and care must be taken to minimize this numerical artifact.

In a well-posed problem, either ϕ or $\partial\phi/\partial n$ is defined around σ. For boundary integral methods to work, the missing boundary values must be available; in order to generate the missing set of boundary values, a number of strategies are commonly used. In the most common approach, both ϕ and $\partial\phi/\partial n$ are discretized into point values and interpolating functions between the point values, with a resultant set of N unknown values. Equation 3-42 is applied directly at the N locations where an unknown value is desired, resulting in a complete set of N equations in N unknowns. This is denoted by the matrix equation

$$H\phi = G\frac{\partial\phi}{\partial n}, \tag{3-45}$$

where H comprises the integrals, dependent on the geometry of the problem, which multiply the discretized point values of ϕ, and G comprises the corresponding integrals for the point values of $\partial\phi/\partial n$. In practice, this equation is rearranged so that known values are multiplied through and placed on the right hand side, and unknown values are moved to the left hand side, resulting in the familiar system of equations

$$Au = b, \tag{3-46}$$

where A is a square matrix, u is the vector of unknowns, and b is a vector of known information.

If the Green's function is satisfied identically along a portion of σ, the corresponding portion of σ need not be discretized; for example, a Green's function can be constructed which explicitly takes into account no-flow conditions on a boundary, using the method of images. The free space

Green's function accommodates infinite boundaries, and only *finite* boundaries need be discretized. This property is in stark contrast to domain method requirements.

Another approach uses the derivative of Equation 3-42 to evaluate the normal derivative at the boundary directly. The derivative of ϕ in an arbitrary direction n_p may be written in the form

$$\alpha \frac{\partial \phi}{\partial n_p}(p) = \frac{\partial}{\partial n_p} \left[\int_\sigma \left(\phi(d) \frac{\partial G}{\partial n}(p,d) - G(p,d) \frac{\partial \phi}{\partial n}(d) \right) \mathrm{d}\sigma \right]. \tag{3-47}$$

Equation 3-47 may be evaluated at any point for which equation Equation 3-42 is valid, with a caveat for a base point p on σ. When the base point is not on the boundary, the derivative of the integrals may be taken inside the integral, resulting in

$$\alpha \frac{\partial \phi}{\partial n_p}(p) = \int_\sigma \left(\phi(d) \frac{\partial^2 G}{\partial n_p \, \partial n}(p,d) - \frac{\partial G}{\partial n_p}(p,d) \frac{\partial \phi}{\partial n}(d) \right) \mathrm{d}\sigma. \tag{3-48}$$

On the other hand, when the base point is on σ, the singularities resulting from coincidence of the base point p and the field point d in Equation 3-48 are *too* strongly singular to be integrated directly. As is shown by Ingber and Mitra (1989), the resulting integral may be evaluated in the finite-part sense, or Equation 3-47 may be evaluated by taking the derivative *after* performing the integration. In either case, both the boundary and the normal gradient must be smoothly varying at the point of evaluation in order to perform the requisite operations. This precludes the use of Equation 3-47 at either angle points or jumps in normal gradient values. The more straightforward approach for evaluating Equation 3-47 is to take the derivative of the integral, rather than trying to evaluate the integral in the finite-part sense.

I have played with some of the approaches in the past. My experience suggests that the standard approach is simplest and produces quite acceptable results. Many of the difficulties faced by other practitioners are due to using higher-order interpolation along the boundary. The piecewise linear ϕ and piecewise constant $\partial\phi/\partial n$, together with adequate numbers of elements, is quite sufficient to avoid most difficulties.

7/16/98 Summary of matrix/fracture equations. SAS

Generic Matrix/Fracture Interaction Equations

The generic equations for a fracture interacting with a matrix include resistance across the fracture to matrix flow (e.g., through fracture coatings or air space), lateral flow in the fracture, and sources

in the fracture. The fracture equations are formulated in 2D using the concept of integrated finite volumes. A simple but general formulation for balance within each fracture volume, incorporating diffusive flux within the fracture, sources in the fracture, and exchange with the matrix, is

$$Q_{si} = \sum_j \lambda_e(\phi_j - \phi_i) + Q_{ci}, \tag{3-49}$$

where Q_{si} represents exchange between matrix and fracture at node i, $\lambda_e = b_e K_e / L_e$ is the elemental conductance between nodes i and j, b_e is fracture thickness, K_e is fracture conductivity, L_e is fracture length, ϕ is potential (e.g., temperature), and Q_{ci} is the source arising within the control volume. The formulation is linear unless λ or Q_{ci} are nonlinear. The generality of the formulation is extended when the divergence of net advective flux within the fracture control volume is included into Q_{ci}.

The exchange between matrix and fracture is assumed to occur uniformly along the fracture walls, with the source apportioned so as to create the same gradient in matrix potential along the fracture wall. The fraction of total flux from the source at node i allocated to element e (attached to node i) is

$$F_{ei} = \frac{K_1 + K_2)_e L_e}{\sum_m (K_1 + K_2)_m L_m}, \tag{3-50}$$

where the summation is over the number of elements connected to node i and subscripts 1 and 2 represent sides of the fracture. Assuming that the flux is uniformly distributed along the element, the rate supplied to the fracture walls is

$$q_{se} = \frac{\sum_j F_{ej} Q_{sj}}{L_e \sum_j}, \tag{3-51}$$

where the summation is over the number of nodes attached to the element (2 in 2D). Expanding,

$$q_{se} = \sum_i [\sum_j C_{eik}(\phi_j - \phi_i) + M_{ei} Q_{ci}], \tag{3-52}$$

$$C_{eik} = \lambda_k M_{ei}, \tag{3-53}$$

$$M_{ei} = \frac{F_{ei}}{L_e \sum_i}, \tag{3-54}$$

where the summation in i is over the number of nodes attached to element e, the summation in j is over the number of nodes with connections to node i, and k represents the element between nodes i and j. Note that the form of the equation is also appropriate in 3D (2D fractures) if L_e represents the area of the element when calculating q_{se} and if the width of the connection is included in λ_e.

It is important to note that the value of ϕ in the flux equations represents an average value within the fracture that may differ from the matrix if there is resistance to transfer between the fracture and matrix.

The general boundary integral formulation for flow in the matrix provides values for u or $\partial u/\partial n$ at particular points on the boundary or within the domain of interest. The formulation is quite simple:

$$\sum_i \alpha_i u_i = \int_\sigma \left(G\frac{\partial u}{\partial n} - u\frac{\partial G}{\partial n} \right) \mathrm{d}\sigma + \int_{\sigma_M} \left(G\Delta\frac{\partial u}{\partial n} - \Delta u\frac{\partial G}{\partial n} \right) \mathrm{d}\sigma_M, \tag{3-55}$$

$$= \int_\sigma \left(G\frac{\partial u}{\partial n} - u\frac{\partial G}{\partial n} \right) \mathrm{d}\sigma + \int_{\sigma_M} \left(-Gq_s - \Delta u\frac{\partial G}{\partial n} \right) \mathrm{d}\sigma_M, \tag{3-56}$$

where G is the Green's function, q_s is the flux entering the fracture, σ represents the domain boundary, σ_M represents discontinuities within the domain, and α_i is the fraction of the point in region i (the point may be partially within several domains). If the point is completely within the domain, $\alpha = 1$. On a smooth boundary, $\alpha = 1/2$.

The BIEM requires that all terms within the integrals are known before ϕ can be explicitly evaluated at any point. A well-specified problem does not provide all terms. In order to define the missing terms, a set of linear equations is formed by writing one equation for each unknown. Choosing the representation of piecewise-linear u and piecewise-constant $\partial u/\partial n$, equations along the boundary are written at nodes wherever there is an unspecified value of u and are written at element centroids wherever there is an unspecified value of $\partial u/\partial n$.

In the case where the fracture ϕ is dominated by matrix interaction (e.g., when ϕ is temperature), the fracture value for ϕ is the numerical average of the matrix ϕ surrounding the point. In this case, u might represent $K\phi$, where K represents conductivity (piecewise constant by region). Flux is represented by $q = -K\nabla\phi = -\nabla u$. Through-flux from matrix to matrix across the fracture may be limited by increased resistance within the fracture, and the matrix blocks may have different conductivities.

In this situation, the general form of the equation written at the discontinuity nodes in the middle of the fracture (not at a fracture intersection) is

$$\alpha_1 u_1 + \alpha_2 u_2 = \int_\sigma \left(G\frac{\partial u}{\partial n} - u\frac{\partial G}{\partial n} \right) \mathrm{d}\sigma + \int_{\sigma_M} \left(-Gq_s - \Delta u\frac{\partial G}{\partial n} \right) \mathrm{d}\sigma_M, \tag{3-57}$$

where the subscripts 1 and 2 represent matrix sides 1 and 2 of the fracture and q_s is defined by fracture mass balance considerations. The unspecified values of q_s require ϕ within the fracture, while Δu is also unspecified. Choosing ϕ within the fracture (piecewise linear between nodes) and Δu (piecewise constant for elements) as variables to be determined, the left-hand-side can be

rewritten

$$\alpha_1 u_1 + \alpha_2 u_2 = (\alpha_1 + \alpha_2)\left(\frac{2K_1K_2}{K_1+K_2}\right)\phi + \left[(\alpha_1+\alpha_2)\left(\frac{K_2-K_1}{K_1+K_2}\right) + (\alpha_2-\alpha_1)\right]\frac{\Delta u}{2}. \tag{3-58}$$

As Δu is only piecewise constant, the arithmetic average of the values attached to the node is used. Note that the following relationships are used:

$$u = K\phi \tag{3-59}$$

$$u_1 = \bar{u} - \Delta u/2 \tag{3-60}$$

$$u_2 = \bar{u} + \Delta u/2 \tag{3-61}$$

$$\bar{\phi} = \frac{1}{2}(\phi_1 + \phi_2) \tag{3-62}$$

$$\bar{\phi} = \frac{1}{2K_1K_2}\left[(K_1+K_2)\bar{u} + (K_1-K_2)\Delta u/2\right] \tag{3-63}$$

$$\Delta\phi = 2\left(\frac{K_1-K_2}{K_1+K_2}\right)\bar{\phi} + \frac{2}{K_1+K_2}\Delta u \tag{3-64}$$

In this general case, both ϕ and Δu must be determined, but insufficient equations are generated if only nodes are used. An additional set of equations is derived by taking the derivative with respect to the normal direction of the discontinuity, yielding

$$\frac{\partial}{\partial n}(\alpha_1 u_1 + \alpha_2 u_2) = \frac{\partial}{\partial n}\left[\int_\sigma \left(G\frac{\partial u}{\partial n} - u\frac{\partial G}{\partial n}\right) d\sigma + \int_{\sigma_M}\left(-Gq_s - \Delta u\frac{\partial G}{\partial n}\right) d\sigma_M,\right]. \tag{3-65}$$

This derivative equation can only be used where the discontinuity is smooth, due to integration difficulties for the high-order singularities arising when the integration passes through the base point. Because of this limitation, Δu is defined as piecewise constant so that enough equations can be generated to determine the unknown values.

The derivative equation is used to impose the restriction on flux normal to the fracture. The left-hand-side is rearranged in terms of ϕ and Δu to yield

$$\frac{\partial}{\partial n}(\alpha_1 u_1 + \alpha_2 u_2) = (\alpha_1+\alpha_2)\frac{K_r}{b}\Delta\phi - \left(\frac{\alpha_1K_1 + \alpha_2K_2}{K_1+K_2}\right)q_s \tag{3-66}$$

$$= \frac{1}{K_1+K_2}\left[2(\alpha_1+\alpha_2)\frac{K_r}{b}((K_1-K_2)\phi + \Delta u) - (\alpha_1K_1+\alpha_2K_2)q_s\right] \tag{3-67}$$

$$= \frac{1}{K_1+K_2}\left[2\frac{K_r}{b}((K_1-K_2)\phi + \Delta u) - \frac{1}{2}(K_1+K_2)q_s\right], \tag{3-68}$$

where $\alpha_1 = \alpha_2 = \frac{1}{2}$ by virtue of the smoothness of the boundary.

Several simplifications may occur. When $K_r = 0$, the matrix is forced to interact completely with the fracture (no flow bypasses the fracture). When the matrix has the same $K = K_m$ on each side of the fracture, the left-hand-side terms become

$$\alpha_1 u_1 + \alpha_2 u_2 = (\alpha_1 + \alpha_2) K_m \phi + (\alpha_2 - \alpha_1) \frac{\Delta u}{2}, \tag{3-69}$$

$$\frac{\partial}{\partial n}(\alpha_1 u_1 + \alpha_2 u_2) = \frac{K_r}{b K_m} \Delta u - \frac{1}{2} q_s. \tag{3-70}$$

If, instead, the drop in ϕ across the fracture is negligible, then the derivative equation is not needed and $\alpha_1 u_1 + \alpha_2 u_2 = (\alpha_1 K_1 + \alpha_2 K_2)\phi$. If the matrix conductivity is also identical on either side of the fracture, the left-hand-side term further simplifies to $\alpha_1 u_1 + \alpha_2 u_2 = (\alpha_1 + \alpha_2) K_m \phi$.

Complications can occur in the left-hand-side of the nodal equation at junctions between fracture sets or at the end of the fracture, due to ambiguities in specifying Δu at the node. If the fracture ends in a uniform matrix ($K_1 = K_2 = K_m$), then $\alpha_1 = \alpha_2 = 1/4$ and the Δu portion of the term is zero. If the fracture lies along a material discontinuity, discretization continues along the discontinuity with no ambiguity. If the fracture node represents a junction between fracture sets, the left-hand-side term becomes

$$\sum_i \alpha_i u_i = \sum_i \alpha_i K_i [\bar{\phi} + \frac{\sum_k (\phi_i - \phi_k)}{\sum_k}] \tag{3-71}$$

$$\phi_i - \phi_k = 2 \left(\frac{K_k - K_i}{K_i + K_k} \right) \bar{\phi} + \frac{2}{K_i + K_k} (u_i - u_k) \tag{3-72}$$

where the summation over i represents the number of matrix blocks contacting node i and the summation over k represents the number of fracture elements contacting matrix block i. The junction equation is valid in both 2D and 3D, and reduces to the simpler formulation. Note that the junction equation is valid for any case where material discontinuities meet, as long as $\bar{\phi}$ is the value that is solved for at the junction.

7/17/98 Simpler formulation of matrix/fracture equations. SAS

Localized Matrix/Fracture Interaction Equations

A slightly different generic case arises if there is local resistance to transferral from the fracture to the matrix (e.g., fluid flow in the fracture resists transferral due to a fracture coating). The local-resistance case is more straightforward to code than the generic case considered previously, due to the more straightforward representation for fracture mass balance.

The nodal balance equation is the fracture mass balance. For fracture node i,

$$\sum_j \lambda_{ij}(\phi_j - \phi_i) + \sum_k L_k[C_{k1}(\phi_k - \phi_{k1}) + C_{k2}(\phi_k - \phi_{k2})] + Q_{ci} = 0, \tag{3-73}$$

where the summation over j represents the number of nodal connections exchanging with node i and the summation over k represents the number of elements attached to node i. The potential in the fracture is denoted by ϕ, while the potential in the matrix is denoted by ϕ_1 and ϕ_2 (for sides 1 and 2 of the fracture, respectively).

For element centroids in this case, assume

$$q_{se} = C_{e1}(\phi_e - \phi_{e1}) + C_{e2}(\phi_e - \phi_{e2}). \tag{3-74}$$

The left-hand-side of the derivative equation is

$$\alpha \frac{\partial}{\partial n}(u_1 + u_2) = 2\alpha \left(\frac{K_f}{b}(\phi_2 - \phi_1) - q_s \right) = \frac{K_f}{b}(\phi_2 - \phi_1) - q_s \tag{3-75}$$

where

$$q_s = 2\bar{C}\phi_e - (2\bar{C}\bar{\phi} + \frac{\Delta C \Delta \phi}{2}), \tag{3-76}$$

$$\bar{\phi} = \frac{1}{2K_1K_2}\left[(K_1 + K_2)\bar{u} + (K_1 - K_2)\frac{\Delta u}{2}\right], \tag{3-77}$$

$$\Delta\phi = \frac{1}{K_1K_2}\left[(K_1 - K_2)\bar{u} + (K_1 + K_2)\frac{\Delta u}{2}\right], \tag{3-78}$$

$$\bar{C} = \tfrac{1}{2}(C_1 + C_2), \tag{3-79}$$

$$\Delta C = C_2 - C_1. \tag{3-80}$$

There are two equations with two unknowns (Δu and q_s), where the second equation is a mass-balance statment for q_s. Note that $\bar{u}$ is directly obtained from an evaluation of the normal-equation integral and ϕ_e is the average of the surrounding nodal values for fracture potential. As C_1 and C_2 become large, potentials become nearly identical across the fracture. One can consider an arbitrarily thin layer of the matrix to be the resistant layer if no fracture coating exists.

Assigning conductances (conductivity divided by thickness) is consistently performed by considering the case where three distinct (and isotropic) layers form the fracture. In sequence, the layers might represent a fracture coating (1), fluid (2), and another fracture coating (3). The total conductance for flow normal to the fracture is then

$$C_{norm} = \frac{\theta}{\sum_i^3 b_i/K_i} + \frac{(1-\theta)K_{bypass}}{\sum_i^3 b_i}, \tag{3-81}$$

while the total conductance for flow along the fracture is

$$C_{tang} = \frac{\sum_i^3 b_i K_i}{L \sum_i^3 b_i}. \tag{3-82}$$

The fraction of the surface area of the fracture contributing to fracture/matrix exchange is denoted by θ; the remainder is assumed to contribute to fracture-bypass fluxes (e.g., through matrix-to-matrix contact along asperities) with conductivity K_{bypass}. The consistent representation for conductances becomes

$$C_{e1} = \frac{\theta}{b_1/K_1 + b_2/(2K_2)}, \tag{3-83}$$

$$C_{e2} = \frac{\theta}{b_3/K_3 + b_2/(2K_2)}, \tag{3-84}$$

$$\bar{C} = \frac{1}{2}(C_{e1} + C_{e2}), \tag{3-85}$$

$$\Delta C = C_{e2} - C_{e1}, \tag{3-86}$$

$$\frac{K_f}{b} = C_{norm}, \tag{3-87}$$

$$\lambda_e = C_{tang}. \tag{3-88}$$

These representations are consistent even if the fracture coatings do not exist ($b_1 = 0$ and/or $b_3 = 0$).

Rearranging the derivative-equation left-hand-side for an element centroid,

$$\alpha \frac{\partial}{\partial n}(u_1 + u_2) = C_{norm}\left(\frac{K_1 - K_2}{K_1 K_2}\right)\bar{u} + C_{norm}\left(\frac{K_1 + K_2}{K_1 K_2}\right)\frac{\Delta u}{2} - q_s, \tag{3-89}$$

while the statement for q_s (also at the centroid) is

$$q_s = 2\bar{C}\phi_e - \left[\bar{C}\left(\frac{K_1 + K_2}{K_1 K_2}\right) + \frac{\Delta C}{2}\left(\frac{K_1 - K_2}{K_1 K_2}\right)\right]\bar{u} - \left[\frac{\bar{C}}{2}\left(\frac{K_1 - K_2}{K_1 K_2}\right) + \frac{\Delta C}{4}\left(\frac{K_1 + K_2}{K_1 K_2}\right)\right]\Delta u. \tag{3-90}$$

In these expressions, $\bar{u}$ is determined by an integral, Δu is the unknown to be determined at the centroid, and ϕ_e is the average of the fracture potentials for the nodes determining the element. The C values should be derived from the K and b values as noted above.

7/20/98 Matrix formulation of matrix/fracture equations.

Simplifications occur when the fracture does not interact with the matrix or lateral flow in the fracture can be neglected, so that $q_s = 0$ and only one equation need be solved at the centroid:

$$\alpha \frac{\partial}{\partial n}(u_1 + u_2) = C_{norm}\left(\frac{K_1 - K_2}{K_1 K_2}\right)\bar{u} + C_{norm}\left(\frac{K_1 + K_2}{K_1 K_2}\right)\frac{\Delta u}{2}. \tag{3-91}$$

If the matrix also has the same conductivity on each side of the fracture, the left-hand-side reduces to

$$\alpha \frac{\partial}{\partial n}(u_1 + u_2) = \left(\frac{C_{norm}}{K_m}\right) \Delta u. \tag{3-92}$$

If the matrix and fracture interact but the matrix has the same conductivity on each side of the fracture, the two equations are

$$\alpha \frac{\partial}{\partial n}(u_1 + u_2) = \left(\frac{C_{norm}}{K_m}\right) \Delta u - q_s, \tag{3-93}$$

$$q_s = 2\bar{C}\phi_e - \frac{2\bar{C}}{K_m}\bar{u} - \frac{\Delta C}{2K_m}\Delta u. \tag{3-94}$$

If the fracture has no particular resistance to flow normal to the fracture (e.g., it is simply a material discontinuity), the formulation does not require the use of the derivative equation, but can use the standard equation with a left-hand-side in the form:

$$\alpha \left(\frac{K_1 + K_2}{K_2 - K_1}\right) \Delta u \tag{3-95}$$

(note that the continuity of potential requires that $\bar{u} = (K_1 + K_2)\phi$ and $\Delta\phi = (K_2 - K_1)\phi$).

Combining all of these cases into a generic format, a BIEM equation for any material-derived discontinuity can be written at the element centroids in terms of (i) values for ϕ at the surrounding nodes, (ii) jumps in u at the centroid, (iii) integrals of the normal equation, and (iv) integrals of the derivative equation. In the most complex cases, both Equation 3-96 and Equation 3-97 are required; otherwise only one is. The full equations are

$$a_{11}q_s + a_{12}\Delta u = b_{11}\left[\int_\sigma \left(G\frac{\partial u}{\partial n} - u\frac{\partial G}{\partial n}\right) d\sigma + \int_{\sigma_M} \left(-Gq_s - \Delta u\frac{\partial G}{\partial n}\right) d\sigma_M\right]$$

$$+b_{12}\frac{\partial}{\partial n}\left[\int_\sigma \left(G\frac{\partial u}{\partial n} - u\frac{\partial G}{\partial n}\right) d\sigma + \int_{\sigma_M} \left(-Gq_s - \Delta u\frac{\partial G}{\partial n}\right) d\sigma_M\right], \tag{3-96}$$

$$a_{21}q_s + a_{22}\Delta u + a_{23}\phi_e = b_{21}\left[\int_\sigma \left(G\frac{\partial u}{\partial n} - u\frac{\partial G}{\partial n}\right) d\sigma + \int_{\sigma_M} \left(-Gq_s - \Delta u\frac{\partial G}{\partial n}\right) d\sigma_M\right], \tag{3-97}$$

where

$$a_{11} = -1 \tag{3-98}$$

$$a_{12} = \frac{C_{norm}}{2}\left(\frac{K_1 + K_2}{K_1 K_2}\right) \tag{3-99}$$

$$b_{11} = -C_{norm}\left(\frac{K_1 - K_2}{K_1 K_2}\right) \tag{3-100}$$

$$b_{12} = 1 \tag{3-101}$$

$$a_{21} = -1 \tag{3-102}$$

$$a_{22} = -\frac{\bar{C}}{2}\left(\frac{K_1 - K_2}{K_1 K_2}\right) - \frac{\Delta C}{4}\left(\frac{K_1 + K_2}{K_1 K_2}\right) \tag{3-103}$$

$$a_{23} = 2\bar{C} \tag{3-104}$$

$$b_{21} = \bar{C}\left(\frac{K_1 + K_2}{K_1 K_2}\right) + \frac{\Delta C}{2}\left(\frac{K_1 - K_2}{K_1 K_2}\right). \tag{3-105}$$

Equation 3-96 can be referred to as the Δh equation while Equation 3-97 can be referred to as the Δg equation.

The fracture mass balance equation for fracture node i is

$$\sum_j C_{tangij}(\phi_j - \phi_i) + \sum_k A_{nfk} q_{sk} + Q_{ci} = 0, \tag{3-106}$$

where A_{nfk} is the area of the fracture exchanging with the matrix that is associated with the node ($A_{nfk} = L_k/2$ in 2D), the summation over j represents the number of nodal connections exchanging with node i and the summation over k represents the number of elements attached to node i.

7/27/98 Partial results of testing. SAS

I used the Jacquard program, which I had developed while at the University of Vermont, to incorporate the ideas on boundary element simulation of fracture/matrix interaction. The Jacquard program incorporates a BIEM module based on the code I developed in my dissertation work. The module intent was to enable interpolation based on the Laplace equation. I had worked out approaches for some of the possible discontinuity formulations at that time, and included them in the code to help document my thinking, but only tested the coding for normal-equation boundaries and line-potential discontinuities. Resistance and material-change discontinuities were incorporated but not verified.

The fracture formulations developed above can be simplified to represent other discontinuities, thereby allowing components of the fracture formulation to be tested independently. As of

today, the Jacquard module includes the following discontinuities:

- Specified-head boundaries
  - Normal-equation for unknown $\partial\phi/\partial n$
  - Derivative-equation for unknown $\partial\phi/\partial n$
- Specified-gradient boundaries
- Line discontinuities
  - Change in matrix properties
  - Specified-potential
  - Specified-source
  - Specified-flux
  - Specified-potential-jump
  - Thin inclusion (no lateral flow in inclusion) with or without change in matrix properties
  - Thin inclusion (lateral flow in inclusion) with or without change in matrix properties

I have tested almost all of these cases, checking for plausibility but without verifying numerical accuracy in most cases. The only case not checked at least summarily is the inclusion with lateral flow and a change in matrix properties.

The test cases are loosely based on the YM repository. The ultimate problem of interest is a vertical fracture with liquid and vapor flux, with the fracture penetrating a drift. The test domain extends roughly 1000 m horizontally both sides of the drift, and roughly 100 m vertically both sides of the drift. Testing of a particular discontinuity may use either horizontal or vertical discontinuity orientations. In general, potentials are specified at the top and bottom of the domain, with the sides open (semi-infinite). Near the drift, these side boundary conditions have little effect.

The plausibility tests were valuable in identifying several minor coding problems, both in the original code and in the additions. The formulations appear to work fairly well at worse and very well at best.

A particularly weak formulation is for a thin inclusion without lateral flow when the conductance of the inclusion is small. This case is like a low-conductivity lens. Apparently the matrix becomes poorly conditioned when the conductivity drops below a few orders of magnitude less than

the matrix. The singularity term, which goes on the diagonal, is proportional to the conductance. As the singularity term goes to zero, conditioning becomes very poor. Physically the problem appears when the conductance is small enough to significantly reduce flow. The difficulty is more apparent when potential is not centered on zero (i.e., extra digits required to represent the potential reduce the number of significant digits used in computations). I don't consider the thin-barrier formulation particularly reliable.

Two comparisons were made for direct confirmation of results. An analytic solution is available when the problem is 1D. I tested the boundary contours for a box, no-flow on two opposing sides and specified-potential on the other two sides. This test identified a problem with the derivative-equation integrations (required for the fracture formulation). The problem was remedied, and analytic solutions were obtained both for the normal-equation approach and the derivative-equation approach, even when the grid was rotated ninety degrees.

The second comparison used the PDE tools supplied with *Matlab* to check the solution for a box with a fracture. The box is 20 m horizontally and 100 m vertically, with a fracture on one vertical side. The fracture was assigned the same material property as the matrix. A uniform sink was applied within the fracture, comparable to the energy removed by latent heat for flows representative of YM. The solutions from *Matlab* and the BIEM approach are identical at the boundaries, to the resolution visible from contour plots. This problem will be revisited with Goodluck for more stringent testing.

Before testing with *Matlab*, I modified the fracture formulation to have fracture potentials supplied at the element centroids rather than the nodes. The solutions generated with the unknown potentials at nodes suffered from numerical instability, with alternate potentials above and below the "true" solution. Instability become noticable for sources orders of magnitude smaller than would be expected for YM problems. The reformulation completely eliminated the instability.

I used the *Matlab* PDE tools to play with the effect of conductivity in the fracture. When the fracture conductivity is comparable to the matrix conductivity, the solution appears to be prone to the same type of instability that was observed in the BIEM approach. When the fracture conductivity is large or small enough, the solution behaves well. One would expect that other codes would have similar difficulties.

7/30/98 Updated Observations. SAS

Goodluck and I tested the BEM code against Abaqus yesterday. Essentially the same problem was used as when I tested the code against *Matlab*, with a slightly different thermal conductivity and a larger extraction rate. We compared vertical transects along the fracture, the far boundary, and the middle of the domain. We also compared horizontal transects at -25, 0, and 25 m (the quarter- and midpoints). These comparisons are plotted in Goodluck's notebook. The results are about as good as was achieved in the comparison against *Matlab*.

The Abaqus fracture was applied as a simple extraction flux along the portion of the boundary corresponding to the fracture. This procedure reduces or eliminates the problems associated with extreme differences in discretization and material properties. After the successful testing, Goodluck and I devised a simple procedure for estimating the penetration zone using this observation of numerical simplicity. If we assume that the total energy extracted from the rock due to boiling is known for a given liquid flux (i.e., latent heat), and we further assume that the energy is extracted in a range of temperatures above and below the boiling point (e.g., ± 5 °C), the problem reduces to predicting the location of the top and bottom of the sink zone. The location of the sink zone should be found fairly straightforwardly through iteration.

The simplified procedure misses three aspects of the problem, however. The implicit assumption is that all liquid flux is converted to vapor flux continuing down the fracture so that there is no recirculation above the boiling zone. The latent heat released upon condensation, thereby warming the condensation zone, is not accounted for. Also, the water entering the system must be warmed from the original temperature to the boiling temperature (above the top boiling zone) and must be cooled to the bottom temperature (below the bottom boiling zone), providing additional energy sinks. One would expect that these effects would be important in different domains. In particular, the release of heat from condensation would be most important near the boiling zone, while the heating/cooling of water would act all the way along the fracture outside the condensation zone.

In order to form a heat pipe, there must be excess capacity for moisture movement beyond that required to transfer the incoming water to the bottom of the domain. It should be possible to estimate the excess capacity, which in turn provides an estimate for the maximum magnitude of recirculation and the maximum amount of energy bound up in the recirculation cycle. The excess capacity is overestimated by the difference between the maximum gravity flux and the actual flux in the fracture (vapor flux needs some capacity unless it occurs in the matrix).

It is reasonable to assume that the excess flux will not always be mobilized. Rather, the

excess flux will not exceed that which creates a monotonic temperature distribution.

A slight modification to the problem may serve to capture the full behavior a bit better. The boiling/condensation behavior is more like a source dipole than a sink, with unbalanced components (some of the latent heat is removed through downward vapor flux, which balances the flux entering the top of the fracture). Perhaps the source and the sink can each be modeled as triangularly distributed over a certain temperature range, where the ranges overlap. An additional source/sink term can be applied uniformly along the fracture from the boundary to the boiling temperature, with a total strength that required to raise the liquid from the initial temperature to boiling. The net source/sink term at any particular location is simply the sum of the three. Note that when the fracture extends above and below the drift, the latent heat lost from above the drift is deposited below the drift, and heat is lost from the liquid as it cools to the bottom boundary temperature. Both of these effects would tend to bring the top reflux zone closer to the drift than the bottom zone would be.

As a practical matter, I would expect that the boiling pattern might drop off rapidly below boiling and not so rapidly above boiling, peaking slightly above boiling. Similarly, I would expect that the condensation pattern would drop off rapidly above boiling and not so rapidly below boiling, peaking slightly below boiling.

A heat-pipe effect would develop from these assumptions. It has to be seen whether the heat pipe bears any resemblance to the heat pipe that develops when fluid motion is explicitly considered. The approach implicitly assumes that the fluid moves readily relative to the flux of energy in the rock. In addition, the approach implicitly assumes that the flux in the fracture is essentially at the carrying capacity for the fracture (so that no excess recirculation can take place).

References

Ingber, M. S. and A. K. Mitra. 1989. The evaluation of the normal derivative along the boundary in the direct boundary element method. *Applied Mathematical Modelling 13*, 32–40.

Liggett, J. A. and P. L.-F. Liu. 1983. *The Boundary Integral Equation Method for Porous Media Flow*. London, England: George Allen & Unwin.

Pullan, A. J. and I. F. Collins. 1987. Two- and Three-Dimensional Steady Quasi-Linear Infiltration From Buried and Surface Cavities Using Boundary Element Techniques. *Water Resources Research 23*(8), 1633–1644.

Stothoff, S. A. 1991. *A Boundary Integral Technique for Modelling Two-Phase Flow in Porous Media*. Ph. D. thesis, Princeton University, Princeton, NJ.

4. Iterative Performance KTI

Account Number: **20-1402-761**
Collaborators: **Robert Baca, Gordon Wittmeyer**
Directories: **As noted**

August 4, 1998 Printout entry.

I performed no work on this project during the period covered by this printout.

5. Iterative Performance KTI - Total Performance Assessment Phase 3

Account Number: **20-1402-761**
Collaborators: **Robert Baca, Gordon Wittmeyer, Sitakanta Mohanty**
Directories: **$HOME2/Matlab/TPA3, $HOME2/IPA/Phase3, as noted**

August 4, 1998 Printout entry.

I performed no work on this project during the period covered by this printout.

6. Breath code development

Account Number: **20-1402-863**
Collaborators: **As noted**
Directories: **Subdirectories of $HOME2/Numeric/Breath as noted**

August 4, 1998 Printout entry.

I performed no work on this project during the period covered by this printout.

11 of 20

SCIENTIFIC NOTEBOOK

by

Stuart A. Stothoff

SCIENTIFIC NOTEBOOK

by

Stuart A. Stothoff

Southwest Research Institute
Center for Nuclear Waste Regulatory Analyses
San Antonio, Texas

January 30, 1999

Initial Entries

Scientific NoteBook: # 163

Issued to: S. A. Stothoff

Issue Date: Tuesday, November 16, 1993

By agreement with the CNWRA QA this NoteBook is to be printed at approximate quarterly intervals. This computerized Scientific NoteBook is intended to address the criteria of CNWRA QAP–001.

Table 0-1: Computing Equipment

Machine Name	Type	OS	Location
sierra.cnwra.swri.edu	Sun SPARC 20	SUNOS 4.1.3_U1	desk Rm A-212, Bldg. 189
sisyphus.cnwra.swri.edu	Sun SPARC 20	SUNOS 4.1.3_U1	network
dopey.cnwra.swri.edu	Sun SPARC 10	SUNOS 4.1.3_U1	network
performer.cnwra.swri.edu	SGI Onyx	IRIX 5.3	network
yosemite.cnwra.swri.edu	SGI Onyx	IRIX 5.3	network
bemore.cnwra.swri.edu	SGI Onyx	IRIX 6.2	network
redwood.cnwra.swri.edu	SGI Indy	IRIX 6.2	network
bigbend.cnwra.swri.edu	Sun Ultra-2	SUNOS 5.5.1	network
scratchy1.cnwra.swri.edu	Sun Ultra-2	SUNOS 5.5.1	network
hornet.cnwra.swri.edu	Sun Ultra-2	SUNOS 5.5.1	network

Contents

List of Figures

List of Tables

Quarterly Information

Entries into Scientific NoteBook # 163 for the period November 16, 1995, to January 30, 1999, have been made by Stuart Stothoff (SAS; January 30, 1999).

No original text entered into this Scientific Notebook has been removed (SAS; January 30, 1999).

cooling relieves some of the strain that forms cooling joints. Lithophysal units tend to spall, forming plate-like talus, while the nonlithophysal units tend to form bulkier talus. The lithophysal talus appears to be somewhat less resistant to further breakdown than the nonlithophysal units. Accordingly, locations with nonlithophysal units cropping out provide a heuristic indicator for both gaping fractures and talus, which are both strong indicators for high infiltration.

S. Stothoff examined eight of the sixteen upper-wash channels between Highway Ridge and Antler Ridge, all of which feature Tcpmn outcrops, to see if they also have other features indicative of high infiltration. Two of the washes, the Split Wash fork already mentioned and the north branch of WT-2 Wash (just south of Whaleback Ridge), appear to have notable high-infiltration areas while the remaining washes appear to be more typical. The WT-2 Wash area shares with Split Wash the characteristics of no recent runoff, copious talus, gaping fractures, dense vegetation, and minimal fracture fillings (at least near the bedrock surface). The nonlithophysal-unit outcrop areas in all of these washes appear to be generally more conducive to infiltration than the lithophysal areas, but the potential for infiltration is mitigated in many of the washes by limited outcrop area, shallow channel slopes, or shallow sideslopes.

In general, talus was more common on north-facing slopes and exposed bedrock fractures were more common on south-facing slopes. Densely welded nonlithophysal units in the examined washes rarely had exposed bedrock in the actual channel, while the lithophysal units often exposed channel bedrock for significant portions of the upper wash.

With the notion that deeper soils are indicators of reduced MAI, due to increased storage and opportunity for evapotranspiration, clues regarding soil depth during glacial periods were also sought during the infiltration hotspot survey. Many of the washes featured concave-down slopes to the channel, which indicates that the most recent activity has been degradational. Colluvial lobes are apparent along many of the washes, suggestive that deeper soils may have existed in the past. If these washes become aggradational in the future, it would be expected that the deeper covers would reduce MAI and thereby reduce the hotspot activity.

11/9/98 Summary of activities. SAS

I have been quite active in working on infiltration issues for the last several months. Two documents have been essentially completed during this period. One is work related to the one-dimensional (1D) bare-soil infiltration simulations, abstracting the simulation results into three formulae for *MAI* (depending on the hydraulic properties of the system). The abstractions were exercised on

heterogeneity issues. The second document was compiled by D. Groeneveld, and discusses the ecologic and hydrologic implications of weedy brome grasses invading the YM area. Both of these documents will be inserted into the notebook, with annotations, upon completion.

I am currently putting together an updated map of *MAI*, using the new abstractions with site-specific data. An ARC-INFO file of the detailed bedrock geology of the central block (Day et al., 1998), obtained from the Department of Energy (DOE) (with original copy maintained by R. Martin), is used to provide a base for the estimate. The geology polygons are transferred to a grid as needed. Bedrock and soil hydraulic properties can be obtained from Flint et al. (1996a), as are fracture intensities. Typical fracture apertures and typical fillings for the units were estimated from my personal fieldwork, as no guidance is provided by Flint et al. (1996a).

Soil properties are from Flint et al. (1996a) as well, with Typic Haplocambids, Typic Calciargids, and Lithic Haplocambids assigned to areas mapped as alluvium, colluvium, and everywhere else, respectively. These assignments are based on the soils in the vicinity of the repository footprint in the soil map presented by Flint et al. (1996a). Of the eight classified soils, the largest K_{sat} is 3.8×10^{-5} m/s and the smallest is 5.6×10^{-6} m/s. These values are all large enough to produce maximal values of *MAI*, so that capturing the exact soil classification is likely not important.

The 1D simulations only use one type of layer beneath the soil, which can be unfilled fractures, soil- or carbonate-filled fractures, or bedrock. The abstractions handle each case. However, the actual field situation likely has some of each case for any one area, each affecting the local pressure gradients. The pressure field most representative of field conditions is assumed to be the one yielding the greatest fluxes, so that the maximum of the four cases is used.

The resulting predictions of *MAI* in the central block are significantly larger than any field observations suggest, particularly in deep alluvium. This is largely due to the neglect of vegetation in the 1D simulations. An uptake efficiency factor may be defined to account for the additional water that vegetation can extract beyond bare-soil evaporation. It is assumed that no additional extraction occurs with zero soil thickness and, if the soil is sufficiently thick to allow a full rooting zone, only a small percentage of the bare-soil *MAI* (e.g., 1 percent) escapes the rooting zone. For intermediate soil thicknesses, the impact of transpiration on *MAI* is assumed to increase exponentially with increasing soil thickness, with the form

$$MAI = MAI_{bs} \exp(-\eta b), \tag{1-16}$$

where MAI_{bs} is the bare-soil *MAI* [L/T], η is the extinction coefficient [1/L], and b is the minimum between soil thickness and maximum rooting depth [L]. Shrubs under current climatic conditions would typically have a rooting zone of about a meter, according to David Groeneveld. Under

wetter climates and larger vegetation, the rooting zone may be deeper but the extinction coefficient smaller. Takeover of bromus would provide a shallower rooting depth (roughly 30 cm), but the extinction coefficient might not change. Both David Groeneveld and Dani Or concur that the correction procedure is reasonable and plausible.

The uptake efficiency factor should be qualitatively correct. Plants tend to have exponentially decreasing biomass with depth (except in the top of the soil column), suggesting that uptake may fall off exponentially with depth. There is some error associated with not accounting for roots in the fractures below the soil zone, which we have observed in the field. The exact values used for the lower rooting-zone thickness and the percentage of *MAI* allowed through the plant uptake are most important in deep soils, not in the shallow soils over the repository (except in the caprock region). Quantifying the reduction factor more precisely will require implementing transpiration into *breath* and performing a series of simulations.

11/10/98 Activities related to infiltration maps. SAS

Putting together the *MAI* map has brought forth several observations. The most important observation is in regard to neglecting transpiration, with proposed treatment discussed above. Additional observations are discussed below.

Under current soil textures, the fracture classifications providing the most infiltration are, in order from largest to smallest, soil-filled, carbonate-filled, and unfilled. Even a small percentage of the fractures with soil filling yields greater values of *MAI* than a much greater percentage filled with relatively high-permeability carbonate, and with only a few centimeters of cover fillings yield larger *MAI* than provided by unfilled fractures. Note that the soil-filled fracture simulations are insensitive to fracture pore space even down to 10^{-4}, and unfilled fractures are minimally sensitive until fracture pore space gets below 10^{-3}. I suspect that adjacent soil-filled and carbonate-filled fractures in the field may be dominated by the capillarity in the carbonate fillings, so that carbonate-dominated areas may see little influence from a few soil-filled fractures. The capillarity in fracture fillings may be somewhat independent of unfilled fractures, as unfilled fractures are only active under infrequent, short, extremely wet conditions.

In order to accommodate these observations in the *MAI* map, soil-filled fractures are assumed not to exist except in caprock-like units and nonlithophysal units. Carbonates are assumed to dominate welded units and are present at low values in the non- to moderately welded units, except for caprock (with large soil-filled fractures). Unfilled fractures are assumed not present

in caprock, minimally present in welded units, and dominant in less-welded units. Note that in less-welded units, *MAI* for bedrock may be larger than *MAI* for fractures. Also note that, thankfully, the lack of sensitivity to fracture pore space makes precise allocation of fracture pore space unimportant (except for the presence/absence of soil-filled fractures).

The bedrock is not known under regions mapped as alluvium or colluvium. Such areas are arbitrarily assigned bedrock properties (including fracture properties) of the lithophysal units, as such units are typically below colluvium. Note that it makes no difference what is assigned with deep soils.

The nominal map of *MAI*, using best estimates for bedrock and fracture properties, is somewhat different from maps I've produced earlier and from maps produced by United States Geological Survey (USGS). Without the vegetation adjustment, the trends in the map are similar to other efforts for shallow soils, with highest rates on the caprock. However, *MAI* is quite large in deep soils (as much as 80 mm/yr). With the vegetation adjustment, the deep-soil *MAI* drops to small values as before. There is a significant drop in *MAI* in the caprock with vegetation, while there is little change on sideslopes or ridges, so that the ridges are predicted to provide relatively large *MAI*. There is also a prominant pair of high-*MAI* stripes on the west flank of YM, due to nonlithophysal-unit outcrops, and additional nonlithophysal hotspot areas increasing to the south of the footprint.

Each pixel can be classified according to what feature provides the largest *MAI* (i.e., deep soil, bedrock, unfilled fracture, carbonate-filled fracture, or soil-filled fracture). Very few areas have unfilled-fracture dominance. Bedrock dominance is generally along channels or on the west flank of YM. Soil-filled fractures dominate in almost all areas where they exist (caprock, nonlithophysal units), while carbonate-filled fractures dominate in the welded units.

The nominal map is based on a refined elevation Digital Elevation Model (DEM), obtained by using a cubic interpolant (interp2 in *Matlab*) on the original grid with cells 30 m on a side. A reduced area is considered, 2 km by 5 km, centered on the main repository block. Each cell is refined into 16 cells, 7.5 m on a side. The soil thickness is calculated directly on the refined grid, with a much smoother representation. The ephemeral channels are far better captured, although grid cells on the order of 0.5 m on a side would be required to fully resolve the channels (perhaps for Split Wash).

I used the *Matlab* PDE tools to play with the effect of conductivity in the fracture. When the fracture conductivity is comparable to the matrix conductivity, the solution appears to be prone to the same type of instability that was observed in the BIEM approach. When the fracture conductivity is large or small enough, the solution behaves well. One would expect that other codes would have similar difficulties.

7/30/98 Updated Observations. SAS

Goodluck and I tested the BEM code against Abaqus yesterday. Essentially the same problem was used as when I tested the code against *Matlab*, with a slightly different thermal conductivity and a larger extraction rate. We compared vertical transects along the fracture, the far boundary, and the middle of the domain. We also compared horizontal transects at -25, 0, and 25 m (the quarter- and midpoints). These comparisons are plotted in Goodluck's notebook. The results are about as good as was achieved in the comparison against *Matlab*.

The Abaqus fracture was applied as a simple extraction flux along the portion of the boundary corresponding to the fracture. This procedure reduces or eliminates the problems associated with extreme differences in discretization and material properties. After the successful testing, Goodluck and I devised a simple procedure for estimating the penetration zone using this observation of numerical simplicity. If we assume that the total energy extracted from the rock due to boiling is known for a given liquid flux (i.e., latent heat), and we further assume that the energy is extracted in a range of temperatures above and below the boiling point (e.g., ± 5 °C), the problem reduces to predicting the location of the top and bottom of the sink zone. The location of the sink zone should be found fairly straightforwardly through iteration.

The simplified procedure misses three aspects of the problem, however. The implicit assumption is that all liquid flux is converted to vapor flux continuing down the fracture so that there is no recirculation above the boiling zone. The latent heat released upon condensation, thereby warming the condensation zone, is not accounted for. Also, the water entering the system must be warmed from the original temperature to the boiling temperature (above the top boiling zone) and must be cooled to the bottom temperature (below the bottom boiling zone), providing additional energy sinks. One would expect that these effects would be important in different domains. In particular, the release of heat from condensation would be most important near the boiling zone, while the heating/cooling of water would act all the way along the fracture outside the condensation zone.

In order to form a heat pipe, there must be excess capacity for moisture movement beyond

that required to transfer the incoming water to the bottom of the domain. It should be possible to estimate the excess capacity, which in turn provides an estimate for the maximum magnitude of recirculation and the maximum amount of energy bound up in the recirculation cycle. The excess capacity is overestimated by the difference between the maximum gravity flux and the actual flux in the fracture (vapor flux needs some capacity unless it occurs in the matrix).

It is reasonable to assume that the excess flux will not always be mobilized. Rather, the excess flux will not exceed that which creates a monotonic temperature distribution.

A slight modification to the problem may serve to capture the full behavior a bit better. The boiling/condensation behavior is more like a source dipole than a sink, with unbalanced components (some of the latent heat is removed through downward vapor flux, which balances the flux entering the top of the fracture). Perhaps the source and the sink can each be modeled as triangularly distributed over a certain temperature range, where the ranges overlap. An additional source/sink term can be applied uniformly along the fracture from the boundary to the boiling temperature, with a total strength that required to raise the liquid from the initial temperature to boiling. The net source/sink term at any particular location is simply the sum of the three. Note that when the fracture extends above and below the drift, the latent heat lost from above the drift is deposited below the drift, and heat is lost from the liquid as it cools to the bottom boundary temperature. Both of these effects would tend to bring the top reflux zone closer to the drift than the bottom zone would be.

As a practical matter, I would expect that the boiling pattern might drop off rapidly below boiling and not so rapidly above boiling, peaking slightly above boiling. Similarly, I would expect that the condensation pattern would drop off rapidly above boiling and not so rapidly below boiling, peaking slightly below boiling.

A heat-pipe effect would develop from these assumptions. It has to be seen whether the heat pipe bears any resemblance to the heat pipe that develops when fluid motion is explicitly considered. The approach implicitly assumes that the fluid moves readily relative to the flux of energy in the rock. In addition, the approach implicitly assumes that the flux in the fracture is essentially at the carrying capacity for the fracture (so that no excess recirculation can take place).

1/13/99 Fracture junctions. 

I am returning to the process of developing a BEM code sufficient for a poster next month. My existing code is adequate for a relatively few matrix blocks, if some additional coding is performed

to handle intersecting fractures. The procedure generates a large square full matrix, however, restricting the applicability due to computational effort (both in solving the matrix equations and due to the global support for each unknown).

An attractive alternative approach may be to develop the BEM code as a type of finite element code, which would produce a matrix structured similar to a finite element code, with reduced support for each node. I anticipate that such a code would be dramatically faster. The development process may be just a little too long for the poster time frame, but the possibility for speedup is tempting nevertheless. Definitely a production code should use the finite element ideas.

In pondering the physics of fracture flow in unsaturated systems, I realized that there are some fundamental differences between saturated and unsaturated systems. In saturated systems, capillarity is not an issue and flow is driven by head differences and conductivity can be treated as a bulk property. In unsaturated systems, capillarity may have a strong influence on flow, with flow directions that would be possible in saturated systems barred due to capillary effects. A good demonstration was presented by Nicholl and Glass (1995) with a field experiment at YM that showed an infiltration pulse at the large-block experimental site bypassing some fractures by simply stopping at the junction. The key factor that has been neglected is the physics at fracture intersections.

There are basically two situations: a filled fracture meeting the junction and a partially empty fracture meeting the junction. The partially empty fracture is dominated by film flow and capillarity is not important. The filled fracture, however, may or may not allow flow into the junction depending on conditions at the junction. In effect, there is a highly nonlinear conductance just at the exit of the fracture; at low flows and at high flows, the conductance is one, while when the fracture is just saturated with minimal overpressure, flows may be zero due capillarity. The translation of these physical considerations has not been made to numerical simulators, as far as I am aware.

A numerical approach to account for these effects is somewhat complicated. The standard equation under steady-state saturated conditions is a mass balance for junction N,

$$\sum_j C_j(\phi_j - \phi_N) = 0, \tag{5-108}$$

where C is a conductance and ϕ is a potential. Solving for ϕ_N and rearranging, flux from the junction into volume i is

$$q_{Ni} = \frac{\sum_j C_i C_j(\phi_j - \phi_i)}{\sum_j C_j}. \tag{5-109}$$

This relationship assumes that no losses occur and there is a single potential at the junction. This relationship works for vapor flux and conduction.

If film flow is occurring in all incoming junctions, the situation may be the same or may be different. For example, consider a near-vertical joint and a slanted intersecting joint, both with entering film flow. In a saturated system, flow would likely join and move into all downsloping fractures. In the unsaturated system, however, flows from the slanted fracture would tend to be completely diverted into the near-vertical fracture unless the near-vertical fracture became saturated. Similarly, flow in the near-vertical fracture will tend to be diverted into the slanted fracture due to surface tension pulling water around the corner. Note that, if the slanted fracture is capable of carrying the flow, only a small diversion would have the effect of completely cutting off vertical flow. Thus, the local structure at the fracture openings may play a rather important role in flow processes.

At a fully saturated 2D pipette network, the connections should default to the Equation 5-109 formula. A simplified approach may be effective for an unsaturated intersection. Assuming that the fractures are straight and the intersection has an offset, two incoming and two outgoing fractures can be defined.

The incoming fractures could be both unsaturated, both saturated, or one of each. If exactly one fracture is saturated and the hydrostatic pressure is not enough to overcome capillarity, the junction conductance for that fracture is 0; otherwise, the conductance is 1.

All flux is assumed to divert into the outgoing fracture on the down side of the offset joint, unless the fracture must be saturated to carry the flux; in this case, the excess spills into the other fracture.

The pressure in the primary outgoing fracture controls outgoing fluxes. The pressure at the incoming junction can be calculated from this (or be assumed the same), which in turn controls incoming fluxes.

The bottom line expression for unsaturated conditions can be formulated as

$$\sum_j C_j(\phi_j, \phi_N)(\phi_j - \phi_N + \Delta\phi_{jN}) = 0, \tag{5-110}$$

where $\Delta\phi_{jN}$ accounts for capillary effects and C_j is upstream weighted. The flux from volume i across the junction into volume j is

$$q_{ij} = \frac{C_i C_j C_{ij}(\phi_i - \phi_j)}{(C_i C_j + C_i C_{ij} + C_j C_{ij})}, \tag{5-111}$$

where C_{ij} is the conductance linking i and j in the junction. Note that $0 \leq C_{ij} < \infty$, with no flow when $C_{ij} = 0$ and the harmonic average between C_i and C_j recovered as C_{ij} becomes very large.

One approach for determining the unsaturated conductances under conditions of complete film flow is semi-explicit, so that it may have problems with stability. Given the potentials at the surrounding volumes, a local mass balance can be explicitly constructed. Assuming fully upstream weighted fluxes and slanted fractures, incoming film fluxes can be calculated. The outgoing fluxes are allocated preferentially according to offset geometry, so that the conductances can be explicitly calculated. Note that there are 9 possible offset configurations, which reduce to 4 basic configurations that need be considered: (i) 2 entering funneling to a split (4 of 9 cases); (ii) 2 reflections, with the chance of overflow (3 of 9); (iii) a zig zag with dual inputs (1 of 9); and (iv) horizontal or near-horizontal fractures (1 of 9). A case with no offsets reduces to the reflections or horizontal split.

1/14/99 More fracture junctions. SAS

The problem of fracture intersections under unsaturated conditions can be simplified tremendously with the simple shift of considering each intersection as an internal boundary condition. In this case, the details of flow inside the intersection need not be considered and the only condition is an appropriate mass balance at the intersection. It turns out that only three types of mass balance equations suffice for all combinations of offset and fracture orientation. Ultimately, there should be a transition to handle fully saturated fractures, which may be due to using a marker potential at the outlet(s) to the junction.

Note that under saturated conditions, the flux into any one fracture volume is a function of the surrounding potentials (see Equation 5-109). For fully upstream-weighted film flow, the corresponding flux is a function of the upstream potential only and the fracture slope. Actually, film flux is dependent on the energy slope, which should only play a role in the transition between film and saturated flow.

The mass balance equation set for the funnel case is

$$q_3 = -\lambda(q_1 + q_2) \tag{5-112}$$

$$q_4 = -(1 - \lambda)(q_1 + q_2), \tag{5-113}$$

where q_1 and q_2 are incoming fluxes, q_3 and q_4 are outgoing fluxes, and λ is a weighting factor.

Typically, λ is set knowing the last value of the incoming fluxes, letting one fracture receive

all flux up to its capacity and the other receive any overflow. If both are filled to capacity, λ smoothly transitions from the threshold value for both having incipient filling to the corresponding saturated-flow parallel conductance weighting (is this the same value?).

The set for the reflection and zigzag cases is

$$q_3 = -(1-\lambda_1)q_1 - \lambda_2 q_2 \tag{5-114}$$

$$q_4 = -\lambda_1 q_1 - (1-\lambda_2)q_2, \tag{5-115}$$

where the λ values are weighting factors set using the same considerations as in the funnel cases. In this case, however, it may be useful to maintain a potential inside the outgoing fractures to determine the direction of crossover flow.

In all of the above cases, film flow is assumed to occur with incoming fluxes, so that the incoming directions are determined from the slope of the fractures. Because film-flow flux is written as a function of potential, the outgoing fluxes are functions of the incoming potentials.

The case of capillary exclusion can be incorporated as well, with the idea of an internal boundary condition working here too.

When flow reduces to the case of a single outlet or a single inlet, the set of balance relationships is, for completeness,

$$q_2 = -\lambda_1 q_1 \tag{5-116}$$

$$q_3 = -\lambda_2 q_1 \tag{5-117}$$

$$q_4 = -(1-\lambda_1-\lambda_2)q_1, \tag{5-118}$$

where q_1 represents flux at either the single inlet or the single outlet.

The case with horizontal fractures is indeterminant, since the horizontal flow direction is not necessarily known *a priori*. For early simulator experiments, it would be best to not confuse the issue with horizontal fractures.

1/15/99 More fracture junctions. SAS

The issue of transition between saturated and film-flow systems must be addressed for the fracture approach.

In saturated systems, it is straightforward to include an extra equation to solve for the

pressure at the junction. Flux interchanging between junction and fracture i is written by

$$q_i = C_i(\phi_i - \phi_N) = C_i(P_i - P_N + \rho g(z_i - z_N), \tag{5-119}$$

where $C_i = b^3/12\mu$ from parallel-plate theory.

The same equation applies for film-flow systems, except that $C_i = b^3/3\mu$. There is a significant loss of efficiency due to the resistance of a second wall; a smooth transition in coefficients will be necessary for mixed saturated/film flow if the film thicknesses are asymmetric (perhaps due to large apertures). If the fracture is narrow enough to have numerous contacts, potentials are likely to be the same on either face and the flows would be symmetric or nearly symmetric on both faces, so that the transition is automatically smooth.

Generally $C_i = C_i(P)$, which can be written in the form $PC_i'(P)$ for inclusion in the matrix equations. Unless the junction is saturated, $P_i = P_N$ and upstream weighting can be used. Near the transition between unsaturated and saturated systems, there may be some effect from P_N even under unsaturated conditions.

In funnel and zigzag configurations, a single value for P_N is sufficient to determine outflow for both outlets. In reflection configurations, probably a single value would be adequate, but some care in switching would be necessary since the outlets are independent at low flows and linked at higher flows. The best option would be to use the potential for the outlet that is closest to its capacity during an iteration.

1/18/99 More fracture junctions.

SAS

Dani and I discussed the ideas of flow routing through fracture junctions today. One point that Dani made was that there may be film flow on both sides of a fracture, particularly at low flux rates. Without this consideration, I had identified a total of 45 possible configurations for 2 fractures with block movement along either fracture (rather than the 9 identified a few entries ago). There are 3 configurations for the subhorizontal fractures (slope less than, equal to, and greater than horizontal, respectively); 3 configurations for the subvertical fractures (slope less than, equal to, and greater than vertical, respectively); and 5 configurations accounting for offsets [right-lateral or left-lateral along either fracture (4 possibilities), or no offset].

As discussion proceeded, it became clear that the routing of film fluxes through a junction is a bit more complex than just the consideration of geometry and fracture capacities. The additional component accounts for the diversion length of fluid before it forms a drop. The diversion length

increases as the entry-fracture slope steepens and flux decreases. The effect of the diversion is to preferentially change the geometric offset based on film fluxes and fracture slope.

1/19/99 More fracture junctions.

Following up on the idea of symmetric/asymmetric flows, it occurred to me that it is likely that the top and bottom of narrow fractures are at the same chemical potential, due to the numerous asperities. The difference in elevation is perhaps insignificant. However, gravity may tend to pull water particles away from the hanging wall and pull water particles towards the footwall. In turn, absorbance forces may be reduced in the hanging wall and increased in the footwall. Presumably gravity would be more important as the film becomes thicker and absorption forces affect a smaller fraction of the film.

The problem of routing can also be looked at as a matter of tracking fluxes on individual faces or matrix blocks. For all configurations (except perfectly vertical/horizontal) there is one upper block that drips from the corner and one that tends to divert laterally. Once dripping occurs, it may encounter any of the footwall fracture faces for each of the four fracture segments, depending on offset geometry.

When the incoming subhorizontal fracture film intersects the footwall of the subvertical fracture, diversion always occurs into the subvertical fracture. If the hanging wall is intersected, diversion always occurs; however, if there is offset on the subvertical fault, dripping may occur onto the upper-block footwall and the possibility of diversion exists.

1/22/99 Fracture-junction routing algorithm.

There are two criteria for determining whether a junction is completely saturated: (i) all surrounding nodes are saturated, or (ii) film-flow inputs are greater than output capacity. When the junction is saturated, the solution process is linear and straightforward, geometry doesn't determine flow directions, and both upstream and downstream potentials determine flow. There can be between one and three entries and exits.

When the junction is completely dominated by film flow, routing is dominated by face geometries, film-flow capacity, and the distance drops move laterally on hanging faces before dripping occurs, and only the upstream potential determines fluxes. Unless there are horizontal fractures, there are two entries and two exits.

When the junction has a mixture of film and saturated flows, it is necessary to consider capillarity to determine if a saturated fracture is an entry, exit, or neutral fracture. It is probably reasonable to assume that both corners touching a saturated fracture have the same potential. Note that the conditions for flux are a combination of the film and saturated conditions.

An algorithm for calculating film-flow routing (with no fracture saturated) is as follows:

- Calculate the flux capacity for each face
- Find incoming faces and estimate the incoming fluxes
- Sort block corners by elevation
- From highest corner to lowest, route incoming-face fluxes to a downstream face
  - Fixed drip (2 incoming faces): drip on underlying footwall (steeper footwall face wins in a tie)
  - No drip (2 outgoing footwall faces): do nothing
  - Lateral diversion (1 incoming and 1 outgoing footwall face): route from incoming to outgoing
  - Hanging-wall diversion (outgoing face is hanging wall): route along outgoing face to capacity, calculate lateral diversion for the remaining fluxes, and route the remaining at that point
- Accumulate the upstream flux for each face and the fraction of the upstream-face fluxes that make it to the downstream face
- Calculate the weights for outgoing fractures using the face information

The algorithm depends on the previous iteration to provide incoming fluxes; however, for low flux rates the weights will generally be independent. The only exception is if lateral diversion occurs before dripping, and if the diversion may cause dripping to reach different faces with different fluxes.

Mass balance is implicit with the completely film-flow formulation. Mass balance can be implicit with the completely saturated formulation.

1/25/99 Algorithm with some saturated fractures. SAS

There are several cases where a mixture of saturated and unsaturated fractures is relatively straightforward. When there are three saturated fractures, the formulation is essentially that of the fully saturated case, with one unknown potential at the junction. When two opposed fractures are saturated, unless dripping occurs the formulation is essentially two independent fully saturated problems. The flux on a face attached to the saturated fracture is given by Equation 5-109.

References

Ingber, M. S. and A. K. Mitra. 1989. The evaluation of the normal derivative along the boundary in the direct boundary element method. *Applied Mathematical Modelling 13*, 32–40.

Liggett, J. A. and P. L.-F. Liu. 1983. *The Boundary Integral Equation Method for Porous Media Flow.* London, England: George Allen & Unwin.

Nicholl, M. J. and R. J. Glass. 1995. A Field Experiment Exploring Fracture Network Geometry, Connectivity, and Unsaturated Flow Processes. *Supplement to Eos, Transactions 76*(46), F196.

Pullan, A. J. and I. F. Collins. 1987. Two- and Three-Dimensional Steady Quasi-Linear Infiltration From Buried and Surface Cavities Using Boundary Element Techniques. *Water Resources Research 23*(8), 1633–1644.

Stothoff, S. A. 1991. *A Boundary Integral Technique for Modelling Two-Phase Flow in Porous Media.* Ph. D. thesis, Princeton University, Princeton, NJ.

NOTE: No original text entered into this Scientific Notebook has been removed.

R Fedors for SAS 10/27/99
Stuart Stothoff **Date**

Per Stothoff signed note on page 9-43 April 11, 1999 entry, the entries into Scientific Notebook #163 for the period November 16, 1995 to April 11, 1999, have been made by Stuart Stothoff — R. Fedors 10/27/99

[See page viii of this quarterly notebook submittal]

SCIENTIFIC NOTEBOOK

by

Stuart A. Stothoff

Southwest Research Institute
Center for Nuclear Waste Regulatory Analyses
San Antonio, Texas

April 11, 1999

Initial Entries

Scientific NoteBook: # 163

Issued to: S. A. Stothoff

Issue Date: Tuesday, November 16, 1993

By agreement with the CNWRA QA this NoteBook is to be printed at approximate quarterly intervals. This computerized Scientific NoteBook is intended to address the criteria of CNWRA QAP–001.

Table 0-1: Computing Equipment

Machine Name	Type	OS	Location	Current
dimension	Dell Dimension	Windows 98	desk	yes
inspiron	Dell Inspiron	Windows 98	desk	yes
latitude	Dell Latitude	Windows 95	desk	yes
sierra.cnwra.swri.edu	Sun SPARC 20	Solaris	desk	yes
sisyphus.cnwra.swri.edu	Sun SPARC 20	SUNOS 4.1.3_U1	network	no
dopey.cnwra.swri.edu	Sun SPARC 10	SUNOS 4.1.3_U1	network	no
performer.cnwra.swri.edu	SGI Onyx	IRIX 5.3	network	no
yosemite.cnwra.swri.edu	SGI Onyx	IRIX 5.3	network	no
bemore.cnwra.swri.edu	SGI Onyx	IRIX 6.2	network	no
redwood.cnwra.swri.edu	SGI Indy	IRIX 6.2	network	no
bigbend.cnwra.swri.edu	Sun Ultra-2	SUNOS 5.5.1	network	no
scratchy1.cnwra.swri.edu	Sun Ultra-2	SUNOS 5.5.1	network	no
hornet.cnwra.swri.edu	Sun Ultra-2	SUNOS 5.5.1	network	no

Contents

List of Figures

List of Tables

1. Ambient Hydrology KTI – Infiltration

Account Number: **20-5708-861**
Collaborators: **Amvrossios Bagtzoglou, Gordon Wittmeyer**
Directories: **$SubRegBreath and as noted**

Objective: Perform detailed analysis of the spatial and temporal distribution of infiltration at Yucca Mountain (YM). A good deal of previous work is documented in the Scientific Notebook for the Subregional Flow and Transport Processes Research Project (subregional project) and various publications under the subregional project and the umbrella of the Iterative Performance Assessment and Performance Assessment Research projects. The research projects were closed out due to reorganization of the NRC and consequently CNWRA; infiltration work is largely being subsumed under the Ambient Hydrology KTI, with some applications possible under the Thermal Effects on Flow KTI in order to examine heating effects on infiltration. Initial efforts in the new project are to be directed towards documenting the work already completed in journal articles. Future work will depend very much on funding and time availability, but several avenues that may be explored include: (i) the impact of matrix-fracture interactions; (ii) watershed-scale modelling, with vegetation and lateral flow accounted for; (iii) geochemical tracer verification; and (iv) "shallow" diversion of infiltration due to the PTn layer.

1/26/96 Initial entry. SAS

Work on infiltration under the subregional project and IPA is currently being documented in two journal articles. The first article deals with the impacts of hydraulic properties on 1D infiltration; the second looks at meteorology, documents the alluvium flow model, and estimates spatial and temporal distributions of infiltration. All simulations to date have been 1D; the first sets examined semi-infinite alluvium columns, with later sets looking at a shallow alluvium layer over a fracture continuum. It is quite clear that the fracture continuum will allow far more water to infiltrate than the alluvium columns; a relatively thin alluvium coating (less than 50 cm) will shut off fracture flow entirely, but sufficiently deep alluvium (greater than 5 m) will allow the flow to resume; hillslopes and ridgetops are the most important infiltration areas; micrometeorology is not a great factor, nor is the fracture description if there is enough fracture porosity; alluvium hydraulic properties have a significant influence, increasing with depth, but the depth of alluvium is the single most important parameter; detailed hourly description of meteorology is only important near precipitation events; and it is critical to use arithmetric averaging or upstream weighting for conductivities in the fracture

soils may make predictions of *MAI* in shallow soils more robust than predictions in deep alluvium.

ACKNOWLEDGEMENTS

This paper was prepared to document work performed by the Center for Nuclear Waste Regulatory Analyses (CNWRA) for the Nuclear Regulatory Commission (NRC) under Contract No. NRC-02-93-005. The activities reported here were performed on behalf of the NRC Office of Nuclear Material Safety and Safeguards, Division of Waste Management. The paper is an independent product of the CNWRA and does not necessarily reflect the views or regulatory position of the NRC. The authors would like to acknowledge the suggestions and comments made by G. Wittmeyer, B. Sagar, D. Woolhiser, and two anonymous reviewers, which tremendously improved the quality of the paper.

CNWRA-generated data contained in this document have been documented according to quality assurance requirements described in the CNWRA Quality Assurance Manual. Sources for other data should be consulted for determining the level of quality for those data. Neither the HYDRUS-2D simulator nor the root-growth simulator is configured under the CNWRA's Software Configuration Procedure. At present, the CNWRA does not anticipate the use of either of these codes for regulatory reviews.

3/6/99 Documentation for shallow-soil MAI abstractions.

In the process of reviewing a paper on shallow-soil abstractions for *MAI*, R. Fedors requested that I provide

- The spreadsheet for estimating coefficients
- *breath* input files for a fracture fill and infinite-soil column to be able to verify some points
- *breath* input and output files for unfilled fractures
- Post-processing scripts

In response, I am collecting all of the results into a documentation CD-ROM, including relevant papers, notebook entries, etc. The CD-ROM will be placed in QA storage.

3/30/99 Error in shallow-soil MAI abstractions.

As I was testing a *Matlab* simulator that will be used to calculate *MAI* in the presence of plants, I discovered a flaw in my assignment of fracture properties. I had realized that the porosity of the

fracture fillings needed to be multiplied by the fraction of the cross-sectional area occupied by the fractures. I had not realized that the permeability of the fracture fillings also needs to be adjusted. This misconception should not affect the regression analysis at all, except perhaps the capillary-barrier regression has less of a range in permeability than I originally thought. The capillary-barrier regression should not be materially affected in the unfilled-fracture parameter subspace.

The primary impact of the misconception is on estimates of *MAI*, driving down the estimates. It appears that there may be relatively little impact under present-day climate and soil, but under future soils *MAI* in a soil-fracture system may be drastically smaller. With the revised concept, *MAI* is much more sensitive to the fracture cross-sectional area.

With the corrected method of estimating fracture permeability, I recalculated the areal-average *MAI* over the repository. Otherwise using the same assumptions as was used for the AGU poster last fall, revised repository-average *MAI* was 8.8, 80, and 29 mm/yr for current, early glacial, and late glacial conditions. The corresponding values of *MAI* were 15, 106, and 45 mm/yr before.

Earlier, I had to artificially put the fraction of fractures containing soil to zero in some units because *MAI* in these units was dominated by the small soil-filled fraction. Revising these units to have a small soil-filled fraction had little effect. Only three categories showed appreciable control: unfilled, deep-soil, and bedrock (soil-filled and carbonate-filled fractures had minimal to no incidences of control).

Re-examining the fracture descriptions used by USGS, my feeling is that the caprock and TCmnl units have under-represented fracture area. I suspect that the fractures used by USGS may not represent fractures in outcrops and shallowly covered cases. For example, I think the caprock should have a description with something like 5 to 15 percent fissure area, while the USGS has a description with 9.2 fractures per meter, averaging 250 μm (or 0.23 percent). Similarly, the fracture area of the middle nonlithophysal turns out to be about 0.026 percent; at the surface I think this should be about two orders of magnitude greater. Increasing these units into a more representative area only minimally increases *MAI* (from 8.8 to 9.1 mm/yr) but results in 1/4 of the repository area having fracture control.

3/25/99 Plant activity considerations. SAS

This entry is intended to clarify my thoughts on procedures for handling plant growth.

In an annual cycle for a perennial shrub, there are several phases:

- Early growth, in which most fine roots and leaves appear. Transport systems are under-utilized.
- Sustained growth, in which the entire plant grows more or less in equilibrium and allocates resources to reproduction. All systems are well utilized.
- Die-back, in which fine roots and leaves die but the transport system is maintained.
- Minimal maintenance, in which a bare minimum of transpiration occurs to satisfy the respiration needs of the transport system.

A common thread through the cycle is an emphasis on maintaining the resource-intensive transport infrastructure.

Plant growth/death can be handled as a constrained optimization problem, allocating nutrient uptake to respiration and growth processes. The constrained optimization problem results from the allocation of nutrients taken up during a day. The nutrients are allocated to respiration demands, growth, and reproduction. Transpiration can be adjusted by the plant to curtail uptake to the most that can be used by the plant, thus minimizing waste. Objectives addressed by the allocation process include:

- Maximizing overall long-term growth
- Maximizing reproduction

Note that reproduction generally requires replacement of existing biomass subsequent to death.

One way to treat the optimization is to maximize nutrient uptake through a global assessment. Each time step, the sensitivity of nutrient uptake to change in plant properties is calculated, where a plant property is any vegetation density component in a computational segment. If there are 20 segments, each with 4 vegetation densities, a first-order sensitivity calculation is calculated by perturbing each of the eighty components and assessing changes in uptake. If the sensitivity

calculation is cheap, this approach is fine, but may be unattractive if the sensitivity calculation requires the solution of a matrix equation.

An alternate way to get at the same thing is by doing a local optimization using local characteristics. A good criterion for allocation is the efficiency of transport through the component. If the component is oversized, it should be cut back; if the component is undersized, it should grow. The criterion might be the deviation of chemical-potential gradient from a nominal gradient, or equivalently a flux per unit area; if the gradient or flux is smaller than nominal, it is too efficient and needs pruning.

As the plant system is hierarchical, subcomponents should exert pressure on a component if they are close to capacity, since capacity is achieved in favorable environments. In order to achieve this goal, the nominal gradient should correspond to the subcomponents at something less than full capacity; subcomponents at greater than this nominal value will supply more flux than the nominal and put pressure on the component to expand. A target value might be something like 80 percent of capacity, to enable growth. The local strategy results in a simple sensitivity test for growth and death. Note that the environment provides forcings for the finest roots and leaves, with wet conditions providing a strong impetus for growth.

Respiration demand is another factor that needs to be accounted for. There should be incentive for allocating nutrient to respiration demand. The incentive should be much stronger than incentives for growth and death, and the relative weight should be proportional to the cost of replacement (higher-order components have stronger priority than lower-order components like fine roots and leaves). In other words, not satisfying respiration demands is painful, and high-order components feel relatively greater pain.

The optimization problem can be formulated as

$$\max \sum_i W_r C_n (R_i - R_{io}) + W_g C_n (G_i - G_{io}), \tag{3-42}$$

where W_r is the weight assigned to respiration, C_n is the nutrient cost per unit biomass, R_i is nutrient allocation to satisfy respiration demand, R_{io} is respiration demand for nutrients, W_g is the weight assigned to growth/death, G_i is nutrient allocation to growth, and G_{io} is maximum growth demand for nutrients. The optimization problem is subject to the constraints

$$0 \le R_i \le R_{io} \tag{3-43}$$

$$0 \le G_i \le G_{io} \tag{3-44}$$

$$G_i = 0 \qquad \text{when } R_i < R_{io} \tag{3-45}$$

3/26/99 More plant activity considerations. SAS

Another approach replaces optimization with a set of partial differential equations that change mass/root-length density according to local fluxes. The idea is to change the allocated mass according to the ratio between actual flux and nominal capacity. The partial differential equation for density change based solely on flux (no other limiting factors) is simply

$$\frac{\partial \rho}{\partial t} = \alpha \frac{q - q_o}{q_o} \rho \tag{3-46}$$

where ρ is the current density, α is a time constant related to cost of growth, q is the actual time-averaged flux over the time period, and q_o is the nominal time-averaged flux corresponding to ρ. Note that the multiplier of ρ should be greater than -1 (for plants, this condition is almost certainly reached for daily time steps, as either the time constant is larger than a day (for transport) or the q ratio doesn't drop to 0 instantaneously.

Growth can be constrained by capacity limits as well. Incorporating capacity constraints yields

$$\frac{\partial \rho}{\partial t} = \alpha \left(\frac{q - q_o}{q_o} \right) \left(\frac{\rho_o - \rho}{\rho_o} \right) \rho \tag{3-47}$$

where ρ_o represents the density at capacity.

The q_o values can be estimated from dividing typical flux values by typical active cross-sectional areas, leaf areas, or root-uptake surface areas, respectively. For example, if a shrub transpires an average of 1 mm/d under nominal conditions, dividing the respective areas by this rate gives nominal flux values per unit area. Hopefully ballpark estimates are sufficient for these parameters.

The time constants arise from considerations of response times under optimal conditions. For example, the time constant for main shrub roots might be on the order of a year, while the time constant for fine roots might be on the order of days. The time constant for leaves is probably on the order of weeks.

It is not clear whether the time constant should be different for death and growth. It can be argued that leaves and fine roots die quicker than they grow, while main transport systems may be reversed. The time constant may change according to environmental stress, with faster death rates and slower growth rates for a wet year after two dry years than for the same wet year after a wet year.

3/27/99 More plant activity considerations. SAS

I coded up a test case for multiple vegetation types simultaneously extracting water from a stagnant column to examine the partial-differential-equation approach and associated constants. The test was of a 50-cm column of soil with no evaporation or bedrock fluxes, and the vegetation was assumed to achieve a vapor density of 2×10^{-5} gm/cm^3 (with atmospheric vapor density of 2×10^{-6} gm/cm^3 and reasonable turbulence). It quickly became apparent that I had to reduce the plant conductivity by the fraction of the total area occupied by plant stems. The actual conductance of stem roots should be like a sand, which has the range of roughly 10^{-9} cm^2 to 10^{-5} cm^2. The higher end may be too conductive, while a value in the midrange seems to give somewhat plausible results.

The conductance of the fine roots is questionable: a fairly small value seems to be necessary.

Allowing the plants to adjust root density according to the nominal-flux criterion for the test problem results in a pressure profile in the soil and plant continua that is almost identical even when the plants initially have sufficiently low densities that the plant pressures are much lower than the soil pressures while supplying vapor flux at the maximum rate. At early times, the plants proliferate exponentially at all depths. As the top dries out, plants that start loosing water adjust the fine-root biomass density down to cut transfer losses.

The permeability of the plant transport strongly affects the dryout profile. For permeabilities comparable to relatively fine sands, a sharp drying front develops. For relatively coarse sands, the front is much more diffuse. For low-permeability transport systems, the transport density tends to drop off more rapidly with depth.

I realized that the change in density term should read

$$\frac{\partial \rho}{\partial t} = \left(\frac{q - q_o}{q_o}\right)\left(\frac{\rho_o - \rho}{\rho_o}\right)\rho \tag{3-48}$$

with the terms in front of ρ on the right-hand side limited to $\pm\alpha$. There is still some question in my mind as to how constraints from nutrients can be accommodated.

1/25/99 Algorithm with some saturated fractures. SAS

There are several cases where a mixture of saturated and unsaturated fractures is relatively straightforward. When there are three saturated fractures, the formulation is essentially that of the fully saturated case, with one unknown potential at the junction. When two opposed fractures are saturated, unless dripping occurs the formulation is essentially two independent fully saturated problems. The flux on a face attached to the saturated fracture is given by Equation 5-109.

2/16/99 Observations after the Witherspoon symposium. SAS

Paul Witherspoon made an observation regarding how difficult the YM problem is, due to the coupled HTMC processes in fractures during the thermal pulse. It occurred to me that the boundary integral approaches that I have been investigating are ideal for elastic deformation (or so I have repeatedly read). It should be relatively straightforward to implement a classic elastic solid deformation model, with the resulting impacts on fracture apertures and permeability due to normal and shear strains.

After pondering some more, it occurred to me that perhaps the chemistry effects could also be incorporated. The restrictions are similar to the restrictions placed on moisture redistribution, although perhaps somewhat more stringent.

The boundary integral approach is most easily applied for several conditions: (i) steady state, (ii) quasi-steady matrix, or (iii) completely disconnected matrix. The steady state condition is the easiest, as only boundary integrals and discontinuity values are required. The quasi-steady matrix is also fairly straightforward, with the matrix essentially acting as a special finite-volume element. A completely disconnected matrix is also straightforward, as only fracture equations need be considered.

When the matrix participates to an intermediate extent, the unmodified boundary integral approach fails due to the deviation from required assumptions. Typical failures are due to transience at an intermediate time scale. When the matrix behavior exhibits transience on time scales comparable to the problem time scales, standard domain discretization methods are required. However, when some matrix interaction is limited to a skin about the fracture and the remainder is either quasi-steady or disconnected, the finite volumes representing fractures can be replaced with a finite-volume mesh extending perpendicular to the fracture. Either a 1D extension or a full grid can be used, depending on the problem.

The skin approach is probably appropriate for YM chemistry near the drifts during the thermal pulse, where the skins represent thin precipitation/dissolution fronts. Note that the assumption of quasi-steady THM components with transient C components may be appropriate for YM. The description of the TH fractures would have layered permeability as described previously, while it may be possible to neglect the layering for the M components. It may be that only the C components require a finite-volume mesh.

Another thought occurred to me recently: a multiple-continuum system can be conceived of as a type of layered aquifer/aquitard system. There is a Green's function developed for the latter case (Cheng and Morohunfola, 1993a, Cheng and Morohunfola, 1993b) that may be specialized for multiple overlapping continua. The presented solutions are for cases where the responses of the aquitards are significant, using Laplace transforms. However, the development should be able to be simplified to neglect the aquitard transience. The ideas may be of some use in considering saturated problems.

to construct a linear approximation that should remain stable; however, the beta distribution can yield PDFs that go to infinity at endpoints (although histograms do not).

A reasonable method for handling the problem is to use the histograms to calculate changes in mean and variance, assuming that the change in the mean and variance used for the beta distribution is the same as the change in the mean and variance of the histogram distribution. This avoids the reconstruction issue entirely, while preserving the computational flexibility of the histogram approach with parameter parsimony of the beta distribution.

A test problem illuminates a difficulty with a single beta distribution. The problem is that of an initial triangular distribution subject to weathering and freeze-thaw breakup. The shift in mean and standard deviation to lower grain sizes tends to make the beta distribution create a bimodal distribution, ultimately with all mass concentrated in the two endpoint bins. This occurs whether the distribution starts with the bulk of the mass in the large or small grain sizes, and I believe that this is purely a numerical artifact.

2/22/99 Temperature distribution calculation. 

I started a directory ***$HOME2/Matlab/Chadwick/SoilGen2*** for the next phase of modeling.

Weathering rates are temperature-dependent, and temperature variation is depth dependent. It is probably sufficient to use analytic solutions for temperature variation with depth, and to only consider annual variation (neglecting daily variation due to the shallow depth penetration of daily perturbations). The use of analytic solutions means that only a mean annual temperature and an amplitude are necessary to characturize the profile.

I resurrected a set of routines to calculate clear-sky shortwave radiation as a function of latitude, day, hour, and ground-surface rotation. The time history of clear-sky shortwave radiation over the year can be calculated.

An energy balance at the surface provides an estimate of soil temperature at the ground surface. The balance equation is

$$\sigma \sum_i \epsilon_a T_a^4 \Delta t - \sigma \sum_i \epsilon_s T_s^4 \Delta t + D_h \sum_i \Delta t (T_a - T_s) + q_{sw} - q_{geo} + q_s = 0 \qquad (9\text{-}65)$$

where σ is the Stefan-Boltzmann constant, ϵ is emissivity, T is temperature, D_h is the diffusion coefficient for heat, q is flux, and the a, s, sw, and geo subscripts refer to atmosphere, soil, net shortwave, and geothermal, respectively.

Characterizing T_s as

$$T_s = \bar{T}_s + A_0 \sin[\omega(J - t_0)] \tag{9-66}$$

where $\bar{T}_s$ is mean annual soil temperature, ΔT_s is soil temperature amplitude, ω is frequency ($\omega = 2\pi/365.25$), t_0 is a day shift, and J is julian day, yields an expression in three unknowns ($\bar{T}_s$, A_0, and t_0). The analytic solution for this problem is (Campbell, 1977)

$$T(z,t) = \bar{T}_s + A_0 \exp(-z/D) \sin[\omega(J - t_0) - z/D] \tag{9-67}$$

$$D = \left(\frac{2k_h}{\omega C_h}\right)^{1/2} \tag{9-68}$$

where z is depth, k_h is thermal conductivity, and C_h is thermal capacitance. The soil heat flux at the ground surface can be found by differentiating and rearranging, yielding

$$q_s = A_0 \left(\frac{\omega C_h k_h}{2}\right)^{1/2} \{\sin[\omega(J - t_0)] + \cos[\omega(J - t_0)]\}\,. \tag{9-69}$$

The three unknown coefficients describing temperature can be solved for using standard least squares.

Generally it is necessary to break the day up into enough pieces to calculate the shortwave variation over the day. An hour or so is probably adequate for moderate ground-surface rotations, but for large north-south rotations (greater than 30 degrees) it is necessary to break up the day into 5-minute intervals or so for reasonably accurate calculations. Also note that the shortwave radiation loading starts significantly deviating from a sinusoid at such large rotations; for part of the year no sunlight may hit steep north-facing slopes. Accordingly, assumption of a sinusoidal temperature may not be totally valid.

3/1/99 Mean temperature distribution calculation.

A set of observations was performed by the USGS in Split Wash in 1997, with net radiation observed in the middle of the wash from days 50 through 212 (February 19 through July 31) and heat dissipation observed on north-facing (days 36 through 212) and south-facing slopes (days 17 through 212). Net radiation is calculated from four thermometers in the atmosphere (every 15 min), while heat dissipation is calculated from thermometers at two depths in the soil (every 6 hr). These data provide an opportunity to calibrate the temperature model.

Temperature is dependent on shortwave radiation, longwave radiation, dissipation into the subsurface, and sensible-heat diffusion across the boundary layer. Shortwave radiation is dependent on the path of the sun, the ground slope, and obscuration due to atmosphere and clouds.

Longwave radiation is dependent on emissions from clouds, clear sky, and the ground surface, in turn dependent on cloudiness and atmospheric vapor density. Dissipation into the ground surface is dependent on the frequency of perturbations and material properties. Sensible-heat fluxes are dependent on the temperature difference across the boundary layer and the windspeed.

A fairly simple approach to predicting soil temperature relies on predicting the annual variation of the mean and superimposing perturbations on an hourly basis, decaying temperature appropriately with soil depth. In order to predict mean variation in soil temperature, the annual cycles of cloudiness, vapor density, and wind speed are useful. Mean values for all of these vary approximately sinusoidally over the year, as does atmospheric pressure. Each of these also have characteristic daily variations as well. Only cloudiness may require the daily variation to be taken into account, and only for shortwave contributions, as there is a peak in cloudiness during the most intense period of the midafternoon.

Hourly Desert Rock data is available for 1978 through 1994, of reasonable length for making calculations of annual atmospheric variation. These hourly data were aggregated into mean daily values and a sine wave was fit to each resulting aggregate curve,

$$v = \bar{v} + A\sin[\omega(J - t_0)] \tag{9-70}$$

where v is the variable being fit and $\bar{v}$, A, and t_0 are fitting parameters. The match between data and model was made based on a least-squares fit, using a *Matlab* routine called fmins. The set of sinusoid fits are shown in Table 9-3, with plots of the data and matched curves shown in Figure 9-1.

Table 9-3: Parameters describing sinusoidal variation of atmospheric variables in form $v = \bar{v} + A\sin[\omega(J - t_0)]$.

Variable	$\bar{v}$	A	t_0
Windspeed (m/s)	4.07831	-0.441414	224.826
Relative Cloudiness	0.325176	-0.134497	136.154
Relative Humidity	0.331675	-0.134384	103.069
Temperature (C)	17.2165	12.1006	109.589
Pressure (mbar)	1136.81	-52.1159	87.7265

Note that vapor density is not fit well with a sinusoid (it depends on relative humidity and is exponentially dependent on temperature), but can be calculated from relative humidity and temperature (both of which are reasonably well captured). Even so, still not a particularly good fit, as hourly variations between these are inversely correlated. The inverse of vapor density is arguably

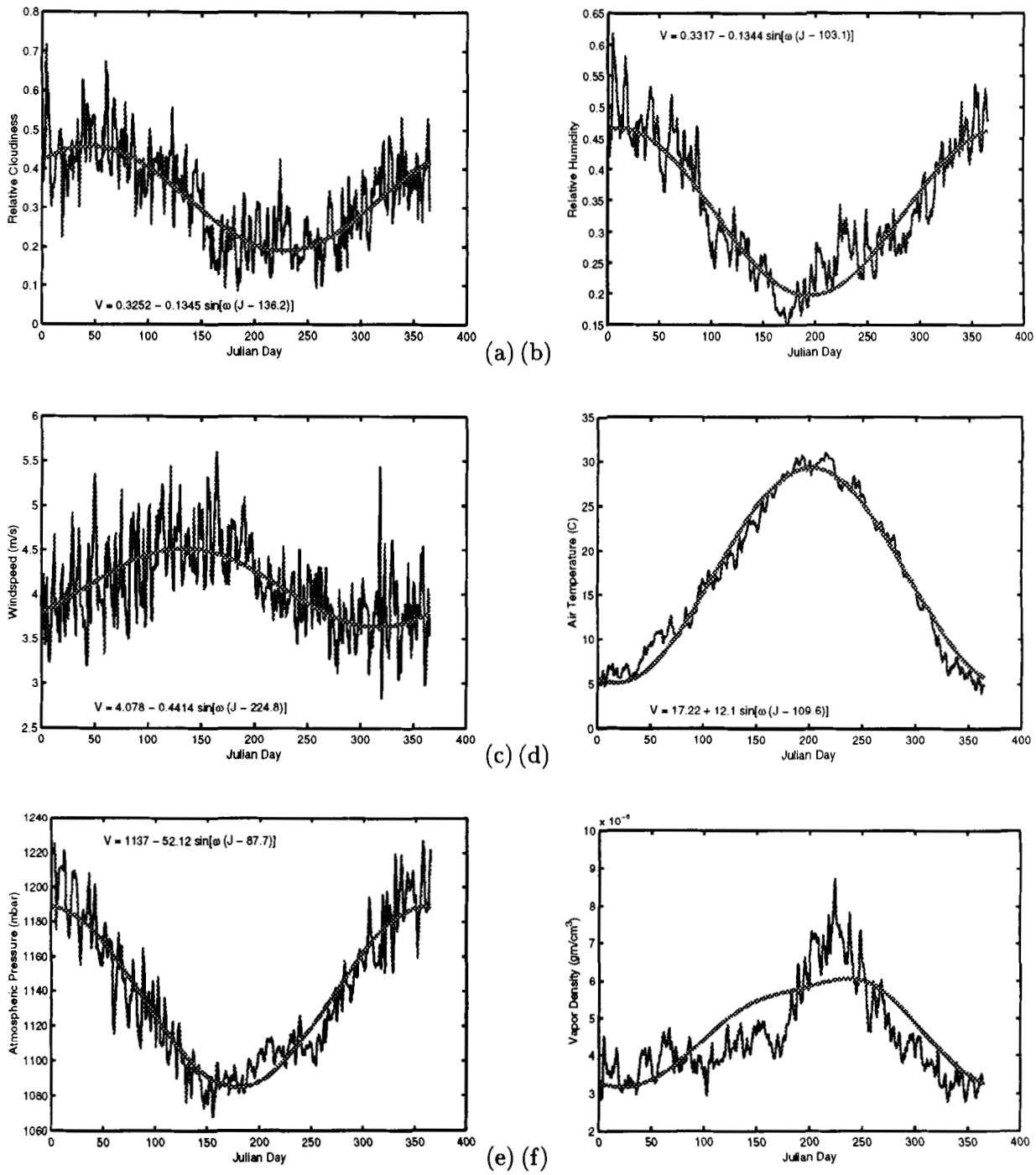

Figure 9-1: 3/1/99. Observed and predicted mean annual variation in (a) cloud cover, (b) relative humidity, (c) wind speed, (d) air temperature, (e) atmospheric pressure, and (f) vapor density.

fit the best using a sinusoidal functions among several options I tried. Perhaps a joint match of relative humidity, temperature, and vapor density would help. Fortunately, the sensitivity of soil temperature to vapor density is quite low.

3/2/99 Mean temperature distribution verification. 

A comparison of the daily average incoming longwave and net shortwave components of atmospheric radiation are plotted in Figure 9-2, with a comparison to the comparable mean components calculated using the annual cycles of cloudiness, relative humidity, and vapor density. The daily average components are calculated using the average of the hourly readings for each day, and should account for fine-scale variability. The match is quite good.

Using the mean energy-balance components with an assumed boundary-layer sensible-heat diffusion coefficient, soil temperature can be estimated using a sinusoidal fitting function, as discussed two entries above.

Measured soil and air temperatures are available for Split Wash, as discussed in the previous entry. The measured temperature profiles only cover part of a cycle and do not unambiguously contain either peak. However, it appears that the summer soil peak is roughly 29 and 32 degrees Celsius for north-facing and south-facing slopes (averaged over both depths), respectively, and the winter soil peak may be roughly 4 and 8 degrees Celsius, respectively. These are probably correct to within plus or minus 2 degrees.

Using the diffusion coefficient as a fitting parameter, reasonably good matches to the data are found, as shown in Figure 9-3. Reasonable matches were obtained for D_h in the range 5×10^{-3} to 10×10^{-3} J/s cm^{2}K, prior to checking plausible values. Note that D_h is dependent on the difference between soil and air temperatures, and requires an iterative process to estimate. Checking for plausible values of D_h with representative windspeeds and temperatures suggests that the lower two-thirds of this range are most reasonable.

A brief sensitivity test for input parameters suggests that:

- A thirty-percent change in cloudiness has minimal effect
- A fifty-percent change in atmospheric emissivity changes T by 2 degrees
- A fifty-percent change in vapor density has minimal effect

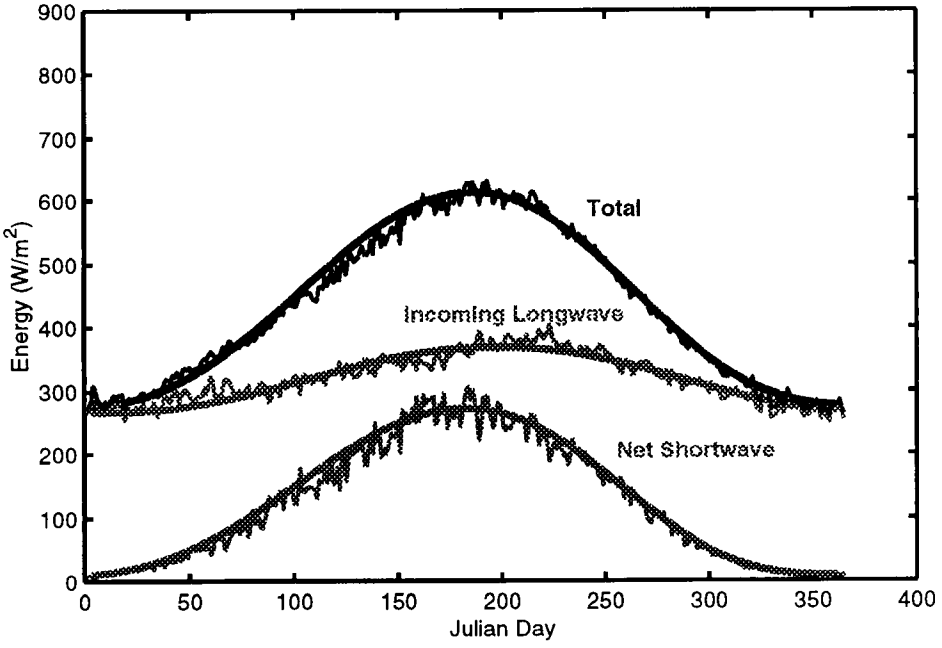

(a)

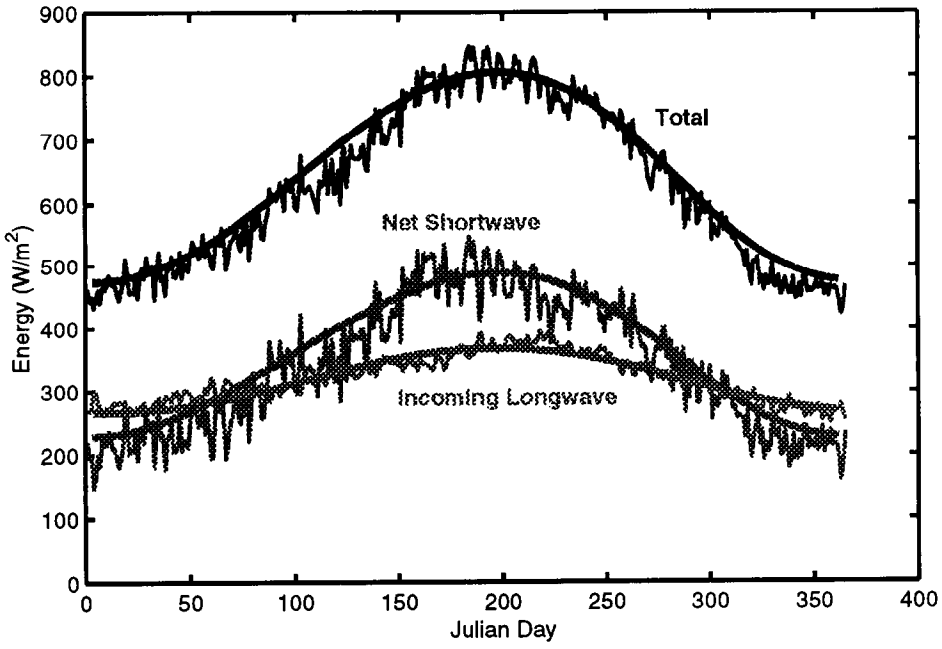

(b)

Figure 9-2: 3/2/99. Average daily and predicted mean annual values of radiation components for Split Wash slopes facing (a) south and (b) north with a slope of 25 degrees, using 1974 through 1994 Desert Rock observations. Albedo is assumed to be 0.1.

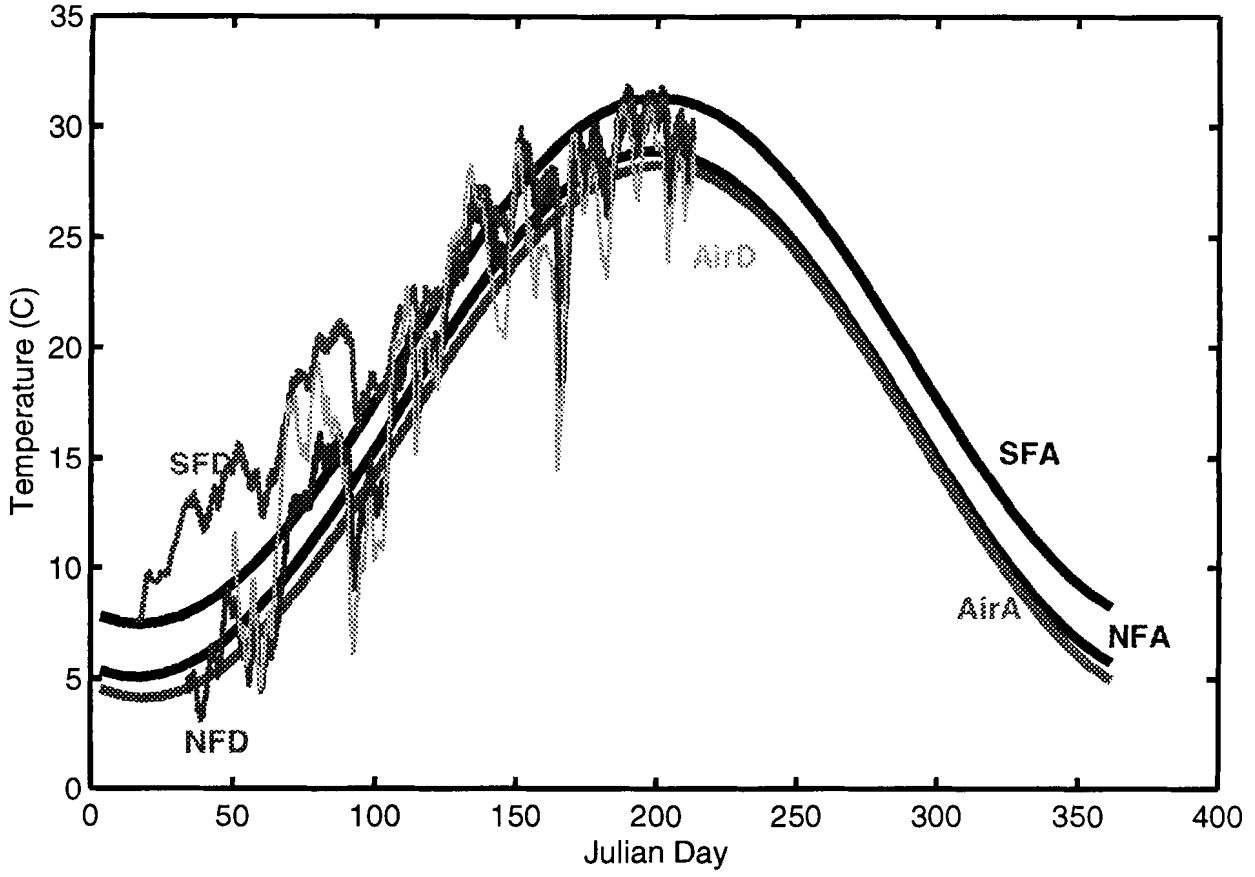

Figure 9-3: 3/2/99. Average daily and predicted mean annual temperatures for Split Wash north- and south-facing slopes and air temperatures. Temperatures increase from air to north-facing to south-facing. Temperature labels: AirA, analytic (sinusoidal) air; AirD, Split Wash daily average; NFA, north-facing soil analytic (30 cm deep); SFA, south-facing soil analytic (30 cm deep); NFD, north-facing soil data (29.2 cm deep); SFD, south-facing soil data (35.6 cm deep). Modeled albedo is 0.1 and boundary-layer diffusion is 7.2×10^{-3} J/s cm^2 K.

- A change in albedo from 0.1 to 0.4 drops mean temperatures by 0.6 and 1.6 degrees C for north-facing and south-facing slopes, respectively, with drops in summer larger than in winter
- Changes in air temperature are directly reflected in changes in soil temperature
- A change in soil emissivity from 0.9 to 0.95 drops mean temperatures by 0.3 degree C
- A change in soil diffusivity by a factor of two has minimal effect

- A change in D_h from 6.2×10^{-3} to 4.2×10^{-3} has a similar effect as changing albedo, with mean temperatures raising by 0.5 and 1.8 degree C for north- and south-facing slopes, respectively. Again the rise is larger in summer than winter.

For soil modeling purposes, the primary factors to capture are air temperature and slope, with less-important secondary factors of albedo and boundary-layer diffusion coefficient (windspeed).

Another factor to consider is what happens to the soil temperature over a daily cycle. This is important for freeze-thaw cycles, for example. In addition, since weathering is proportional to 2^{T-T_0}, perturbations about a mean yield a higher effective rate.

The Beatty data set provides minimum and maximum temperatures over the range from 1948 through 1994, with several missing intervals. The difference between maximum and minimum temperature varies slightly over the year, with the mean difference (all temperatures in Celsius) having the relationship $\bar{\Delta} = 18.3727 + 2.7465\sin[\omega(J - 113.2405)]$. A histogram of the deviation from the mean is slightly skewed, with a mean of -0.5636 and a standard deviation of 4.

The mean temperature (the mean of maximum and minimum), $T = 15.5172+10.7973\sin[\omega(J-112.1112)]$, is fairly similar to Desert Rock, with a mean 1.7 degrees cooler and an amplitude 1.3 degrees smaller. A histogram of the deviation from the mean is less skewed than the corresponding temperature-difference case, with a mean of -0.1821 and a standard deviation of 3.6179. The correlation between daily-mean deviation and temperature-range deviation is 0.241. From this information, assuming normality for both distributions should allow calculation of the number of freeze-thaw days and the fraction of time spent at various temperatures over the course of a year.

3/3/99 Perturbed temperature distribution. SAS

The fraction of days with a freeze-thaw cycle can be calculated given the mean temperature, the variance of the daily average deviation from the mean, and the variance of the temperature range. Noting that the two variance variables are assumed normal and correlated, realizations are generated by first sampling one. The other is then created from the first using

$$m_{Y|X} = m_Y + \rho\frac{\sigma_Y}{\sigma_X}(x - m_X) \tag{9-71}$$

$$\sigma^2_{Y|X} = (1 - \rho^2)\sigma^2_Y \tag{9-72}$$

where m represents the mean, σ^2 is the variance, and ρ is the correlation coefficient. A table can be created for the temperatures with significant numbers of freeze-thaw cycles (generally in the range

of $\pm 3(\sigma_X^2 + \sigma_Y^2)^{1/2}$). The table should use roughly 1-degree steps within this range; it is reasonable to use at least 10^5 realizations per temperature for a smooth function. For each day of the year, given a mean temperature the expected number of freeze-thaw cycles can be calculated from the table; these can then be summed to yield an annual average.

The fraction of days with a freeze-thaw cycle is bell-shaped as a function of mean temperature, and is centered on 0 degrees C with no correlation. With a positive correlation the peak is shifted below 0, while with a negative correlation the peak is shifted above 0. For reasonable inputs the shifts are only a degree or so. Halving the standard deviation for daily temperature range halves the fraction of days with freeze-thaw cycles. Doubling the standard deviation for daily average deviation also halves peak, but doubles the spread of the curve and doubles the shift due to the correlation coefficient.

At a depth within the soil column, temperature perturbations decay, with effect of shrinking both standard deviations equally. The net effect would be to keep the same peak but decrease the spread of the curve.

The weathering rate (given sufficient moisture) is stated in the general form

$$R = A2^{\alpha(T-T_0)} \tag{9-73}$$

where T is temperature, R is the weathering rate, A and α are constants, and T_0 is a reference temperature. Note that $\alpha = 10$ (doubling in weathering for each 10 degree increase in temperature. Since temperature is essentially normally distributed, R has a larger mean than median. To handle this, note that the relationship can be rewritten as

$$R = A(2^{\Delta T})^{\alpha} 2^{\alpha(\bar{T}-T_0)} \tag{9-74}$$

where $\bar{T}$ is a mean temperature and ΔT is the offset from the mean. Only the component with the ΔT need be calculated using realizations.

With a base case having standard deviations of 3.62 and 4 for daily mean deviation and daily range, respectively, $f = 2^{\alpha\Delta T}$ is about 1.5. Halving σ for the range drops f to 1.4, while doubling raises f to 1.9. Halving σ for the daily deviation drops f to 1.15, while doubling raises f to between 3 and 5. The correlation coefficient has no effect. As a practical matter, using 1.5 should be fine, particularly since A is a calibration coefficient anyway. One would expect that the variability would only decrease under wetter or cooler climates, since relative humidity should be larger and thereby buffer the temperature swings.

3/4/99 Annual freeze-thaw. SAS

I wrote a *Matlab* routine called make_FT_table to drive the calculations of the freeze-thaw cycle as a function of the mean daily temperature. The base case uses the standard deviations and correlation for Beatty. A table is written out with the resulting fraction of the time a day with given mean temperature has a maximum greater than 0 degree C and a minimum less than 0 degree C, based on 10^6 realizations. The mean temperature is varied by 0.5 degree steps.

Another routine, test_get_annual_FT, plots the number of freeze-thaw cycles for various values of MAT and at various depths within the soil. It is assumed that the decay of the temperature amplitude with depth can be applied to the standard deviations for daily temperature range and daily-mean deviation. Thus, both standard deviations are multiplied by $\exp(-z/D)$, where z is depth below the soil surface, $D = (2k_h/\omega C_h)^{1/2}$, and $\omega = 2\pi/24$ (representing a daily cycle). For typical soils, D for daily perturbations might be about 15 cm. The resulting combination is implemented by scaling the mean temperatures corresponding to a given fraction, so that interpolation occurs using a table with entries based on $T\exp(-z/D)$. Typically an offset is needed in the scaling, but since freezing is based on 0 degree C the offset is zero.

Typical cases are shown in Figure 9-4, using the standard deviations, correlation coefficient, amplitudes, and offsets determined using the Beatty data set. Only MAT and depth are varied. Note the peaks in Figure 9-4 correspond to the cases where the peak of either summer or winter has an expected temperature of 0 degree C. The decay of the amplitude of the annual cycle with depth is also considered, tending to bring the peaks towards 0 degree C. Also note that freeze-thaw cycles are rare and shallow (less than 10 cm) with a ground-surface MAT corresponding to the atmospheric MAT at YM (17.2 degree C). If soil temperatures were 5 degree C cooler, however, there might be an annual average of 15 freeze-thaw cycles at the ground surface and several cycles even 50 cm deep within the soil profile.

For both north- and south-facing slopes, soil temperatures are higher than air temperatures; north-facing slopes are a few degrees warmer than air temperatures and south-facing slopes are at least four degrees warmer still. Even under glacial conditions it may be that south-facing YM slopes see minimal freeze-thaw activity.

The number of freeze-thaw cycles are only part of the story for weathering; moisture must also be available for weathering to occur. The appropriate assumption on moisture availability has yet to be confirmed. Options include: (i) the amount of moisture required is so minimal that it can always be assumed to be present, (ii) freeze-thaw has no effect unless at least 15 bar of suction

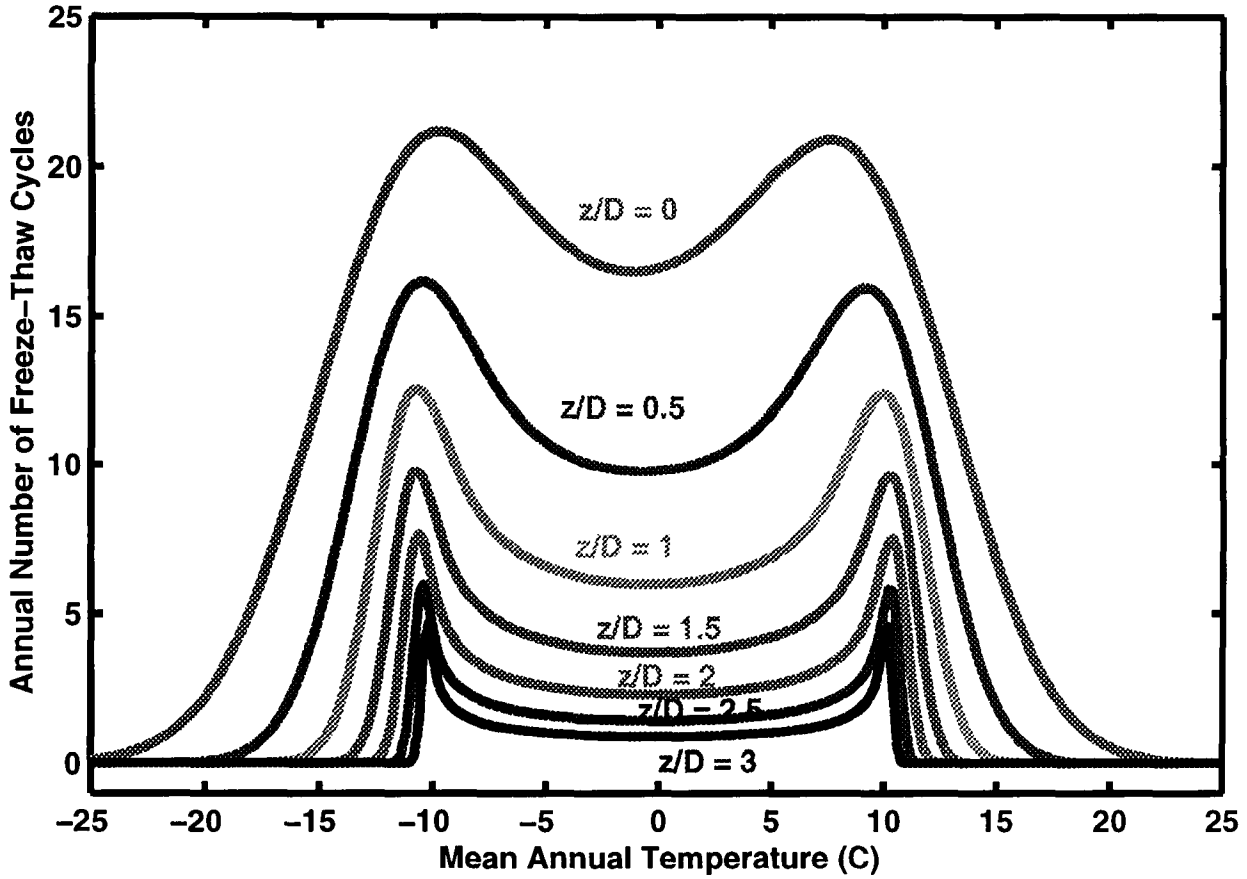

Figure 9-4: 3/4/99. Number of freeze-thaw cycles per year for various normalized soil depths and mean annual temperatures, using temperature statistics based on Beatty observations between 1948 and 1994. The z/D parameter is depth within the soil divided by a diffusion parameter (on the order of 15 cm for typical soils).

exists, or (iii) some drier condition marks the activity threshold.

3/5/99 Probability of moisture above a threshold. SAS

Quantifying the number of freeze-thaw cycles is the most straightforward component of the weathering problem, and the above work should be sufficient to handle it. The other component of weathering comes from weathering-rind formation.

Quantifying the expected rate of weathering-rind formation has with two subcomponents:

(i) expected rate given moisture above a threshold, and (ii) probability that moisture is above or below the threshold. The first subcomponent has been discussed above, with the conclusion that the annual variation of temperature is probably all that needs to be accounted for (daily fluctuations are likely to cause a multiplier factor that is between 1 and 1.5, much smaller than the uncertainty in the weathering rate under base conditions). The second subcomponent is far more difficult to quantify, although the important simplification of temperature and moisture subcomponent independence is likely justified.

Probably the most satisfying approach for quantifying soil moisture frequency is to simply run several centuries of a model that accounts for precipitation, evapotranspiration, and net infiltration, using the sinusoidal climatic parameters except for precipitation. Precipitation would use appropriate generator statistics. The basic USGS approach of a bucket or cascading-bucket model would be an acceptable starting point, although adaptive vegetation would be highly desirable. Although this approach may be crude for estimating MAI, it may be quite reasonable for estimating the fraction of time that moisture is available above a threshold.

The shallow soils on YM allow the simplifying assumption that the soil column is divided into a dry-soil and an underlying wet-soil bucket lying above the bedrock. Within the wet bucket, saturation and pressure is assumed uniform. The bucket model assumes that the losses due to infiltration into the bedrock are through gravity drainage; the conductivity of the underlying bedrock and fractures can be calculated with the bucket pressure. Gravity drainage rates in the soil place an upper limit on deliveries to the bedrock (in case of fractures).

Evaporation is calculated assuming that the soil in the dry zone is all at equilibrium with the vapor density at the annual average soil temperature. At the interface between the wet and dry zones, vapor density is calculated using the wet-zone pressure and an appropriate temperature. The velocity of the interface is calculated using

$$V_i = \frac{q_v - q_w}{\varepsilon(\theta_v - \theta_w)} \tag{9-75}$$

where V_i is the downward interface velocity, q_v is the downward vapor flux, q_w is the downward liquid flux ($= 0$), ε is porosity, θ_v is liquid saturation in the dry zone, and θ_w is liquid saturation in the wet zone.

Preliminary calculations suggest that the first two days after initial wetting should use time steps on the order of two to four hours; daily or larger time steps are acceptable after the drying zone develops appreciable thickness.

A mass balance is more convenient using soil water mass; however, the transfer function for

change in pressure due to change in water mass is more easily determined by tabulating the mass in the column as a function of the pressure.

3/12/99 Testing code. SAS

I performed a direct comparison of *breath* and the simplified infiltration model for a test case of soil over a fracture. The two models provide very similar results, in terms of total mass in the soil system, after the first 10 or 15 percent of the mass has evaporated. Both have total mass drop off as a power law. The volume of wetted soil is larger for the *breath* simulation, while the saturation of the wetted soil is larger for the simple model.

The discrepancy between the two predictions is due to the ability of the soil to deliver water to the ground surface through both vapor and liquid transport at early times in the *breath* simulations, while as soon as there is any air gap the simple model can only deliver water through the less-efficient mechanism of vapor transport.

Based on this test case, it appears that breaking the bucket into a few saturation contours to describe the drying front would provide a significant improvement in predictions at relatively minimal computational cost, albeit with additional coding effort. This step would also tend to provide a better estimate of wetted volume. I would not use more than a few (e.g., less than 6) saturation contours to describe the drying front. Perhaps they could be placed evenly according to conductivity.

Note, however, that simulations with only evaporation may be expected to have the largest discrepancy between detailed and simple simulations, while transpiration uptake may overwhelm the discrepancies. For example, roughly a quarter of plant-available storage is still available after a year of evaporation from a 50-cm column. I expect that the soil column would be essentially dry by late spring or early summer from a completely saturating winter rain.

One other approach may be fruitful as well. If there is assumed to be a hydrostatic capillary fringe, the equivalent conductance of the fringe can be taken into account. A table can be constructed of conductance for the fringe, with tabulated values corresponding to saturations relative to full saturation. Actual conductance is calculated by differencing.

4/11/99 Summary of meeting. SAS

I presented current and ongoing work at a noontime seminar last week. There was a meeting between Randy Fedors, Oliver Chadwick, David Groeneveld, and myself built around the seminar, at which we fleshed out remaining details in infiltration and soil genesis modeling. David will provide typical ranges of values for transpiration and individual plant descriptions (e.g., growth rates, sizes, shapes). Oliver will provide weathering rates, while looking out for information on roughnesses, dust deposition modeling, and creep. Randy will look into methods for translating soil particle-size distributions into van Genuchten retention parameters, and will ask Mike Miklas if he could look into some of the factors that Oliver is looking out for as well.

The soil genesis model clarified considerably in the discussions. The original model consisted of a particle-size distribution with uniform mineralogy (most importantly, weathering rates). The model now conceptually consists of up to five particle-size distributions: (i) native rock, (ii) fast-weathering, (iii) moderate-weathering, (iv) slow-weathering, and (v) carbonates.

The first distribution arises from bedrock entrainment. Our first inclination is to assume that the predominant weathering process is through mechanical weathering, although there is no particular reason that some type of chemical weathering might also take place. Either bedrock from all units weathers at the same rate or a mixture must be tracked.

The remaining distributions arise from dust deposition. Although in some cases an individual dust particle may be formed from a mixture of minerals (e.g., welded-tuff source rock), the feeling from Randy and Oliver is that assuming single-mineral particles is not unreasonable. Certainly it is much easier to track separate distributions than it is to track particles composed of multiple minerals.

The carbonate class is a special case. Apparently the problem of caliche formation in desert soils has received a good deal of attention over the last 20 years, and neglecting caliche may raise eyebrows. Our observations suggest that caliche generally is not forming in the soil column, except in deeper soils, and rather is associated with soil/bedrock interfaces and bedrock fractures. Our model will likely deposit the carbonates within bedrock fractures, neglecting details of deposition mechanisms. Perhaps some analysis of wetting penetration depths will aid in justifying this assumption.

Quarterly Information

Entries into Scientific NoteBook # 163 for the period November 16, 1995, to April 11, 1999, have been made by Stuart Stothoff (SAS; April 11, 1999).

No original text entered into this Scientific Notebook has been removed (SAS; April 11, 1999).

One other approach may be fruitful as well. If there is assumed to be a hydrostatic capillary fringe, the equivalent conductance of the fringe can be taken into account. A table can be constructed of conductance for the fringe, with tabulated values corresponding to saturations relative to full saturation. Actual conductance is calculated by differencing.

4/11/99 Summary of meeting.

I presented current and ongoing work at a noontime seminar last week. There was a meeting between Randy Fedors, Oliver Chadwick, David Groeneveld, and myself built around the seminar, at which we fleshed out remaining details in infiltration and soil genesis modeling. David will provide typical ranges of values for transpiration and individual plant descriptions (*e.g.*, growth rates, sizes, shapes). Oliver will provide weathering rates, while looking out for information on roughnesses, dust deposition modeling, and creep. Randy will look into methods for translating soil particle-size distributions into van Genuchten retention parameters, and will ask Mike Miklas if he could look into some of the factors that Oliver is looking out for as well.

The soil genesis model clarified considerably in the discussions. The original model consisted of a particle-size distribution with uniform mineralogy (most importantly, weathering rates). The model now conceptually consists of up to five particle-size distributions: (i) native rock, (ii) fast-weathering, (iii) moderate-weathering, (iv) slow-weathering, and (v) carbonates.

The first distribution arises from bedrock entrainment. Our first inclination is to assume that the predominant weathering process is through mechanical weathering, although there is no particular reason that some type of chemical weathering might also take place. Either bedrock from all units weathers at the same rate or a mixture must be tracked.

The remaining distributions arise from dust deposition. Although in some cases an individual dust particle may be formed from a mixture of minerals (*e.g.*, welded-tuff source rock), the feeling from Randy and Oliver is that assuming single-mineral particles is not unreasonable. Certainly it is much easier to track separate distributions than it is to track particles composed of multiple minerals.

The carbonate class is a special case. Apparently the problem of caliche formation in desert soils has received a good deal of attention over the last 20 years, and neglecting caliche may raise eyebrows. Our observations suggest that caliche generally is not forming in the soil column, except in deeper soils, and rather is associated with soil/bedrock interfaces and bedrock fractures. Our model will likely deposit the carbonates within bedrock fractures, neglecting details

of deposition mechanisms. Perhaps some analysis of wetting penetration depths will aid in justifying this assumption.

4/25/99 Updated approach.

The day-to-day programming of soil-genesis algorithms and modules is being documented in a Microsoft Word document with embedded *Matlab* commands and output. The notebook format is available on systems running Windows. The advantage of the notebook format is that the developed modules are documented and tested simultaneously. All of the *Matlab* code accessed by the notebook can be retested at will, enabling verification that code is not broken.

Unfortunately, there is no option for running either WordPerfect or LaTeX notebooks, although it should be possible to write macros for WordPerfect comparable to the macro package in Word. It would be much more difficult to implement such a notebook in LaTeX, unless it was modeled somehow on procedures for creating references.

Updated approaches to modeling soil genesis are being incorporated in the new code. The code will be run either in single-column mode or as a set of 1D columns linked with 2D sweeps at the ground surface. The 1D columns will account for creep, bedrock entrainment, and weathering; the 2D sweeps will account for dust and sediment balances at the ground surface.

The 1D column balances will include all but a top active layer. The sequence of steps will be:

- A bulk mass balance, providing bulk fluxes from column to column. This step does not need to consider texture or weathering.
- A particle mass balance, providing particle fluxes from column to column as well as weathering. The bulk fluxes from the first step will be used with the mass fraction corresponding to each particle bin.

Depending on the constitutive relationships, it may be necessary to iterate.

Bulk mass balance of the column will proceed element by element from bottom of the column to the top. The mass balance equation is

$$\frac{\partial M}{\partial t} + \sum_i Q_i = 0, \tag{9-76}$$

where M is mass in the element and Q_i is the ith flux into and out of the element. The variables in the equation are expanded in a finite-volume sense as

$$M = V\rho \tag{9-77}$$

$$V = Ab \tag{9-78}$$

$$Q = vA_c = vbw \tag{9-79}$$

where V is the volume of the element, A is the plan-view area of the element, A_c is the area of the connection between one element and the next, b is the thickness of the upstream element, w is the width of the connection between one element and the next, ρ is the mass density in the element, and q is the flux from one element to another.

Creeping flux is assumed to be governed by film flow, which is has a parabolic velocity distribution. For a constant-density film on an incline, the mean velocity $\bar{v}$ in an element with bottom and top elevations above bedrock of z_a and z_b, respectively, can be shown to be (adapting Bird et al. (1960))

$$\begin{aligned}\bar{v} &= -\left(\frac{\rho g \nabla z}{6\mu}\right)\left(\frac{z_b^3 - z_a^3}{z_b - z_a}\right) \\ &= -\rho C\left(z_a^2 + z_a z_b + z_b^2\right) \\ &= -\rho C\left(z_a^2 + z_a(z_a + b) + (z_a + b)^2\right) \\ &= -\rho C\left(3z_a^2 + 3z_a b + b^2\right), \end{aligned} \tag{9-80}$$

$$C = \frac{g\nabla z}{6\mu}, \tag{9-81}$$

where g is the acceleration due to gravity, ∇z is the slope, and μ is the soil viscosity. With the assumption that the kinematic approach is valid, columns can be processed from top to bottom by elevation. Thus, fluxes can be classed as either incoming (known) or outgoing (unknown).

Substituting definitions into the mass balance equation yields

$$A[(b\rho)^{n+1} - (b\rho)^n] - \left(\sum Q_{in} - \sum Q_{out}\right)\Delta t = 0, \tag{9-82}$$

where n is the time step level. Assuming that the thickness of the element changes to accommodate mass balance changes, b^{n+1} can be isolated:

$$A(b\rho)^{n+1} + \Delta t\left(\sum (b\rho)^{n+1} w_i C_i\right)(3z_a^2 + 3z_a b + b^2)^{n+1} = A(b\rho)^n + \Delta t \sum Q_{in}, \tag{9-83}$$

yielding a cubic relationship for b^{n+1} even assuming that all else remains constant. It is easy enough to solve iteratively for $(b\rho)^{n+1}$ by rearranging,

$$(b\rho)^{n+1} = \frac{A(b\rho)^n + \Delta t \sum Q_{in}}{A + \Delta t(\sum w_i C_i)(3z_a^2 + 3z_a b + b^2)^{n+1}}, \tag{9-84}$$

where there is a quadratic expression including b^{n+1} in the denominator that forces the iteration. Presumably changes in b will be relatively small during a time step. It is possible to update ρ during the cycle if some reasonable method is found. Note that sources and sinks might be considered an incoming flux (*e.g.*, bedrock fluxes). Of course, if the thickness of the element is held constant, the change in density is calculated instead of the element thickness.

Physically one would expect that a mixing process takes place, so that not only the element thickness but the element density adjust over a time step. A mixing mass balance equation for density can be written

$$\frac{\partial \rho M}{\partial t} + \sum_i \rho_i Q_i = 0, \tag{9-85}$$

which, following the same steps, results in

$$A[(b\rho^2)^{n+1} - (b\rho^2)^n] - \left(\sum \rho_{in} Q_{in} - \rho \sum Q_{out}\right) \Delta t = 0, \tag{9-86}$$

and finally

$$(b\rho^2)^{n+1} = \frac{A(b\rho^2)^n + \Delta t \sum \rho_{in} Q_{in}}{A + \Delta t (\sum w_i C_i)(3z_a^2 + 3z_a b + b^2)^{n+1}}. \tag{9-87}$$

These two equations can be used to update $b\rho$ and $b\rho^2$. Simplifying the equations,

$$b\rho = \beta_1 \tag{9-88}$$

$$b\rho^2 = \beta_2 \tag{9-89}$$

yields solutions of

$$b = \frac{\beta_1^2}{\beta_2} \tag{9-90}$$

$$\rho = \frac{\beta_2}{\beta_1} \tag{9-91}$$

These still need iteration, due to the quadratic term with b. A simple test suggests that 5 iterations may be sufficient if the Courant number is less than 1 (incoming mass is less than the initial mass in the cell).

Once the bulk fluxes are obtained, then texture can be considered. The particle mass balance equation for a particle class is

$$\frac{\partial \omega M}{\partial t} - \sum \omega_{in} Q_{in} + \sum \omega Q_{out} - \sum_j S_j + \lambda \omega M = 0, \tag{9-92}$$

where ω is mass fraction, S is the particle mass created by weathering larger particles, and λ is the rate of loss of particle mass to smaller particles. Again external sources/sinks are treated as fluxes. Note that adding all of the particle mass balance equations together yields the bulk mass balance equation. Rearranging yields

$$(\omega M)^{n+1} + \Delta t \omega^{n+1} \left(\sum Q_{out} + \lambda M \right)^{n+1} = (\omega M)^n + \Delta t \left(\sum \omega_{in} Q_{in} + \sum_j S_j \right), \tag{9-93}$$

and finally the explicit relationship

$$\omega^{n+1} = \frac{(\omega M)^n + \Delta t \left(\sum \omega_{in} Q_{in} + \sum_j S_j \right)}{M^{n+1}(1 + \Delta t \lambda) + \Delta t \sum Q_{out}}. \tag{9-94}$$

It is best to not use the particle balance equation for one particle class, because the bulk equation has been used. Instead, it is better to subtract the mass in all particle classes from the total mass, thereby ensuring overall mass balance. Probably one of the clay bins would be a good candidate (maybe the fastest-weathering category).

4/27/99 Dispersion.

Preliminary tests of bulk mass balance in a 1D column seem to work pretty well. In the testing, I realized that the density balance calculation does not require iteration, as β_2/β_1 is completely known (the nonlinear denominator of both β_1 and β_2 is the same and cancels in the ratio, and the numerators are completely known *a priori*).

Vertical movement of particles must occur within a soil column: witness desert pavement, for example, where larger fragments float to the ground surface. Also, Oliver emphasized that a debris flow fully mixes the profile. These phenomena have not been included in our model to date, and I've been worried about how to do so. Today two approaches occurred to me that might help.

The mixing process due to creep and bulk flow is dispersive. In the porous-media transport literature, the dispersion coefficient is related to velocity. A similar relationship can be applied here, where vertical dispersion is due to slope-parallel fluxes. Such a relationship can be simply written in the form

$$D = \alpha V, \tag{9-95}$$

where D is the dispersion coefficient used for particle transport, α is dispersivity, and V is velocity. The velocity might be a flux-weighted average of all velocities in connections to a column. The

dispersion coefficient will increase from the bottom of the column to the top, consistent with the parabolic velocity profile.

It occurs to me that the dispersivity should be proportional to the standard deviation of the particle-size distribution, and should be related to the nonuniformity of the larger particles. The reasoning is that an extremely uniform distribution with extremely spherical particles may move quite laminarly. Mixing should be enhanced by a wider particle-size distribution; just imagine the effect on smaller particles of rolling a cobble along. If the cobble is highly irregular, mixing should be even more enhanced.

The flotation process should also be enhanced by a wide distribution of particle sizes. Flotation occurs when the smaller grains are able to work their way under the larger particles, thereby switching elevations. If there is a narrow distribution, there is nothing to float. Flotation is enhanced by anything that causes grain movement, such as thermal expansion and vibrations. All of the movement-inducing processes active without bulk motion are dampened with depth below the surface.

One way to characterize the flotation process is by a body force on the particles. I imagine this force might have the form

$$f(z,r) = (a_1 \exp[(z - z_s)/D_z] + a_2 V_h) \left(\frac{r^2 - r_m^2}{r_m^2} \right), \tag{9-96}$$

where z is elevation, z_s is ground-surface elevation, r is particle radius, r_m is the mean particle radius, D_z is a damping depth (the diurnal thermal depth should be good), V_h is the horizontal velocity used to calculate dispersion, and a_1 and a_2 are scaling coefficients. The term with r yields an upward force for large particles and a downward force for small particles. I presume that the cross-sectional area of the particle should provide the proportionality, since force is pressure divided by area. The rationale for the exponential term is that surface-induced perturbations are exponentially dampened (such as thermal and pressure perturbations). The rationale for the velocity term is that bulk movement provides opportunity for particles to redistribute. Both terms decay with depth below ground surface.

4/29/99 More dispersion.

After further thought, the flotation flux should have the form

$$q(z,r) = (a_1 \exp[(z - z_s)/D_z] + a_2 V_h)(\pi \mathbf{g})(\langle \rho r^2 \rangle - \rho r^2) \tag{9-97}$$

$$\langle \rho r^2 \rangle = \frac{\sum_{i,j} \rho_{ij} r_{ij}^2 \omega_{ij}}{\sum_{i,j} \omega_{ij}} = \sum_{i,j} \rho_{ij} r_{ij}^2 \omega_{ij} \tag{9-98}$$

The summation is over the number of particle classes and bins. As before, the net flux is zero, but it also is dependent on particle density (both larger and lighter particles float better). Note that the gravity vector $\mathbf{g}$ points down and $\sum \omega = 1$.

A nice feature of the formulation is that net flux is inherently zero. However, a problem with this formulation is that all bins of all textures simultaneously participate in the summation. Aside from the flotation flux, the individual textures can be independently treated; each bin can be independently treated to boot (particle breakup cascades from larger to smaller particles). If not for dispersion, each element within a column could also be independently treated.

The overall particle balance equation for particle class k, with the newer thoughts, becomes

$$\frac{\partial M \omega_k}{\partial t} - \sum \omega_{in} Q_{in} + \sum \omega_k Q_{out} + M \omega_k \lambda_k - \sum_j \lambda_j \Xi_{jk} M_j \omega_j - \sum_m D_m \nabla_m \omega_k + \sum Q_{float} - \sum Source = 0 \tag{9-99}$$

where λ is the decay rate from weathering, Ξ is the distribution function for weathering products into bins, *Source* represents external sources/sinks (positive for sources), Q_{float} represents flotation fluxes, and the remainder are defined above.

Rigorous treatment of flotation generates a block-tridiagonal matrix if all textures are grouped by element. This structure is as compact as can be achieved. With the organization of the coefficient matrix by element at the coarsest level, the maximum width of active columns is $3 \times N_{\text{class}} \times N_{\text{bin}}$, where N_{class} is the number of particle classes and N_{bin} is the number of bins per particle class. For example, with 7 classes and 37 bins, the active width is 777. The dimension of the matrix is the active width times the number of elements.

The (reasonable) example might take a significant fraction of a minute to solve, which is much too slow for practical purposes. Replacing the direct solution with an iterative procedure, lagging the flotation component, reduces the coefficient matrix to a series of tridiagonals, one for each bin of each particle class. The example would produce 777 short tridiagonal matrices. The

flotation fluxes should be relatively small and consistent from beginning to end of a time step, so that iteration should be fast.

A rough estimate of solution effort for a banded matrix is NB^2. A tridiagonal matrix solves linearly with dimension. If N_t is the total number of particle-class bins, and N_e is the number of elements, an iterative step would take effort proportional to $N_t \times N_e$. The block-tridiagonal matrix would take effort proportional to $N_e \times N_t \times (N_t/2)^2$, simplifying to $N_e N_t^3$. Since N_e is generally going to be negligible compared to N_t, effort is approximately cubed for the block-tridiagonal relative to the multiple tridiagonal. This should mean a solution in several seconds rather than a minute for the example.

I would expect that it would be faster in *Matlab* to assemble and solve a triangular matrix than it would be to loop through the equivalent sequence directly, since the solution is hard-coded while looping is relatively inefficient. This matrix corresponds to the case with one element (no flotation). It is not clear whether a block-tridiagonal sequence with triangular blocks would be faster than looping over a sequence of tridiagonal matrices.

5/3/99 Timings.

A rough estimate of time required to perform various *Matlab* activities suggests that solving a lower-triangular system of equations (corresponding to the solution of a pure-advection system with weathering breakdown) is extremely fast if sparse storage is used. For example, a lower-triangular matrix of dimension 2000 takes about 7×10^{-4} sec. A symmetric tridiagonal matrix of the same dimension takes about 3.6×10^{-2} sec, while an unsymmetric tridiagonal matrix takes about 1.3 sec. A more typical size might be of dimension 800, yielding times of 2.8×10^{-4} sec, 1.4×10^{-2} sec, and 0.21 sec, respectively.

A block-tridiagonal matrix, with blocks of dimension 250, takes about 9 sec, while a block-tridiagonal matrix with lower triangular blocks takes about 2.4 sec.

The *Matlab* solvers have quirks. A matrix of dimension 1000 consisting of a lower triangular matrix with one additional diagonal just above the main diagonal takes 5.5 sec to solve if it is stored in sparse format, while it only takes 0.77 sec to solve if it is stored in full format. On the other hand, a lower triangular matrix of the same dimension uses 0.16 sec in full format and 3.3×10^{-4} sec in sparse format. There must be overhead involved in both formats, with additional checking in full format and indirect addressing in sparse format.

Correction dated 5/7/99: Matlab *support explained that the slowness of the sparse triangular matrix solution is due to a step that attempts to reorder the matrix to minimize fill-in (not necessary for my problem). They offer a procedure to turn on and off this reordering at will. The* Matlab *command spparms('autommd',0) turns off reordering and spparms('autommd',1) turns it back on. I would expect that my applications would not benefit significantly from reordering, since I am careful in maintaining matrix structure.* SAS

The form of the discretized full particle balance equation is

$$a_1\omega_i^{n+1} + \sum \omega_i^{n+1} q_{out} + \omega_i^{n+1}\lambda_i - \sum \omega_j^{n+1}\Xi_{ji} - \sum D\nabla_z\omega_i + \sum \omega_i q_{flot} = a_2\omega_i^n + \sum \omega_{in} q_{in} + \sum Source \tag{9-100}$$

Neglecting weathering (the λ and Ξ terms), dispersion (the D term), and flotation (the q_{flot} term) results in an explicit calculation. Adding just weathering yields a triangular matrix. Adding just dispersion yields a symmetric tridiagonal matrix. Adding just flotation yields a linear unsymmetric full matrix, or a nonlinear unsymmetric tridiagonal matrix.

The only hope for competitively fast solutions arises from using the triangular matrix with iteration to handle dispersion and flotation. Note that 50 solutions of the triangular matrix can occur in the same time that the equivalent symmetric tridiagonal can be solved (1850 solutions relative to the equivalent unsymmetric tridiagonal). Flotation clearly must be handled using iteration, while dispersion probably should as well (note that iteration will require reassembly of the right-hand side vector, so that matrix solution is not the only factor to be considered).

5/5/99 More timings and tests.

SAS

I finally got the bulk transport and differential transport modules working (without dispersive processes) and tested. I made up a nine-cell problem for which I could change the number of texture classes and the number of vertical elements. I tested two cases to examine mass balance: pure weathering (no sources) and pure transport (no weathering). Both cases identified bugs, but each one now has mass balance to within roundoff error (at least 14 decimal places), even with several elements, several texture classes, and numerous bins for each class.

Timings on the test problem suggest that 90 to 95 percent of the computational effort is in the beta transformation used to create the bins. This is the case with weathering but not vertical dispersion. The issues regarding matrix solution may be less important than I thought before, although a quick test is still in order. Overall time for a cell with 36 bins, 4 elements, and 2

textures is on the order of 4 seconds, of which at least 3.6 seconds go to the beta distributions. This gives 15 cells per minute; adding textures would reduce this. It appears that only hillslope simulations may be practical unless very coarse discretizations of the particle distribution are used. A factor of 10 speedup would result from not going through the statistical distribution, although memory would be a big problem. Probably 10^3 mass fractions per cell. Maybe for a problem with less than 10^3 cells (30×30), like a hillslope.

5/7/99 Revisions.

I've revised the coding to provide the option for carrying either a statistical representation (memory saving) or bin representation (memory intensive but faster and more accurate) for the particle-size distribution of each element. Inefficiency in the original coding was improved upon as well. As a comparison of relative speed, I have a problem with 2 texture components, 37 bins per texture, and 4 elements per column. The original coding with statistical representation ran one step of this problem 10 times in 37.6 sec, for an average of 3.76 sec/step (excluding setup costs). The updated coding ran one step of the same problem 100 times in 7.74 sec, for an average of 0.0774 sec/step (almost 50 times faster).

The updated code ran the statistical representation 10 times in 16.8 sec, for an average of 1.68 sec/step (2.2 times faster). Most of the speedup was accomplished by moving the evaluation of the breakdown transition matrix to a preprocessing step, halving the number of beta-distribution calls per time step. The remaining small speedup was likely gained by using global arrays rather than passing arguments.

In a mode with one element and four textures per column, and grain-size distribution characterized with 19 bins, representing a minimum resolution that might be used, one time step is roughly 0.0559 sec. This corresponds to about 1070 cells per minute. Converting the *Matlab* particle-update routine to a compiled version using the builtin *Matlab* converter realized a further speedup to a time step of 0.0395 sec, probably due to reduced looping overhead. Converting both the particle-update and the bulk flux driver routines resulted in a speed of 0.0367 sec/step, or about 1640 step/min (about 1.5 times faster). With 37 bins, the average rate is 0.597 sec/step (1.6 times slower); with 10 bins, 0.0375 sec/step (essentially the same).

The fastest rate would correspond to solving a 40×40 grid each minute for the subsurface particle transport. Note that additional processing (*e.g.*, sorting) would slow this down, and additional work is necessary for surface transport and sources. For comparison, the finest Split Wash

grid (1.875 m on a grid-block side) is 417×737 blocks for a total of 307,329 grid blocks; this would mean each time step takes more than 3 hours. Even though perhaps half of the grid blocks are not strictly necessary, a transient Split Wash simulation is still ambitious. A hillslope cross section at the same resolution would be only 200 blocks, so that several time steps could be accomplished per minute (much more practical).

5/8/99 Constitutive relationships.

Summarizing from previous entries, the sediment mass balance, for any particular particle size, is

$$\sum S_{in} q_{in} - S \sum q_{out} + (W/L) c_e (S - S_{eq}) = 0, \tag{9-101}$$

$$S_{eq} = C_s \frac{v^4}{h}, \tag{9-102}$$

$$c_e = \begin{cases} \frac{v_s}{h}\left(1 - \frac{S_{eq}}{S}\right) & \text{for deposition} \\ C_{scour} & \text{for detachment} \end{cases} \tag{9-103}$$

where

- S is sediment concentration [M/L^3],
- S_{eq} is equilibrium sediment concentration [M/L^3],
- q is volumetric water flux [L^3/T],
- v is water velocity [L/T],
- v_s is particle settling velocity [L/T],
- C_s is a coefficient [M T^4/L^6],
- C_{scour} is a coefficient describing detachment [1/T],
- q is volumetric water flux [L^3/T],
- W/L is travel width/travel length [–], and
- c_e is the kinetic exchange coefficient [–].

There are one-to-one relationships between velocity, flux, flow depth, and equilibrium sediment concentration, so that all can be calculated given one. Unfortunately, c_e is dependent on whether deposition or detachment is occurring.

The WEPP documentation (Flanagan and Nearing, 1995) has a similar but more complete approach to predicting erosion and detachment. In particular, detachment is much more physically based, considering shear stress and the effects of roughness. The WEPP approach partitions the system into rills (1D features) and delivery from interrill areas. Interrill areas are not explicitly treated, other than in the 1D features. Sediment transport is assumed steady state, with overland

flow assumed to occur at the peak rate for the length of time that produces the same total flux over the storm (*i.e.*, a equal-volume steady pulse).

The WEPP rill equation is

$$\frac{\partial G}{\partial x} = D_f + D_i \tag{9-104}$$

$$D_f = \begin{cases} \left(\frac{K_r}{T_c}\right)(\tau_f - \tau_c)(T_c - G) & \text{for detachment} \\ \left(\frac{\beta V_f}{q}\right)(T_c - G) & \text{for deposition} \\ D_i & = K_{iadj} I_e \sigma_{ir} SDR_{RR} \left(\frac{R_s}{w}\right) \end{cases} \tag{9-105}$$

where

G is sediment load [M/LT],
D_f is rill erosion rate [M/L^{2}T],
D_i is interrill sediment delivery rate [M/L^{2}T],
x is distance downstream [L],
K_r is a rill erodibility parameter [T/L],
τ_f is flow shear stress acting on the soil [M/LT^2],
τ_c is the critical flow shear stress for detachment [M/LT^2],
T_c is sediment transport capacity [M/LT],
β is a raindrop-induced turbulence coefficient (0.5 if raining, 1 if not) [–],
V_f is effective fall velocity for the sediment [L/T],
q is flow discharge per unit width [L^{2}T],
K_{iadj} is adjusted interrill erodibility [–],
I_e is effective rainfall intensity [L/T],
σ_{ir} is the interrill runoff rate [L/T],
R_s is the rill spacing [L], and
w is the rill width [L].

In order to translate the WEPP equation into the sediment concentration form, the following correspondences hold:

$$G = Svw \tag{9-106}$$

$$T_c = S_{eq} vw \tag{9-107}$$

$$q = vw \tag{9-108}$$

Substituting into the WEPP and neglecting interrill delivery yields

$$\frac{\partial Svw}{\partial x} = \begin{cases} \left(\frac{K_r}{S_{eq}vw}\right)(\tau_f - \tau_c)(S_{eq} - S)vw & \text{for detachment} \\ \left(\frac{\beta V_f}{vw}\right)(S_{eq} - S)vw & \text{for deposition} \end{cases} \tag{9-109}$$

Simplifying yields

$$\frac{\partial Svw}{\partial x} = \begin{cases} \left(\frac{K_r}{S_{eq}}\right)(\tau_f - \tau_c)(S_{eq} - S) & \text{for detachment} \\ \beta V_f(S_{eq} - S) & \text{for deposition} \end{cases} \tag{9-110}$$

This can be written in the form

$$\sum(Sv) + \frac{L}{w}c_e(S - S_{eq}) = 0 \tag{9-111}$$

where c_e is extracted from the above relationships. The form in the WEPP documentation is the same as I used before, except for the length/width ratio. I think my previous documentation is in error, but the coding should be correct.

WEPP calculates the shear stress at the end of a segment, τ_{fe}, and the transport capacity as

$$\tau_{fe} = \gamma R \sin(\alpha)\left(\frac{f_s}{f_t}\right) \tag{9-112}$$

$$T_c = k_t \tau_f^{3/2} \tag{9-113}$$

where

- γ is the specific weight of water [M/L^{2}T^2],
- R is the hydraulic radius [L],
- α is the average slope angle [–],
- f_s is the friction factor for the soil [–],
- f_t is the total friction factor [–], and
- k_t is a transport coefficient [L$^{0.5}$ T^2/M$^{0.5}$].

In the WEPP documentation, regression relationships are given for K_r and τ_c for rangeland and cropland. The rangeland rill relationships, based on 18 rangeland soils, are

$$K_r = 0.0017 + 0.0024clay - 0.0088orgmat - \frac{0.00088\rho_d}{1000} - 0.00048ROOT_{10} \tag{9-114}$$

$$\tau_c = 3.23 - 5.6sand - 24.4orgmat + \frac{0.9\rho_d}{1000} \tag{9-115}$$

where

K_r has dimensions of [s/m],

τ_c has dimensions of [Pa],

$clay$ is the fraction of clay in the surface soil (0.033 to 0.422),

$sand$ is the fraction of sand in the surface soil (0.08 to 0.88),

$orgmat$ is the fraction of organic material in the surface soil (0.005 to 0.112),

ρ_d is the bulk density (1200 to 1800 kg/m^3), and

$ROOT_{10}$ is the total root mass in the top 10 cm of the soil (0.02 to 4.10 kg/m^2).

Adjustments in WEPP to the K_r and τ_c rill relationships are

$$K_{radj} = K_{rb} CK_{rbr} CK_{rdr} CK_{rlr} CK_{rsc} CK_{rft} \tag{9-116}$$

$$CK_{rbr} = \exp(-0.4br) \tag{9-117}$$

$$CK_{rdr} = \exp(-2.2dr) \tag{9-118}$$

$$CK_{rlr} = \exp(-3.5lr) \tag{9-119}$$

$$CK_{rsc} = \frac{K_{rcons}}{K_r} + \left(1 - \frac{K_{rcons}}{K_r}\right) \exp(-\rho_d daydis) \tag{9-120}$$

$$K_{rcons} = 0.00035 - 0.0014\theta_{cf} + 0.00068silt + 0.0049M_{cf} \tag{9-121}$$

$$CK_{rft} = 2.0(0.933)^{\Psi_{surf}} \tag{9-122}$$

$$\tau_{cadj} = \tau_{cb} C\tau_{rr} C\tau_{cons} C\tau_{sc} C\tau_{ft} \tag{9-123}$$

$$C\tau_{rr} = 1 + 8(RR_t - 0.006) \tag{9-124}$$

$$C\tau_{sc} = \frac{\tau_{rcons}}{\tau_r} + \left(1 - \frac{\tau_{rcons}}{\tau_r}\right) \exp(-\rho_d daydis) \tag{9-125}$$

$$\tau_{cons} = 8.37 - 11.8\theta_{fc} - 4.9sand \tag{9-126}$$

$$C\tau_{ft} = 0.875 + 0.0543 \ln(Psi_{surf}) \tag{9-127}$$

where

K_{radj} is the adjusted value of K_r,
CK_{rbr} is the rill erodibility adjustment,
CK_{rdr} is the dead root adjustment,
CK_{rlr} is the live root adjustment,
CK_{rsc} is the sealing and crusting adjustment,
br is the mass of buried residue in the top 15 cm [kg/m^2],
dr is the mass of dead roots in the top 15 cm [kg/m^2],
lr is the mass of live roots in the top 15 cm [kg/m^2],
$daydis$ is the number of days since disturbance [day],
θ_{cf} is the volumetric water content at field capacity (1/3 bar) [m^3/m^3],
$silt$ is the fraction of silt in the surface soil [–],
RR_t is the random roughness of the surface soil [mm]

The adjustments for sealing and crusting are only made for cropland.

The interrill delivery rate, D_i, is

$$D_i = K_{iadj} I_e Q_r \tag{9-128}$$

where

K_{iadj} is the adjusted value of interrill erodibility [kg s/m^4],
I_e is the rainfall intensity [L/T],
Q_r is the runoff rate [L/T],

The relationships in WEPP for rangeland interrill erodibility are

$$K_{iadj} = K_{ib} RK_{icov} RK_{ift} \tag{9-129}$$

$$K_{ib} = 1.81 - 1.91 sand - 6.327 orgmat - 0.846\theta_{fc} \tag{9-130}$$

$$RK_{icov} = \exp[-7.0(inrcov + cancov) \tag{9-131}$$

$$RK_{ift} = CK_{ift} \tag{9-132}$$

where

K_{ib} is the base value of interrill erodibility [kg s/m^4],
RK_{icov} is the adjustment for cover [–],
$inrcov$ is the interrill cover [0 to 1],
$cancov$ is the canopy cover [0 to 1].

5/9/99 Proposed revisions to constitutive theory.

These descriptions are somewhat unsatisfactory. There is always a deposition component, although it may be overcome by the detachment component. Partitioning c_e into either a deposition or a detachment mode loses this physical behavior. I would prefer to see something like the evaporation relationships in boundary layer theory, with a far-field concentration and a surface concentration based on the shear stress available for lifting particles.

Stress at the ground surface arising from fluid flow should be partitioned among all of the surface elements. I would expect that stress on a particular surface element (*e.g.*, a particular grain size) would be proportional to the exposed grain surface area relative to the total exposed surface area. This can be written

$$\tau_i = \tau_t \frac{SA_i}{\sum_j SA_j} \tag{9-133}$$

where τ_i is the stress over all surface elements of class i, τ_t is the total surface stress, SA represents the total exposed surface area, and the summation on the right-hand side is over all surface elements. Comparison of the stress relative to a critical stress for each surface element provides information on rates of detachment.

A development by Bird et al. (1960) suggests that the fall velocity, v_∞ of a particle in turbulent conditions is

$$v_\infty^2 = \frac{8gR}{3f}\left(\frac{\rho_s - \rho_f}{\rho_f}\right) \tag{9-134}$$

$$Re = \frac{2Rv_\infty\rho_f}{\mu} \tag{9-135}$$

$$f = \begin{cases} \frac{24}{Re} & Re < 2 \\ \frac{18.5}{Re^{3/5}} & 2 < Re < 500 \\ 0.44 & 500 < Re < 2 \times 10^5 \end{cases} \tag{9-136}$$

where

- g is the acceleration due to gravity [L/T^2],
- R is the particle radius [L],
- ρ_s is the sphere density [M/L^3],
- ρ_f is the fluid density [M/L^3], and
- μ is the fluid viscosity [M/LT].

A more recent analysis suggests that the friction factor should be

$$f = \frac{24}{Re} + 1.5 \tag{9-137}$$

for natural sands and gravels (Julien, 1995).

The same analysis might be adapted to calculate the forces on the particles given a fluid velocity. Such an analysis has been done by ?) for particles in rivers, balancing stresses with gravity and incorporating a statistical distribution of angles.

5/10/99 Incorporating time-variable overland flow.

The approach for incorporating sediment transport in time-variable overland flow relies on steady-state sediment transport in time-averaged storms. The WEPP approach also uses steady-state transport for each storm, but here the mixture of storms is performed differently. The idea here is to run a sequence of storms representative of the natural distribution, accumulating the cumulative distribution of flow within each cell.

The cumulative distribution is broken into N bins for each cell. An equivalent set of storm fluxes arises from the N bins, in the form

$$\sum_i \left[\sum_j (S_{ij} f_{ij} v_{ij}) + \frac{L}{w} f_i c_{ei} (S_i - S_{eqi}) \right] = 0 \tag{9-138}$$

where the i subscript represents a storm bin and f_i is the fraction of time that storm bin i is active. A subtlety of this approach is that f may not be the same for incoming and outgoing fluxes at a particular cell, meaning that there need not be continuity of water fluxes if there are losses due to infiltration or evaporation. Typically f would be lower for outgoing fluxes, which would yield additional deposition.

The coefficients used in the time-averaged storms should be appropriately time weighted as well. A particular flux may occur at any time of year, but may be more likely in some season. The coefficients should reflect this preferentiality.

In order to properly accumulate the storm statistics, I envision running numerous storms with numerous initial characteristics. Note that each storm should be quite fast to run (minutes or less). Some type of response surface could be built up, specific to the specific watershed. The factors in the response surface might include peak flow and the equivalent length of time for that flow. The factors that might be considered include:

- Initial moisture content
- Cover and canopy cover
- Surface soil texture
- Masses of live and dead roots and buried residue
- Random surface roughness
- Friction factors

Thus, each rainfall event might be rerun numerous times, although probably only a relatively few numbers of rainfall events would be necessary.

References

Ackers, P. and W. R. White. 1973. Sediment Transport: New Approach and Analysis. *Journal of the Hydraulics Division, American Society of Civil Engineers 99*(HY11), 2041–2060.

Beaumont, C., P. Fullsack, and J. Hamilton. 1992. Erosional control of active compressional orogens. In K. R. McClay (Ed.), *Thrust Tectonics*, London, pp. 1–18. Chapman & Hall.

Bird, R. B., W. E. Stewart, and E. N. Lightfoot. 1960. *Transport Phenomena.* New York, NY: John Wiley & Sons.

Campbell, G. S. 1977. *An Introduction to Environmental Biophysics.* New York: Springer-Verlag.

Fair, G. M. and J. C. Geyer. 1954. *Water Supply and Wastewater Disposal.* New York, NY: John Wiley & Sons.

Fernandez, J. A., J. B. Case, C. A. Givens, and B. C. Carney. 1994. *A Strategy to Seal Exploratory Boreholes in Unsaturated Tuff.* SAND93-1184, Sandia National Laboratories, Albuquerque, NM.

Flanagan, D. C. and M. A. Nearing. 1995. *USDA - Water Erosion Prediction Project Hillslope Profile and Watershed Model Documentation.* NSERL Report No. 10, United States Department of Agriculture, Agricultural Research Service, West Lafayette, IN.

Julien, P. Y. 1995. *Erosion and Sedimentation.* Cambridge, England: Cambridge University Press.

Kilinc, M. and E. V. Richardson. 1973. *Mechanics of Soil Erosion From Overland Flow Generated by Simulated Rainfall.* Hydrology Paper 63, Colorado State University, Fort Collins, CO.

Meyer, L. D. and W. H. Wischmeier. 1969. Mathematical Simulation of the Process of Soil Erosion by Water. *Transactions of the American Society of Agricultural Engineers 12*(6), 754–762.

Scott, R. B. and J. Bonk. 1984. *Preliminary Geologic Map (1:12,000 scale) of Yucca Mountain, Nye County, Nevada, with Geologic Cross Sections.* Open-File Report 84-494, United States Geological Survey, Denver, CO.

Stothoff, S. A. and A. C. Bagtzoglou. 1996. Subregional Hydrogeologic Flow and Transport Processes. In B. Sagar (Ed.), *NRC High-Level Radioactive Waste Research at CNWRA, July–December 1995*, Volume CNWRA 95-02S, San Antonio, TX, pp. 9–1–9–20. Center for Nuclear Waste Regulatory Analyses.

Woolhiser, D. A., R. E. Smith, and D. C. Goodrich. 1990. *KINEROS, A Kinematic Runoff and Erosion Model: Documentation and User Manual.* ARS-77, United States Department of Agriculture, Agricultural Research Service.

Yalin, Y. S. 1963. An Expression for Bed-Load Transportation. *Journal of the Hydraulics Division, American Society of Civil Engineers 89*(HY3), 221–250.

Yang, C. T. 1973. Incipient Motion and Sediment Transport. *Journal of the Hydraulics Division, American Society of Civil Engineers 99*(HY10), 1679–1704.

Quarterly Information

Entries into Scientific NoteBook # 163 for the period November 16, 1995, to July 2, 1999, have been made by Stuart Stothoff (SAS; July 2, 1999).

No original text entered into this Scientific Notebook has been removed (SAS; July 2, 1999).

SCIENTIFIC NOTEBOOK

by

Stuart A. Stothoff

Southwest Research Institute
Center for Nuclear Waste Regulatory Analyses
San Antonio, Texas

October 1, 1999

Initial Entries

Scientific NoteBook: # 163

Issued to: S. A. Stothoff

Issue Date: Tuesday, November 16, 1993

By agreement with the CNWRA QA this NoteBook is to be printed at approximate quarterly intervals. This computerized Scientific NoteBook is intended to address the criteria of CNWRA QAP-001.

Table 0-1: Computing Equipment

Machine Name	Type	OS	Location	Current
dimension	Dell Dimension	Windows 98	desk	yes
inspiron	Dell Inspiron	Windows 98	desk	yes
latitude	Dell Latitude	Windows 95	desk	yes
sierra.cnwra.swri.edu	Sun SPARC 20	Solaris	desk	yes
sisyphus.cnwra.swri.edu	Sun SPARC 20	SUNOS 4.1.3_U1	network	no
dopey.cnwra.swri.edu	Sun SPARC 10	SUNOS 4.1.3_U1	network	no
performer.cnwra.swri.edu	SGI Onyx	IRIX 5.3	network	no
yosemite.cnwra.swri.edu	SGI Onyx	IRIX 5.3	network	no
bemore.cnwra.swri.edu	SGI Onyx	IRIX 6.2	network	no
redwood.cnwra.swri.edu	SGI Indy	IRIX 6.2	network	no
bigbend.cnwra.swri.edu	Sun Ultra-2	SUNOS 5.5.1	network	no
scratchy1.cnwra.swri.edu	Sun Ultra-2	SUNOS 5.5.1	network	no
hornet.cnwra.swri.edu	Sun Ultra-2	SUNOS 5.5.1	network	no

Contents

List of Figures

List of Tables

fracture fillings needed to be multiplied by the fraction of the cross-sectional area occupied by the fractures. I had not realized that the permeability of the fracture fillings also needs to be adjusted. This misconception should not affect the regression analysis at all, except perhaps the capillary-barrier regression has less of a range in permeability than I originally thought. The capillary-barrier regression should not be materially affected in the unfilled-fracture parameter subspace.

The primary impact of the misconception is on estimates of *MAI*, driving down the estimates. It appears that there may be relatively little impact under present-day climate and soil, but under future soils *MAI* in a soil-fracture system may be drastically smaller. With the revised concept, *MAI* is much more sensitive to the fracture cross-sectional area.

With the corrected method of estimating fracture permeability, I recalculated the areal-average *MAI* over the repository. Otherwise using the same assumptions as was used for the AGU poster last fall, revised repository-average *MAI* was 8.8, 80, and 29 mm/yr for current, early glacial, and late glacial conditions. The corresponding values of *MAI* were 15, 106, and 45 mm/yr before.

Earlier, I had to artificially put the fraction of fractures containing soil to zero in some units because *MAI* in these units was dominated by the small soil-filled fraction. Revising these units to have a small soil-filled fraction had little effect. Only three categories showed appreciable control: unfilled, deep-soil, and bedrock (soil-filled and carbonate-filled fractures had minimal to no incidences of control).

Re-examining the fracture descriptions used by USGS, my feeling is that the caprock and TCmnl units have under-represented fracture area. I suspect that the fractures used by USGS may not represent fractures in outcrops and shallowly covered cases. For example, I think the caprock should have a description with something like 5 to 15 percent fissure area, while the USGS has a description with 9.2 fractures per meter, averaging 250 μm (or 0.23 percent). Similarly, the fracture area of the middle nonlithophysal turns out to be about 0.026 percent; at the surface I think this should be about two orders of magnitude greater. Increasing these units into a more representative area only minimally increases *MAI* (from 8.8 to 9.1 mm/yr) but results in 1/4 of the repository area having fracture control.

9/21/99 Newly obtained meteorologic information.

In order to relate vegetation, soils, climate, and infiltration, several sets of data have been acquired. This entry documents the data and some of the analyses.

The National Weather Service maintains a set of weather stations across the United States. At least two levels of station are maintained. Stations with the widest distribution are called COOP (Cooperative) stations; these typically record daily summary values. The available summary values of primary interest include precipitation, snowfall, snow depth, minimum air temperature, and maximum air temperature. These records are available from the National Climatic Data Center (NCDC) on CD-ROM, in the form of (i) state-wide series for station establishment through 1993, (ii) all stations for 1994 through 1996, and (iii) all stations for 1997. In addition to the 1994-1996 and 1997 CD-ROMs, three pre-1994 state CD-ROMS were acquired this month

- California
- Arizona and Nevada
- Utah and New Mexico

These CD-ROMs include a station history file and a station observation file for each state. There is also an NCDC online file that describes the location of each of the COOP stations, including latitude, longitude, and elevation. Some of the stations were moved during the period of service. The time-averaged location was used for these stations. Several of the elevations reported in the CD-ROM data were missing, clearly incorrect, or misread, so a processing check was performed to replace the CD-ROM information with the online file when the two elevations disagreed by more than 30 m.

Some of the COOP stations, with WBAN numbers, also maintain a higher measurement degree. These stations record additional variables, such as wind speed, cloud cover, and dew point. In addition, the records are available at more frequent intervals, at least hourly and sometimes more frequently. Unfortunately, there are relatively few WBAN stations in the region of interest. The daily summaries for these stations are available from the NOAA web site. All WBAN stations are also COOP stations, but the WBAN daily summaries also report additional information beyond the COOP information such as atmospheric pressure and percent of solar radiation. Data from a total of 18 stations were acquired (15 in NV, 1 in CA, 2 in UT), of which 2 have unusably short records. Of the usable stations, 10 include atmospheric pressure and 5 include percent of solar radiation.

An hourly record of solar radiation is available for a 30-yr period (1961 through 1990) from the Solar and Meteorological Surface Observation Network (SAMSON). All observations in the US are available on a 3-CD-ROM set from the NCDC. Observed data include several different forms of solar radiation, temperature, relative humidity, wind speed and direction, atmospheric pressure,

and precipitation (although not all of these are necessarily available at each station). The CD-ROM with the western states was acquired. There are 8 stations that should be useful: Tonopah, Ely, McCarren, Reno, Elko, Winnemucca, Barstow, CA, and Cedar City, UT. Several other stations exist in Arizona, Utah, and Idaho that might be useful, although these are fairly far from YM.

Data is also available for download from the DOE Technical Library web site. Several sets of met stations are maintained by DOE and USGS. The DOE has nine stations, while USGS has at least five stations (five are in the DOE online database) plus a network of non-recording gauges. Summary information on precipitation, temperature, relative humidity, and solar flux was obtained for the period 1986 through 1997 for the nine DOE stations, as well as hourly precipitation records for each of the stations for parts of the period (1993, half of 1994, 3/4 of 1995, half of 1996, and 1997). The obtained files are all labeled starting with *MS*, for monitoring station, with the names also including station IDs, range of dates, and met data (precipitation is implied). The hourly readings for temperature, relative humidity, solar flux, and atmospheric pressure (among others) are also available for download covering the same period of time, but it would take roughly a day to download all of this information. Probably the best thing to do is to request a data packet from DOE if the information is required, since the missing records may be available as well as the records for 1986 through 1992.

Hourly readings of relative humidity, temperature, solar flux, and windspeed were obtained for the five USGS stations over the period 10/1/94 through 10/1/95. Each variable is downloaded in 18 files; these were concatenated, extraneous header and tail information were removed, and the resulting files collected in an Excel spreadsheet.

The network of nonrecording gauges available online includes the periods 1/1/90-9/30/91, 10/1/93-9/30/94, and 11/1/94-9/30/95. Various other area nonrecording gauges are available online for the periods 2/84-9/85 and 3/89-9/90. These data were collected at intervals (*e.g.*, weekly, monthly); some intervals may be several months. These five sequences were obtained; as with the DOE stations, it may be best to request them directly in order to obtain a complete sequence of data.

Precipitation data were also obtained for 17 Nevada Test Site locations covering the period 10/1/82 through 9/27/85. These data appear to be part of a longer sequence that would be useful to obtain. Longer sequences from these stations form part of the basis for some of the infiltration modeling work performed by the USGS.

Daily data from four weather stations maintained by the USGS (McKinley and Oliver, 1994, McKinley and Oliver, 1995) in the 3 Springs area were obtained. These stations are used to

provide estimates of recharge at future-climate analog sites (Lichty and McKinley, 1995). The data include precipitation, soil and air temperature, relative humidity, and solar flux. Some of the records in the html download file were obviously mislabeled (inconsistent location name, inconsistent month or year); these records were corrected and the data were extracted from the download file and collated into a *Matlab* binary file.

9/22/99 Analysis of mean climatic parameters.

Analysis of climatic parameters is motivated by two functions: (i) distribution of conditions affecting *MAI* to individual pixels, so that areal-average estimates can be obtained; and (ii) distribution of conditions affecting vegetation to analog sites, so that vegetative species and density can be estimated for given climatic conditions.

The primary variables influencing net infiltration are precipitation (water source) and temperature (evapotranspiration). Evapotranspiration also depends on atmospheric vapor density, windspeed, and both shortwave and longwave radiation. Vegetation density depends on all of these variables as well, although precipitation, temperature, and shortwave radiation should be the primary climatic indicators for vegetative species mix and density. Shortwave radiation should be well predicted if latitude and ground slope are known, as long as some indication of cloudiness patterns can be determined. Unless there are strong regional or elevational trends in cloudiness that can be explicitly accounted for, it should be sufficient to use estimates of radiation assuming clear-sky conditions when predicting vegetation quantities.

Numerical simulation of a water balance using *breath* requires precipitation, air temperature, atmospheric vapor density, wind speed, shortwave radiation, and longwave radiation. Future modifications to *breath* may also require atmospheric pressure. When using numerical simulation to predict *MAI*, experience has shown that it is adequate to use hourly variation for the days immediately preceeding, during, and immediately after precipitation, and monthly variation outside this window. The importance of the window is because potential evapotranspiration is reduced on these days, due to increased relative humidity, decreased solar radiation, and cooler temperatures. The reduced evapotranspiration enables deeper penetration of wetting fronts during the window than would otherwise have occurred, thereby increasing the fraction of water reaching below the ET trap.

Based on all of these considerations, the primary variables of interest for analysis are *MAP* and *MAT*. The approach followed by Hevesi et al. (1992) was to cokrige *MAP* and elevation,

using stations in the area of YM. As an alternative, I choose to use a much wider range of data locations, use a regional interpolation, and only then see how well the YM information fits into the regional picture. An advantage of this approach is that regional information is available for much longer time periods than local information and is better distributed spatially. The local information provides a reality check and information on local variability.

The COOP data is the workhorse data set for precipitation and temperature, as there are hundreds of stations in Nevada and surrounding states. For the analyses, data from all stations in NV, AZ, UT, and CA with actual observations attached to stations in the station history file were extracted from the CD-ROMs in a standard format. Some stations were listed in the station history but had no observations, while some observations in the data file referenced nonexistent COOPS (usually only a month per station). A procedure was adopted that compensates for missing values and mismatched record lengths. An array of 366 julian days was created for each variable type (*e.g.*, precipitation, temperature). Each data observation was added to the data array and a counter for the corresponding day was incremented. The mean value for the day is obtained by dividing the sum of values by the number of observations. The annual value is obtained by the average of the mean array (the 366th day is weighted by 0.25 in the average, since it only occurs once every four years). Maximum and minimum values for each day as well as frequencies of nonzero occurrence were also accumulated. Extraction from the CD-ROMs was performed for every AZ, CA, NV, and UT station. The complete extraction took several hours.

After complete extraction, a reduced set of stations was extracted from the complete set. The reduced extraction includes all NV stations, all UT stations west of longitude 113, all AZ stations west of longitude 113 and north of latitude 35, and all CA stations east of longitude 118.2 and north of latitude 34.5 (north of the San Gabriel mountains and east of the crest of the southern Sierra Nevadas). All stations in Inyo and Mono counties were also explicitly included. The boundaries were selected to include stations in more-or-less the same climatic regime with at least a 2-degree buffer on every side of YM. The Sierra Nevada and San Gabriel ranges make natural boundaries, while the northern and eastern boundaries are more diffuse.

Note that it may be advantageous to also extract statistics by precipitation categories, such as precipitation bins, day before, day after, and interstorm. This information could provide information useful for generating storm and meteorological sequences. It would probably be necessary to lump numerous stations to generate robust parameters, although it is not obvious whether statistics should also be stratified by elevation. Extraction of these parameters would likely take several hours, although only a fraction of the stations originally extracted should be examined. Some of this work would fit nicely with the work that David Woolhiser is doing.

Most of the variables of interest don't require a tremendously long period of observation to be reasonably well estimated. Seasonally, atmospheric variables tend to be quite repetitive from year to year. On the other hand, precipitation is highly variable from year to year and annual averages require decades of observations to estimate reliably in the semiarid Mojave and Great Basin. Thus, stations with shorter records can be used for analyses of atmospheric variables than for precipitation. In the following analyses, the effect of record length is examined. Generally speaking, inclusion of all stations with record lengths at least 10 yr is adequate to estimate regression parameters, although the less-sensitive parameters may vary in their significance as the minimum record lengths change. The record length in years is defined as the number of observations divided by 365.25.

The pieces of information attached to each station that can be used for regression include latitude, longitude, and elevation. In the region of interest, annual-average clear-sky shortwave radiation is almost linear with latitude, so that a significant regression with one will provide a significant regression with the other (say for temperature). Temperature also generally varies linearly with elevation in the atmosphere, so there should be a good regression between temperature and elevation. There are orographic effects that tend to increase precipitation with elevation, while particularly in summer rain can evaporate while falling (decreasing precipitation with lowering of elevation). Therefore elevation should play a role in precipitation, but may be more important during the summer. Also, it is generally accepted that the Sierra Nevada range provides a rain shadow that lessens from west to east, perhaps providing a longitudinal impact. A quick inspection shows an exponential increase in MAP with elevation, suggesting that the logarithm of MAP is more appropriate than MAP directly (consistent with the results of Hevesi et al. (1992)).

Several observations are quickly apparent in the data. The maximum-temperature data can be quite well predicted using elevation and latitude/shortwave radiation. The minimum-temperature data is less well predicted using these factors, and there does not appear to be a strong regional effect in the error. Thus, local effects are probably significant in minimum temperature. Minimum temperature can be impacted by drainage of dense, cold air downslope from local hills or mountains; additional work is required to examine this type of effect. A quick feel might be obtained by overlaying the prediction errors on a topo map or DEM. I've downloaded the set of USGS 1-250,000 scale DEMs for most of the area of interest (some of the CA areas are missing), and Center for Nuclear Waste Regulatory Analyses (CNWRA) has the USGS topo maps at the same scale.

Local maximum slope or local curvature might be a likely predictor for additional regression analysis, reasoning that slope is required for drainage but a bowl may be necessary to capture the

air. Actually a valley bottom would be good too. Using a DEM, the predictors should be the maximum of the 4 local slopes and the maximum of the 4 local curvatures (N-S, E-W, NW-SE, NE-SW). Perhaps the maximum of the 8 local slopes should be checked too.

The log-precipitation data is also most strongly dependent on elevation, with some regional effect showing up as slight dependence on latitude and longitude. There is quite a bit of scatter around the regressions. Spatial plots of error over the region suggest that there are regional effects that are not linearly dependent on latitude and longitude.

A systematic set of regressions were performed for MAP, MAT, mean annual maximum temperature, mean annual minimum temperature, mean winter precipitation (julian days 281 through 170), and mean summer precipitation (julian days 171 through 280). For each regression, each multiple of elevation, latitude, longitude (Z, Lt, Lg, ZLt, ZLg, $LtLg$, and $ZLtLg$) was considered a predictor. All possible combinations of predictors were examined (individual, pairwise, triplets, etc.). Statistics are reported for each combination.

9/27/1999 Results of analysis.

SAS

The COOP data were run through a regression analysis to determine predictive relationships as a function of spatial location (*e.g.*, latitude, longitude, elevation). Solar radiation is also important in an energy balance, so potential solar radiation was used as a base variable as well. Potential solar radiation is almost linear with latitude in the area of interest. All four base variables were normalized to keep coefficients of the same order of magnitude. Elevation was converted to kilometers, with normalization between 34 and 42 degrees for latitude, 113 and 120 degrees for longitude, and 280 and 310 W/cm^2 for solar radiation. *Correction dated 9/29/1999: This was corrected to units of J/cm^2/dy by multiplying by 3600/365.25, or normalization from 2750 to 3050 J/cm^2/dy.* SAS
The regression analysis was performed with a routine written in *Matlab* called analyze_fit_set.

In the analysis, regression variables were created from all possible multiplicative combinations of 1, 2, or 3 base variables (a total of 34 combined variables). For example, elevation (Z) is presented as Z, Z^2, and Z^3 as well as with all other combinations of the remaining 3 base variables. A regression was performed using one combined variable at a time to determine the best single-variable predictor. The analysis was repeated with each combination of combined-variable pairs to find the best predictor pair. Higher-order sets were also searched until the point of diminishing returns was reached. Note that computational burdens became significant if more than triplets were considered (more than 5×10^4 analyses for quads and more than 3×10^5 analyses for quintuplets).

Each of the COOP stations have different record lengths. It is desirable to include as many stations as possible, while restricting the stations to ones with valid record lengths. Using the R^2 criterion as a basis, experimentation suggests that temperature predictions improve with number of stations (more extreme elevations), while precipitation predictions improve with length of record (thereby using only stations with appropriate means). Balancing of these factors appears to be reasonably achieved by using stations with record lengths of greater than 20, 5, and 40 yr for precipitation, temperature, and snow precipitation, respectively. The complete set of best predictions for each number of predictor variables is shown in Table 1-17 (for precipitation), Table 1-18 (for winter and summer precipitation), and Table 1-19 (for temperature). Corresponding scatterplots of observed versus predicted values are shown in Figures 1-14 through 1-15.

For temperature and snow precipitation, improvement is minimal if more than pair-wise combinations are considered. For precipitation, there is still improvement from 5- to 6-way combinations. Interestingly, the mean annual values for precipitation are better predicted than either summer or winter precipitation, although winter prediction is significantly better than summer prediction. The slow but steady improvement as additional predictor variable are added suggested that another type of interpolation might provide better results. A set of radial basis functions were added to the base variables, replacing all of the combination variables. The basis function locations were selected to provide a regular grid in normalized latitude/longitude coordinates. Both radial $[r = (Nt^2 + Ng^2)^{1/2}]$ and inverse-radial $(1/r)$ bases were used, with radial bases appearing to provide slightly better results. Limiting the *MAP* prediction to 6 predictors in the original scheme provides a best R^2 of 0.793. Using 9 predictors in the inverse-radial scheme for a grid on the one-third markers (*i.e.*, 0, 1/3, 2/3, and 1) in both directions provides a best R^2 of 0.782 (0.763 for 6 predictors). Using 7 predictors in the radial scheme with the same grid provides a best R^2 of 0.802 (0.796 for 6 predictors). The radial scheme is nominally superior to the original scheme, and is considerably less computationally demanding to exhaustively examine than the original scheme, due to the fewer possible variables. In the numbering scheme, grid locations are called poles and are numbered consecutively from left to right, moving from the bottom left corner to the top right corner. The best 7-predictor radial scheme has a minimum and maximum ratios of observed to predicted *MAP* of 0.64 and 1.69, respectively. Despite the nominal improvement, the original formulation is easier to implement and less arbitrary in selction of pole locations. There is still at least one predictor variable missing from the formulation, based on the remaining scatter.

The precipitation and temperature values for the nine DOE met stations in the YM area over the period 1986 through 1997 are shown as crosses in the scatterplots. The data for these nine stations are shown as a function of elevation in Figure 1-16. These values were not used in the regressions. The met station values for precipitation are well within the scatter of predicted-versus-

Table 1-17: Best estimated fits to mean annual COOP precipitation meteorological data. All fits are to the base-10 logarithm of the data.

SSE	R^2	$\min(V_{obs} - V_{reg})$	$\max(V_{obs} - V_{reg})$	Variables
MAP: 171 stations with at least 20 yr record				
1.2	0.515	-0.329	0.333	Z
0.856	0.631	-0.279	0.343	Z NtNgSw
0.669	0.700	-0.282	0.316	Z NgSw SwSwSw
0.552	0.744	-0.234	0.266	Z NgSw NgNgSw SwSwSw
0.490	0.759	-0.219	0.269	Nt ZSw NgSw ZNtNt NgNgSw
0.420	0.793	-0.220	0.275	Z SwSw NtNtNg NtNgNg NgNgNg NgSwSw
MAP: Inverse-radial basis functions (choice of 16 poles)				
1.2	0.515	-0.329	0.333	Z
0.847	0.639	-0.259	0.286	Z P7
0.652	0.715	-0.265	0.233	Z P1 P7
0.558	0.739	-0.242	0.210	Z P1 P7 P11
0.494	0.754	-0.228	0.229	Z P1 P7 P9 P11
0.449	0.763	-0.237	0.224	Z Ng P1 P7 P9 P11
0.412	0.772	-0.249	0.236	Z Ng P1 P6 P7 P9 P11
0.383	0.779	-0.253	0.239	Z Ng P1 P6 P7 P9 P11 P12
0.360	0.782	-0.257	0.234	Z Ng P1 P6 P7 P9 P10 P11 P12
MAP: Radial basis functions (choice of 16 poles)				
1.2	0.515	-0.329	0.333	Z
0.814	0.667	-0.315	0.266	Z P7
0.631	0.733	-0.279	0.237	Z Nt P7
0.529	0.765	-0.214	0.234	Z P5 P7 P9
0.468	0.780	-0.207	0.251	Z P7 P13 P14 P16
0.417	0.796	-0.186	0.227	Z P4 P5 P7 P9 P14
0.384	0.802	-0.195	0.228	Z Ng P5 P7 P9 P14 P16
0.355	0.810	-0.196	0.212	Z Ng Sw P1 P5 P7 P15 P16
0.330	0.818	-0.200	0.231	Z Nt Sw P7 P9 P11 P12 P14 P15

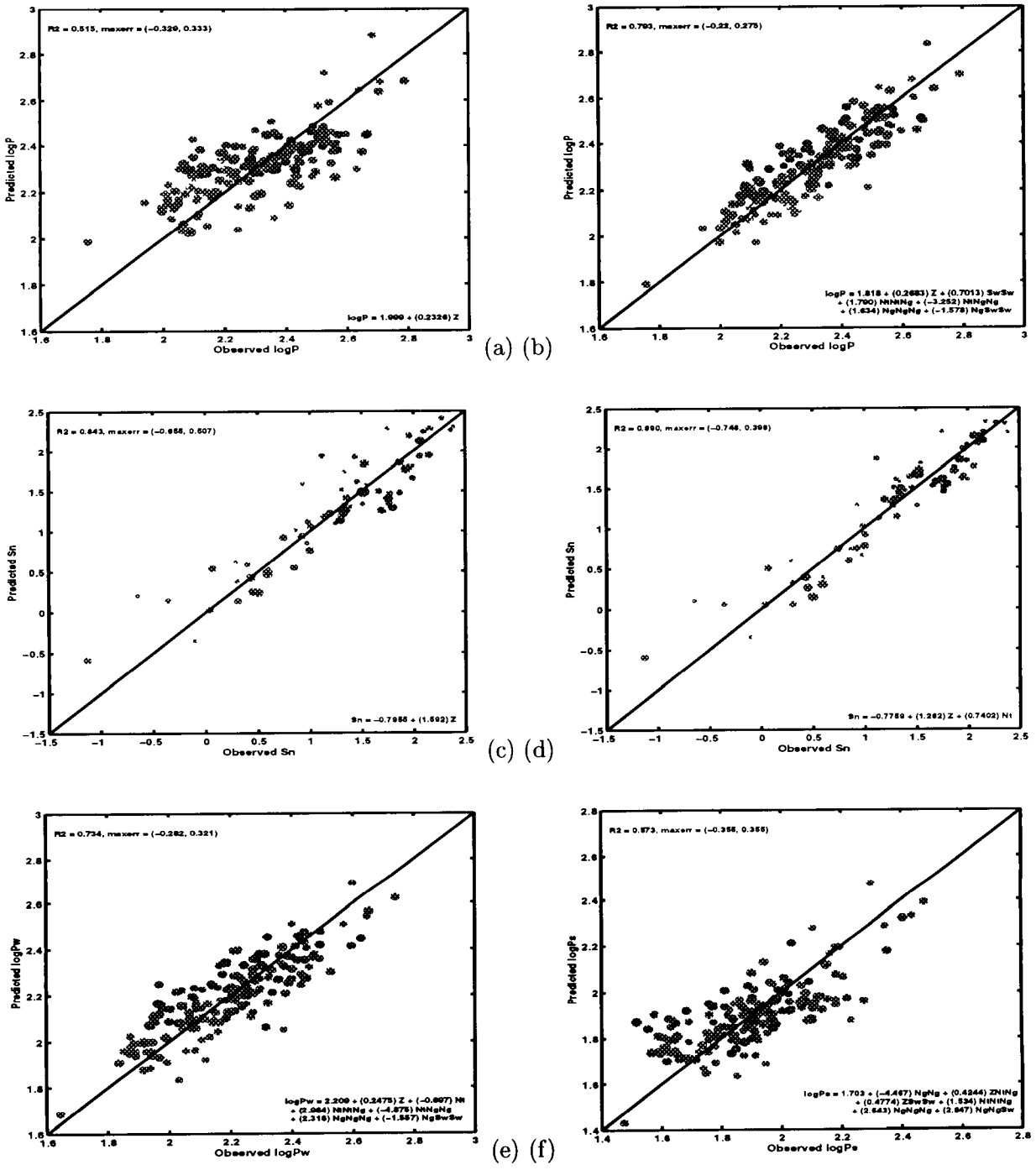

Figure 1-14: 9/27/1999. Scatterplot of observed versus predicted mean annual log-10 precipitation, (a) 1 and (b) 6 predictors; log-10 snowfall, (c) 1 and (d) 2 predictors; and (e) winter (day 281 through 170) and (f) summer (day 171 through 280) precipitation, 6 predictors. Crosses represent DOE met stations in the YM area. Area of circles are proportional to length of record. Circle color changes from red to blue on west to east. Circle fill changes from red to blue on south to north.

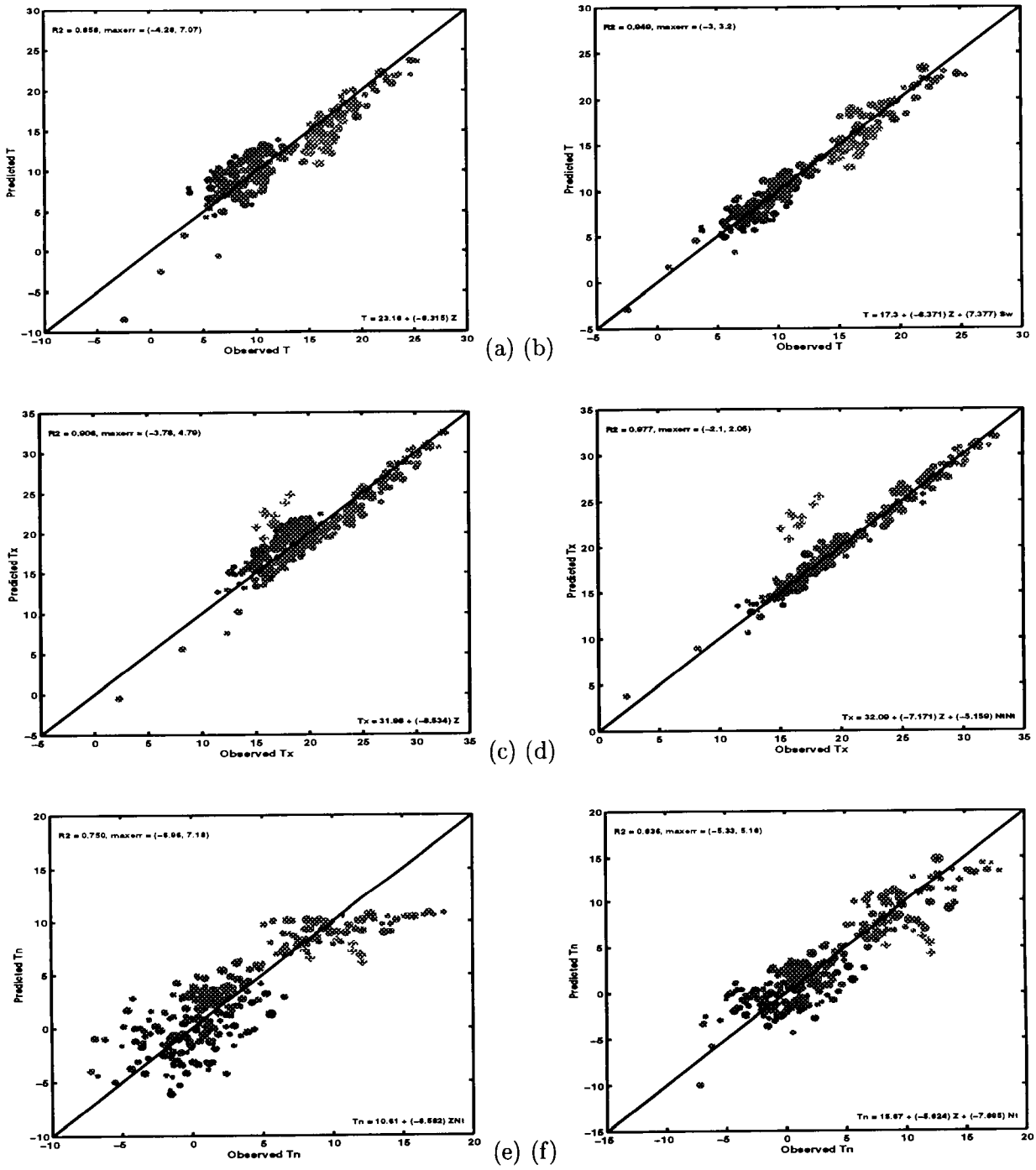

Figure 1-15: 9/27/1999. Scatterplot of observed versus predicted mean annual temperature, (a) 1 and (b) 2 predictors; maximum temperature, (c) 1 and (d) 2 predictors; and minimum temperature, (e) 1 and (f) 2 predictors. Crosses represent DOE met stations in the YM area. Area of circles are proportional to length of record. Circle color changes from red to blue on west to east. Circle fill changes from red to blue on south to north.

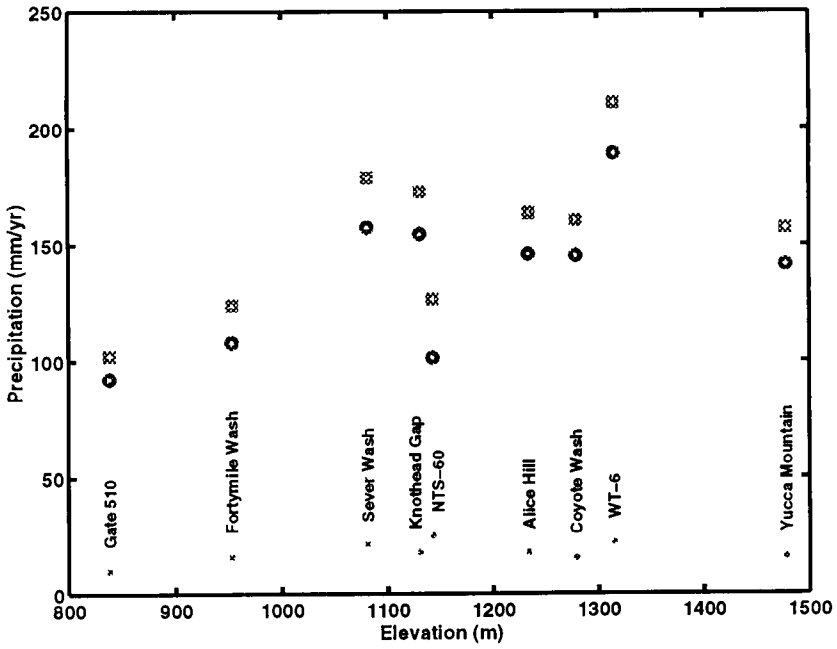

(a)

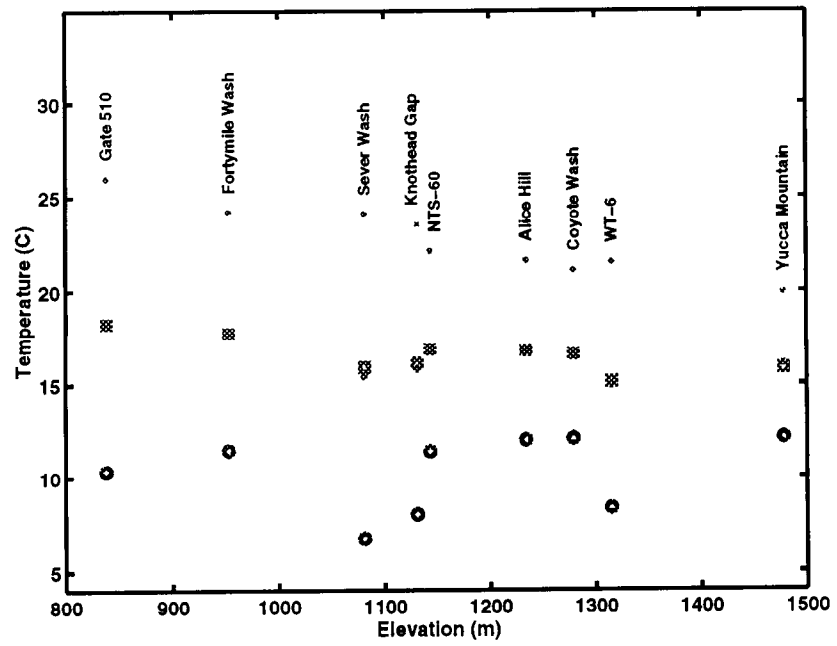

(b)

Figure 1-16: 9/27/1999. Scatterplot of observed (a) mean summer (dot), winter (circle), and annual (square) precipitation; and (b) mean annual maximum (dot), minimum (circle), and average (square) temperature at DOE meteorologic stations. Crosses represent average of minimum and maximum temperatures.

Table 1-18: Best estimated fits to mean annual COOP precipitation (summer and winter) meteorological data, as well as snowfall depth. All fits are to the base-10 logarithm of the data.

SSE	R^2	$\min(V_{obs} - V_{reg})$	$\max(V_{obs} - V_{reg})$	Variables
Summer MAP: 171 stations with at least 20 yr record				
1.48	0.313	-0.347	0.388	ZZ
1.10	0.427	-0.328	0.405	Z NtNtSw
0.935	0.450	-0.335	0.380	ZSw SwSw ZNtNt
0.804	0.492	-0.329	0.339	Z NgNg NtNtSw
0.716	0.517	-0.388	0.373	ZSw NgNg NtNtNg NgNgNg NgNgSw
0.623	0.573	-0.355	0.355	NgNg ZNtNg ZSwSw NtNtNg NgNgNg NgNgSw
Winter MAP: 171 stations with at least 20 yr record				
1.25	0.520	-0.342	0.285	Z
0.938	0.596	-0.297	0.315	Z NtSw
0.786	0.622	-0.322	0.286	Z NtNgSw NgNgNg
0.667	0.660	-0.291	0.256	Z NtSw NgNg NgNgNg
0.584	0.686	-0.310	0.281	ZSw NgNg NtNtNg NgNgNg NgNgSw
0.498	0.734	-0.282	0.321	Z Nt NtNtNg NtNgNg NgNgNg NgSwSw
Snowfall: 73 stations with at least 40 yr record				
1.76	0.843	-0.855	0.507	Z
1.2	0.890	-0.748	0.398	Z Nt

observed points. The values for *MAT* are warmer than the regression equation by a few degrees Celsius, but are generally within the scatter of predicted-versus-observed points. Regionally, *MAT* decreases by about 6.37 °C with every kilometer of elevation, while the 9 DOE met stations have a shallower decrease of 4 to 5.5 °C/km. The regional decrease is shallower than the two-point Desert Rock/Kawitch slope (8.3 °C/km) I used in distributing *MAT* on DEMs for predictions of *MAI*, and the local YM decrease is shallower still. Predictions of *MAI* should be re-evaluated with the corrected values.

Interestingly, both the annual-average maximum and minimum temperature values are outside the scatter of coop points, especially the maximum temperature points. The maximum temperature points are significantly warmer than the regression while the minimum temperature points are significantly cooler than the regression, yet the difference between maximum and minimum temperature tends to be less than typical for coop stations by roughly 4 °C. The difference between

Table 1-19: Best estimated fits to mean annual COOP temperature data.

SSE	R^2	$\min(V_{obs} - V_{reg})$	$\max(V_{obs} - V_{reg})$	Variables
MAT: 262 stations with at least 5 yr record				
21.5	0.858	-4.28	7.07	Z
10.5	0.949	-3.00	3.2	Z Sw
T_{max}: 262 stations with at least 5 yr record				
17.4	0.906	-3.78	4.79	Z
7	0.977	-2.10	2.05	Z NtNt
T_{min}: 262 stations with at least 5 yr record				
30.2	0.75	-6.96	7.18	ZNt
19.9	0.836	-5.33	5.18	Z Nt
$T_{max} - T_{min}$: 262 stations with at least 5 yr record				
26.3	0.064	-6.26	5.23	ZZZ
20.7	0.132	-6.12	5.09	ZZZ NtNtSw

maximum and minimum temperature decreases with increasing elevation. These effects seem to be due to local effects. Maximum readings at and near the YM crest may be representative of warmer low-elevation air advected during the windy daylight hours. At night there appears to be drainage of cool air downslope and warm air upslope; minimum temperatures appear to increase with elevation, aside from 3 stations at the base of drainages that have anomalously cool minimum temperatures. I think that the relatively poorer prediction of regional mean annual minimum temperature is probably due to similar local drainage patterns. This conclusion is supported by the lack of regional trends in mean annual temperature difference in the coop dataset.

9/29/1999 More results of analysis.

An error was made in the discussion and analysis regarding the units for shortwave radiation. In the original analyses, shortwave radiation was calculated without multiplying by the number of seconds in an hour, affecting the normalizing values for shortwave radiation. The shortwave radiation values were changed to mean daily shortwave radiation [J/cm^2] rather than annual radiation, so that the normalizing values reported above should be multiplied by 3600/365.25. Also, the 366th day of the year was given unit weight rather than 1/4 weight (leap year only) in calculating annual radiation. The modification of the leap year calculation results in regression coefficients that are different from the coefficients in the figures by a small amount, but the conclusions shouldn't be changed at all.

Table 1-20: Annual meteorological summary data from USGS analog sites.

MAP		MAT (°C)				Soil T		RH		Daily Solar	
mm/yr	Yr	Ave	Max	Min	Yr	°C	Yr	%	Yr	J/cm^2	Yr
3 Springs Basin - Kawich Peak Near Warm Springs											
369.13	4.00	6.37	9.62	1.00	3.95	5.62	4.00	44.20	2.00	1888	1.81
3 Springs Basin - 3 Springs Creek Near Warm Springs											
314.99	7.00	8.12	13.59	0.43	6.79	10.70	6.97	42.73	1.60	1820	6.92
East Stewart Basin - Veg Spring Near Ione											
524.89	6.00	6.71	9.19	-0.84	3.24	3.54	4.00	46.89	1.96	1375	1.81
East Stewart Basin - East Stewart Creek Near Ione											
476.63	6.92	4.66	8.13	-1.42	6.40	5.79	6.75	45.20	1.00	1651	6.66

A quick comparison was made to estimate the predictive power of the previously used relationships between *MAP*, *MAT*, and elevation. The R^2 value for the Hevesi et al. (1992) formula used for the 171 stations with at least 20 yr of data is 0.299 (the best elevation-only fit I came up with is 0.515 for the same data). The R^2 value for the 262 stations with at least 5 yr of data is 0.599 using the formula based on Desert Rock and 3 Springs, while the new elevation-only figure is 0.858.

I extracted annual summaries for the variables reported by McKinley and Oliver (1994) and McKinley and Oliver (1995). The data were obtained from the DOE Technical Library web site. These annual summaries are reported in Table 1-20.

Note that there are some odd things going on between mean air temperature and mean soil temperature; the soil temperature is inconsistently between 2.6°C warmer and 3.2°C cooler.

9/30/1999 More results of analysis.

The USGS has operated a set of high-elevation precipitation gauges in southern and eastern Nevada. The sites range from 7760 through 10650 ft in elevation. David Groeneveld was able to obtain observations from these sites. The observations were made by emptying the gauges twice a year, in October and in May. The record length is from 1984 through 1998 for some and 1986 through 1998 for the others. David reports problems with missing or apparently incorrect values for some of the sites; one of the 12 sites had sufficient holes in the data record that David eliminated it from consideration. Both David Groeneveld and David Woolhiser think that winter snow may be

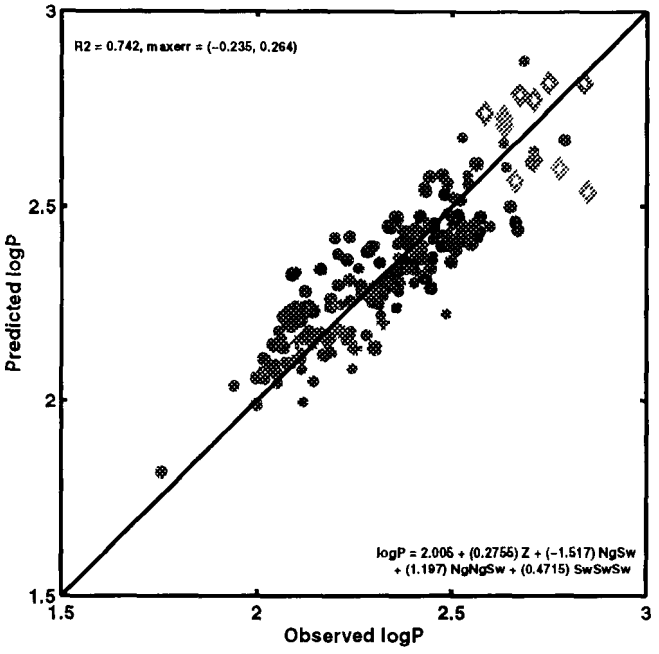

Figure 1-17: 9/30/1999. Scatterplot of observed mean annual precipitation versus predicted. Crosses represent DOE met stations at YM. Dark cyan diamonds represent eastern NV stations and olive diamonds represent southern NV stations. Circles represent coop stations (only these were used for regression). Circle size is proportional to station record length. Circle color moves from red to blue as stations are located east to west. Circle fill moves from red to blue as stations are located south to north.

under-represented in the data set. David patched holes in the remaining records through regression techniques. This patching is documented in David's scientific notebook.

I plotted the high-elevation data on top of the scatterplots for the coop station regressions for comparison, in Figure 1-17 (for *MAP*) and Figure 1-18 (for summer and winter precipitation). The regressions use fewer predictors than the best-fit cases, but the fits are nearly as good and much faster to recreate.

The fit for *MAP* is quite good, and both the regression and the high-elevation data appear to be from the same population. Note that the coop points have at least 20 yr of observations, while the high-elevation points have at best 16 yr of observations.

The winter/summer data periods are somewhat different for the coop stations and for the

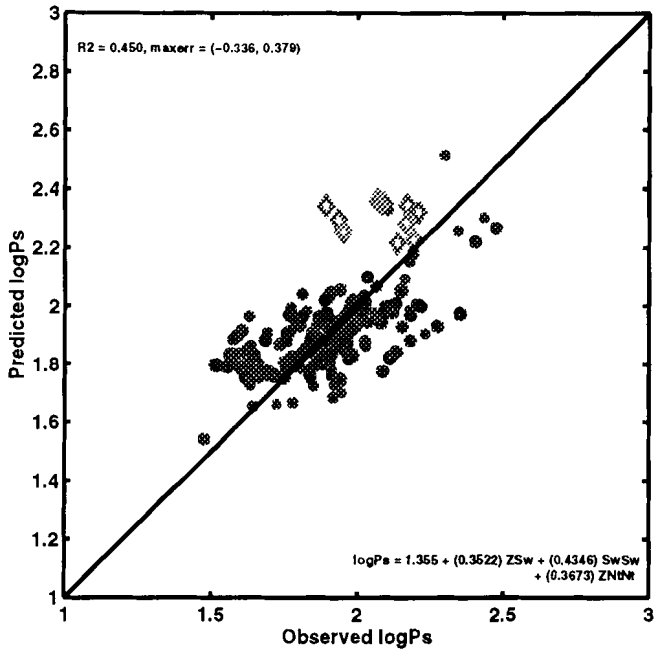

(a)

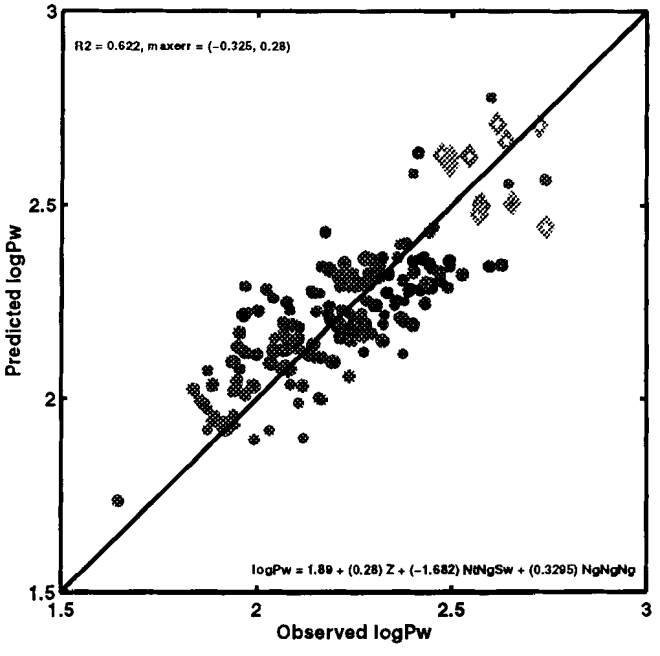

(b)

Figure 1-18: 9/30/1999. Scatterplot of observed (a) mean summer and (b) mean winter precipitation. temperature at DOE meteorologic stations. Data points use the same codes as in Figure 1-17.

high-elevation sites, with a shorter summer for coop stations (day 171 through 280) than for the high-elevation sites (roughly May through October). Thus, summer precipitation for the high-elevation sites is somewhat larger than it should be for perfect comparison with the coop data, and winter is somewhat smaller. The effect is more obvious in the summer data, since summer precipitation is smaller and the same absolute error will have a larger relative error in the set with the smaller average. Nevertheless, both summer and winter sets are also reasonably compatible. In summary, I think we have a pretty good representation for annual precipitation, temperature, and snowfall, good enough to publish.

It would be of great interest, for weather-generation purposes, to also examine the daily statistics (*e.g.*, fraction of wet days, fraction of wet days followed by wet, temperatures on wet versus dry days, etc.). Probably the statistics for temperature should be according to a bin based on precipitation. Typically these statistics are described by Fourier series. I would imagine that statistics would be much more robust if the same type of regression analysis as was performed for mean annual statistics were performed using all stations at the same time. In order to perform the analysis, the same type of extraction from the CD-ROMs would be required; however, the resulting output files would be considerably larger, since more information would be saved. The extraction would also be a little more complex, since strings of days would be examined rather than just single days and cross-comparisons of more than one data type would be required.

These coop statistics only address precipitation and temperature. Although these are the most important statistics, information required for generating the weather required for modeling infiltration also includes vapor density and incoming radiation. The SAMSON data should help out on these fronts.

References

Allison, G. B., G. W. Gee, and S. W. Tyler. 1994. Vadose-Zone Techniques for Estimating Groundwater Recharge in Arid and Semiarid Regions. *Soil Science Society of America Journal 58*(1), 6–14.

Allison, G. B. and M. W. Hughes. 1978. The Use of Environmental Chloride and Tritium to Estimate Total Recharge to an Unconfined Aquifer. *Australian Journal of Soil Research 16*, 181–195.

Andrews, R. W., T. F. Dale, and J. A. McNeish. 1994. *Total System Performance Assessment-1993: An Evaluation of the Potential Yucca Mountain Repository.* B00000000-01717-2200-00099-Rev.01, Intera, Inc., Las Vegas, NV.

Bagtzoglou, A. C., N. M. Coleman, E. C. Pearcy, S. A. Stothoff, and G. W. Wittmeyer. 1997. Unsaturated and Saturated Flow Under Isothermal Conditions. In B. Sagar (Ed.), *NRC High-Level Radioactive Waste Program FY96 Annual Progress Report*, Volume NUREG/CR-6513, No. 1, Washington, DC, pp. 10–1–10–28. Nuclear Regulatory Commission.

Bagtzoglou, A. C., S. A. Stothoff, and M. A. Muller. 1995. *Progress Towards Estimating Infiltration and Deep Percolation at the Yucca Mountain Site.* , Center for Nuclear Waste Regulatory Analyses, San Antonio, TX.

Barnes, C. J., G. Jacobson, and G. D. Smith. 1994. The Distributed Recharge Mechanism in the Australian Arid Zone. *Soil Science Society of America Journal 58*(1), 31–40.

Brown, T., S. Conrad, S. Wirth, J. Cochran, and J. Emery. 1997. *Plausible Future Climate States at the Area 5 Radioactive Waste Management Site, Nevada Test Site.* SNL-?, Sandia National Laboratories, Albuquerque, NM.

Buesch, D. C., R. W. Spengler, T. C. Moyer, and J. K. Geslin. 1996. *Proposed Stratigraphic Nomenclature and Macroscopic Identification of Lithostratigraphic Units of the Paintbrush Group Exposed at Yucca Mountain, Nevada.* Open-File Report 94-469, United States Geological Survey, Denver, CO.

Campbell, G. S. 1985. *Soil Physics with BASIC.* Amsterdam, The Netherlands: Elsevier Science Publishers B.V.

Carsel, R. F. and R. S. Parrish. 1988. Developing Joint Probability Distributions of Soil Water Retention Characteristics. *Water Resources Research 24*(5), 755–769.

Clausnitzer, V. and J. W. Hopmans. 1993. *An Algorithm for Three-Dimensional, Simultaneous Modeling of Root Growth and Transient Soil Water Flow, V 1.0.* LAWR Paper No. 100022, Department of Land, Air, and Water Resources, University of California, Davis, CA.

Clausnitzer, V. and J. W. Hopmans. 1994. Simultaneous modeling of transient three-dimensional root growth and soil water flow adaptation. *Plant and Soil 164*, 299–314.

Conrad, S. H. 1993. Using Environmental Tracers to Estimate Recharge Through an Arid Basin. In *Proceedings of the Fourth Annual International Conference on High Level Radioactive Waste Management*, La Grange Park, IL, pp. 132–137. American Nuclear Society.

Day, W. C., C. J. Potter, D. S. Sweetkind, and C. A. S. Juan. 1998. *Bedrock geologic map of the central block area, Yucca Mountain, Nye County, Nevada.* Miscellaneous Investigations Series I-2601, United States Geological Survey, Denver, CO.

du Bray, E. A., D. O. Hurtubise, and C. A. Bannister. 1987. *Geologic Map of the Weepah Spring Wilderness Study Area, Lincoln and Nye Counties, Nevada 1:50,000.* Miscellaneous Field Studies Map MF-1922, United States Geological Survey, Denver, CO.

Electric Power Research Institute. 1990. *Demonstration of a Risk-Based Approach to High-Level Waste Repository Evaluation.* EPRI NP-7057, Electric Power Research Institute, Palo Alto, CA.

Electric Power Research Institute. 1992. *Demonstration of a Risk-Based Approach to High-Level Waste Repository Evaluation: Phase 2.* EPRI TR-100384, Electric Power Research Institute, Palo Alto, CA.

Electric Power Research Institute. 1996. *Yucca Mountain Total System Performance Assessment, Phase 3.* EPRI TR-107191, Electric Power Research Institute, Palo Alto, CA.

Eslinger, P. W., L. A. Doremus, D. W. Engel, T. B. Miley, M. T. Murphy, W. E. Nichols, M. D. White, D. W. Langford, and S. J. Ouderkirk. 1993. *Preliminary Total-System Analysis of a Potential High-Level Nuclear Waste Repository at Yucca Mountain.* PNL-8444, Pacific Northwest Laboratory, Richland, WA.

Evans, D. D., T. W. Sammis, and D. R. Cable. 1981. Actual Evapotranspiration under Desert Conditions. In D. D. Evans and J. L. Thames (Eds.), *Water in Desert Ecosystems*, pp. 195–218. Stroudsburg, PA: Dowden, Hutchinson, and Ross, Inc.

Fabryka-Martin, J. T., P. R. Dixon, S. Levy, B. Liu, H. J. Turin, and A. V. Wolfsberg. 1996a. *Systematic Sampling for Chlorine-36 in the Exploratory Studies Facility.* LA-CST-TIP-96-001, Los Alamos National Laboratory, Los Alamos, NM.

Fabryka-Martin, J. T., H. J. Turin, A. V. Wolfsberg, D. Brenner, P. R. Dixon, and J. A. Musgrave. 1996b. *Summary Report of Chlorine-36 Studies.* LA-CST-TIP-96-003, Los Alamos National Laboratory, Los Alamos, NM.

Fayer, M. J. and T. L. Jones. 1990. *UNSAT-H Version 2.0: Unsaturated Soil Water and Heat Flow Manual.* PNL-6779, Pacific Northwest Laboratory, Richland, WA.

Fernandez, J. A., J. B. Case, C. A. Givens, and B. C. Carney. 1994. *A Strategy to Seal Exploratory Boreholes in Unsaturated Tuff.* SAND93-1184, Sandia National Laboratories, Albuquerque, NM.

Flint, A. L., J. A. Hevesi, and L. E. Flint. 1996a. *Conceptual and Numerical Model of Infiltration for the Yucca Mountain Area, Nevada.* Milestone 3GUI623M, Department of Energy, Las Vegas, NV.

Flint, L. E. 1996. *Matrix Properties of Hydrogeologic Units at Yucca Mountain, Nevada.* Milestone 3GUP604M, Department of Energy, Las Vegas, NV.

Flint, L. E. and A. L. Flint. 1990. *Preliminary Permeability and Water-Retention Data for Nonwelded and Bedded Tuff Samples, Yucca Mountain Area, Nye County, Nevada.* Open-File Report 90-569, United States Geological Survey, Denver, CO.

Flint, L. E. and A. L. Flint. 1995. *Shallow Infiltration Processes at Yucca Mountain, Nevada–Neutron Logging Data 1984-93.* Water-Resources Investigations Report 95-4035, United States Geological Survey, Denver, CO.

Flint, L. E., A. L. Flint, and J. A. Hevesi. 1994. Shallow Infiltration Processes in Arid Watersheds at Yucca Mountain, Nevada. In *Proceedings of the Fifth Annual International Conference on High Level Radioactive Waste Management*, La Grange Park, IL, pp. 2315–2322. American Nuclear Society.

Flint, L. E., A. L. Flint, C. A. Rautman, and J. D. Istok. 1996b. *Physical and Hydrologic Properties of Rock Outcrop Samples at Yucca Mountain, Nevada.* Open-File Report 95-280, United States Geological Survey, Denver, CO.

Fonteyn, P. J. and B. E. Mahall. 1981. An experimental analysis of structure in a desert plant community. *Journal of Ecology 69*, 883–896.

Gee, G. W., P. J. Wierenga, B. J. Andraski, M. H. Young, M. J. Fayer, and M. L. Rockhold. 1994. Variations in Water Balance and Recharge Potential at Three Western Desert Sites. *Soil Science Society of America Journal 58*(1), 63–72.

Gerwitz, A. and E. R. Page. 1974. An Empirical Mathematical Model to Describe Plant Root Systems. *Journal of Applied Ecology 11*, 773–782.

Goodall, D. W. 1952. Some considerations in the use of point quadrats for the analysis of vegetation. *Australian Journal of Scientific Research 5*, 1–41.

Groeneveld, D. P. 1997. Vertical point quadrat sampling and an extinction factor to calculate leaf area index. *Journal of Arid Environments 36*(3), 475–485.

Heady, J. F., R. P. Gibbens, and R. W. Powell. 1959. A comparison of the charting, line intercept and line-point methods of sampling shrub types of vegetation. *Journal of Range Management 12*, 180–188.

Herwitz, S. R. and L. Olsvig-Whittaker. 1989. Preferential upslope growth of *Zygophyllum dumosum* Boiss. (Zygophyllaceae) roots into bedrock fissures in the northern Negev desert. *Journal of Biogeography 16*, 457–460.

Hevesi, J. A., J. D. Istok, and A. L. Flint. 1992. Precipitation Estimation in Mountainous Terrain Using Multivariate Geostatistics. Part I: Structural Analysis. *Journal of Applied Meteorology 31*(7), 661–676.

Hickman, J. C. 1995. *The Jepson manual of higher plants of California.* Berkeley, CA: University of California Press.

Lachenbruch, A. H. and J. H. Sass. 1977. Heat Flow in the United States and the Thermal Regime of the Crust. In H. G. Heacock (Ed.), *The Earth's Crust*, Volume Geophysical Monograph 20, pp. 626–675. Washington, DC: American Geophysical Union.

Leary, K. D. 1990. *Analysis of Techniques for Estimating Potential Recharge and Shallow Unsaturated Zone Water Balance Near Yucca Mountain, Nevada.* Ph. D. thesis, University of Nevada, Reno, NV.

Lichty, R. W. and P. W. McKinley. 1995. *Estimates of Ground-Water Recharge Rates for Two Small Basins in Central Nevada.* Water-Resources Investigations Report 94-4104, United States Geological Survey, Denver, CO.

Long, A. and S. W. Childs. 1993. Rainfall and Net Infiltration Probabilities for Future Climate Conditions at Yucca Mountain. In *Proceedings of the Fourth Annual International Conference on High Level Radioactive Waste Management*, La Grange Park, IL, pp. 112–121. American Nuclear Society.

McKenna, S. A. and C. A. Rautman. 1995. *Summary Evaluation of Yucca Mountain Surface Transects with Implications for Downhole Sampling.* SAND94-2038, Sandia National Laboratories, Albuquerque, NM.

McKinley, P. and T. Oliver. 1994. *Meteorological, Stream-Discharge, and Water-Quality Data for 1986 through 1991 from Two Small Basins in Central Nevada.* Open-File Report 93-651, United States Geological Survey, Denver, CO.

McKinley, P. and T. Oliver. 1995. *Meteorological, Stream-Discharge, and Water-Quality Data for Water Year 1992 from Two Basins in Central Nevada.* Open-File Report 94-456, United States Geological Survey, Denver, CO.

Nichols, W. D. 1987. *Geohydrology of the Unsaturated Zone at the Burial Site for Low-Level Radioactive Waste Near Beatty, Nye County, Nevada.* Water-Supply Paper 2312, United States Geological Survey, Denver, CO.

Noy-Meir, I. 1973. Desert ecosystems: environment and producers. *Annual Review of Ecological Systems 4*, 25–52.

Nuclear Regulatory Commission. 1992. *Initial Demonstration of the NRC's Capability to Conduct a Performance Assessment for a High-Level Waste Repository.* NUREG-1327, Nuclear Regulatory Commission, Washington, DC.

Nuclear Regulatory Commission. 1995. *NRC Iterative Performance Assessment Phase 2: Development of Capabilities for Review of a Performance Assessment for a High-Level Waste Repository.* NUREG-1464, Nuclear Regulatory Commission, Washington, DC.

Phillips, F. M. 1994. Environmental Tracers for Water Movement in Desert Soils of the American Southwest. *Soil Science Society of America Journal 58*(1), 15–24.

Quade, J. and T. E. Cerling. 1990. Stable Isotopic Evidence for a Pedogenic Origin of Carbonates in Trench 14 near Yucca Mountain, Nevada. *Science 250*, 1549–1552.

Ratliff, L. F., J. T. Ritchie, and D. K. Cassel. 1983. Field-Measured Limits of Soil Water Availability as Related to Laboratory-Measured Properties. *Soil Science Society of America Journal 47*, 770–775.

Rautman, C. A., L. E. Flint, A. L. Flint, and J. D. Istok. 1995. *Physical and Hydrologic Properties of Rock Outcrop Samples From a Nonwelded to Welded Tuff Transition, Yucca Mountain, Nevada.* Water-Resources Investigations Report 95-4061, United States Geological Survey, Denver, CO.

Rousseau, J. P., E. M. Kwicklis, and D. C. Gillies (Eds.). 1996. *Hydrogeology of the Unsaturated Zone, North Ramp Area of the Exploratory Studies Facility, Yucca Mountain, Nevada*, Water-Resources Investigations Report 96-????, Denver, CO. United States Geological Survey. Draft dated 8/29/96.

Sandia National Laboratories. 1992. *TSPA 1991: An Initial Total-System Performance Assessment for Yucca Mountain.* SAND91-2795, Sandia National Laboratories, Albuquerque, NM.

Sandia National Laboratories. 1994. *Total-System Performance Assessment for Yucca Mountain–SNL Second Iteration (TSPA-1993).* SAND93-2675, Sandia National Laboratories, Albuquerque, NM.

Sass, J. H. and A. H. Lachenbruch. 1982. *Preliminary Interpretations of Thermal Data from the Nevada Test Site.* Open-File Report 82-973, United States Geological Survey, Reston, VA.

Sass, J. H., A. H. Lachenbruch, W. W. Dudley, Jr., S. S. Priest, and R. J. Munroe. 1988. *Temperature, thermal conductivity, and heat flow near Yucca Mountain, Nevada: Some tectonic and hydrologic implications.* Open-File Report 87-649, United States Geological Survey, Denver, CO.

Sass, J. H., A. H. Lachenbruch, and C. W. Mase. 1980. *Analysis of Thermal Data From Drill Holes UE25a-3 and UE25a-1, Calico Hills and Yucca Mountain, Nevada Test Site.* Open-File Report 80-826, United States Geological Survey, Menlo Park, CA.

Scanlon, B. R. 1991. Evaluation of moisture flux from chloride data in desert soils. *Journal of Hydrology 128*, 137–156.

Scanlon, B. R. 1992. Evaluation of Liquid and Vapor Water Flow in Desert Soils Based on Chlorine 36 and Tritium Tracers and Nonisothermal Flow Simulations. *Water Resources Research 28*(1), 285–297.

Schenker, A. R., D. C. Guerin, T. H. Robey, C. A. Rautman, and R. W. Barnard. 1995. *Stochastic Hydrogeologic Units and Hydrogeologic Properties Development for Total-System Performance Assessments.* SAND94-0244, Sandia National Laboratories, Albuquerque, NM.

Schmidt, M. R. 1989. Classification of Upland Soils by Geomorphic and Physical Properties Affecting Infiltration at Yucca Mountain, Nevada. Master's thesis, Colorado School of Mines, Golden, CO.

Scott, R. B. and J. Bonk. 1984. *Preliminary Geologic Map (1:12,000 scale) of Yucca Mountain, Nye County, Nevada, with Geologic Cross Sections.* Open-File Report 84-494, United States Geological Survey, Denver, CO.

Šimůnek, J., T. Vogel, and M. T. van Genuchten. 1992. *The SWMS_2D code for simulating water flow and solute transport in two-dimensional variably saturated media V. 1.1.* Research Report No. 126, U. S. Salinity Laboratory, ARS USDA, Riverside, CA.

Somma, F., V. Clausnitzer, and J. W. Hopmans. 1997. *An Algorithm For Three-Dimensional, Simultaneous Modeling Of Root Growth, Transient Soil Water Flow, And Solute Transport And Uptake, Version 2.1.* LAWR Paper No. 100034, Department of Land, Air, and Water Resources, University of California, Davis, CA.

Stephenson, N. L. 1990. Climate control of vegetation distribution: The role of the water balance. *The American Naturalist 135*, 649–670.

Sternberg, P. D., M. A. Anderson, R. C. Graham, J. L. Beyers, and K. R. Rice. 1996. Root distribution and seasonal water status in weathered granitic bedrock under chapparal. *Geoderma 72*, 89–98.

Stothoff, S. A. 1997. Sensitivity of long-term bare soil infiltration simulations to hydraulic properties in an arid environment. *Water Resources Research 33*(4), 547–558.

Stothoff, S. A. and A. C. Bagtzoglou. 1995. Estimation of Recharge at Yucca Mountain, Nevada. *Supplement to Eos, Transactions 76*(46), F242.

Stothoff, S. A. and A. C. Bagtzoglou. 1996. Subregional Hydrogeologic Flow and Transport Processes. In B. Sagar (Ed.), *NRC High-Level Radioactive Waste Research at CNWRA, July–December 1995*, Volume CNWRA 95-02S, San Antonio, TX, pp. 9–1–9–20. Center for Nuclear Waste Regulatory Analyses.

Stothoff, S. A., A. C. Bagtzoglou, and H. Castellaw. 1996. Estimation of Spatial Distribution of Recharge Factors at Yucca Mountain, NV. In *Proceedings of the International Conference on Application of Geographic Information Systems in Hydrology and Water Resources Management*, Vienna, Austria. International Association of Hydrological Sciences.

Stothoff, S. A., H. M. Castellaw, and A. C. Bagtzoglou. 1995. Estimation of Spatial Distribution of Recharge Factors at Yucca Mountain. In B. Sagar (Ed.), *NRC High-Level Radioactive Waste Research at CNWRA, January–June 1995*, Volume CNWRA 95-01S, San Antonio, TX, pp. 9–5–9–12. Center for Nuclear Waste Regulatory Analyses.

Sykes, J. F., J. L. Wilson, and R. W. Andrews. 1985. Sensitivity Analysis for Steady State Groundwater Flow Using Adjoint Operators. *Water Resources Research 21*(3), 359–371.

TRW. 1995. *Total System Performance Assessment–1995: An Evaluation of the Potential Yucca Mountain Repository.* B00000000-01717-2200-00136, TRW Environmental Safety Systems Inc., Las Vegas, NV.

Tyler, S. W. and G. R. Walker. 1994. Root Zone Effects on Tracer Migration in Arid Zones. *Soil Science Society of America Journal 58*(1), 25–31.

van Genuchten, M. T. 1980. A Closed-form Equation for Predicting the Hydraulic Conductivity of Unsaturated Soils. *Soil Science Society of America Journal 44*, 892–898.

Yang, I. C., G. W. Rattray, and P. Yu. 1996. *Interpretations of Chemical and Isotopic Data From Boreholes in the Unsaturated Zone at Yucca Mountain, Nevada.* Water-Resources Investigations Report 96-4058, United States Geological Survey, Denver, CO.

Zwieniecki, M. A. and M. Newton. 1995. Roots growing into rock fissures: Their morphological adaptation. *Plant and Soil 172*, 181–187.

front is much more diffuse. For low-permeability transport systems, the transport density tends to drop off more rapidly with depth.

I realized that the change in density term should read

$$\frac{\partial \rho}{\partial t} = \left(\frac{q - q_o}{q_o}\right)\left(\frac{\rho_o - \rho}{\rho_o}\right)\rho \tag{3-48}$$

with the terms in front of ρ on the right-hand side limited to $\pm\alpha$. There is still some question in my mind as to how constraints from nutrients can be accommodated.

7/19/99 Generic equations.

It is useful to have a capability for solving generic 1D equations and systems of equations in which the actual equations and coefficients are defined through easily modified scripts and the work of equation assembly, equation solution, and state variable manipulations are handled with generic solvers. If done properly, coding up a different equation should be very fast.

There are several types of 1D equations that should be accommodated. These include a diffusion equation, a transport equation, and a phase balance equation. The form of a diffusion equation is

$$\frac{\partial u}{\partial t} - \nabla \cdot (K \nabla u) = Src; \tag{3-49}$$

a transport equation is

$$\frac{\partial u}{\partial t} + \nabla(vu) - \nabla \cdot (K \nabla u) = Src; \tag{3-50}$$

and a phase balance equation is

$$\frac{\partial M}{\partial t} - \nabla \cdot [K(\nabla u + G \nabla z)] = Src. \tag{3-51}$$

In the above, u, M, and z represent state variables; K, v, and G represent parameters; and Src represents source terms.

The generic form of all of these equations is

$$\frac{\partial M}{\partial t} + \nabla \cdot q = Src. \tag{3-52}$$

The system form of the generic equations is

$$\sum_j \left[\alpha_{ij} \frac{\partial M_{ij}}{\partial t} + \nabla \cdot \beta_{ij} \mathbf{q}_{ij} = Src_{ij}\right], \tag{3-53}$$

where an i subscript represents the primary state variable, a j subscript represents secondary state variables, $\mathbf{q}$ is flux, and the α and β variables are flags for inclusion of terms in the equation. Fully implicitly discretizing this system using a finite volume approach in 1D,

$$\sum_j \left\{ \alpha_{ij} \left[\frac{M_{ij}}{\Delta t} \right]_n^{n+1} + \beta_{ij} \left. \frac{\Delta \mathbf{q}_{ij}}{\Delta x} \right|^{n+1} = Src_{ij}|^{n+1} \right\}; \tag{3-54}$$

rearranging yields

$$\sum_j \left\{ \alpha_{ij} \left[M_{ij} \right]_n^{n+1} V + \beta_{ij} \Delta t \, \Delta \mathbf{q}_{ij}|^{n+1} = V \Delta t \, Src_{ij}|^{n+1} \right\}, \tag{3-55}$$

where Δ denotes a difference operator (Δt is the time step and other quantities are the difference between one side of the volume and the other) and V is the volume of the element ($V = \Delta x$).

When the system includes nonlinearities, a first-order increment is added to the equation set

$$\begin{aligned} &\sum_j \left\{ \alpha_{ij} \left[M_{ij} \right]_n^m V + \beta_{ij} \Delta t \, \Delta \mathbf{q}_{ij}|^m - V \Delta t \, Src_{ij}|^m \right\} \\ &\quad + \sum_k \sum_j \left\{ \alpha_{ij} V \, M_{ij}|_m^{m+1} + \beta_{ij} \Delta t \Delta \left(\mathbf{q}_{ij}|_m^{m+1} \right) - V \Delta t \, Src_{ij}|_m^{m+1} \right\} = 0, \end{aligned} \tag{3-56}$$

where u is an unknown, n is the time step level, and m is the iteration level (implicitly at the $n+1$ time step). This form also works for linear equations, as the incremental part of the time derivative is the only active part and the remainder of the terms cancel except for the incremental part.

The generic solver needs to handle the following fluxes, (i) $\mathbf{q} = -K \nabla u$ (diffusion), and (ii) $\mathbf{q} = \mathbf{v} u$ (advection). When u represents elevation, gravity-dependent flux is accommodated, which implies a loose definition of state variable. It would be useful to enable specification of K for adjacent finite volumes and have the generic solver provide the appropriate interface value (*e.g.*, harmonic mean, geometric mean, upstream value, flux-limited value). The solver also needs to handle the following zeroth- and first-order sources (i) $Src_{ij} = f_{ij}$ (specified source), (ii) $Src_{ij} = \lambda_{ij} u_j$ (decay), and (iii) $Src_{ij} = \Lambda_{ij}(u_j - u_i)$ (transfer).

The various increment terms are approximated by the generic expansions for variable c

(taking advantage of the chain rule)

$$c|_m^{m+1} = \left(\frac{\partial c}{\partial \chi}\right)^m \delta \tag{3-57}$$

$$(c\nabla u_j)|_m^{m+1} = c^m \left(\frac{\partial u_j}{\partial \chi}\right)^m \nabla\delta + \left(\frac{\partial u_j}{\partial \chi}\right)^m \delta\nabla\chi^m, \tag{3-58}$$

$$(cu_j)|_m^{m+1} = \left[c^m \left(\frac{\partial u_j}{\partial \chi}\right)^m + \left(\frac{\partial c}{\partial \chi}\right)^m u_j^m\right] \delta, \tag{3-59}$$

$$\delta = \chi|_m^{m+1}. \tag{3-60}$$

Typically δ is solved for rather than u.

The individual applications should provide α_{ij}, β_{ij}, K_{ij}, $\mathbf{v}_j$, λ_{ij}, Λ_{ij}, and f_{ij}. For each of these values, the corresponding array of sensitivity coefficients should also be provided. In *Matlab*, storage could be sparse for each of these arrays if significant numbers of coefficients are zero. Of course, storage is not a constraint in 1D.

In multiphase flow and transport, constraints on volume fractions and mass fractions are applied. Constraints on mass fractions are applied for each phase by adding together all species mass-balance equations for the phase, replacing one mass fraction with a weighted sum of the others, and neglecting the corresponding species balance equation in favor of the summed equation. Constraints on volume fractions are applied by summing together the equations for all phases, replacing one volume fraction with a weighted sum of the others, and neglecting the corresponding phase equation in favor of the summed equation. Mechanisms should be provided to do this, with automatic switching to constrain the largest volume fraction and largest mass fraction in each phase (avoiding roundoff error).

A second type of facility may be nice. It is possible to strictly enforce nonnegativity or boundedness through transforms. A log transform enforces nonnegativity at the cost of disallowing zero values (useful for concentration), while a tanh transform enforces boundedness between -1 and 1 at the cost of disallowing the limiting values (useful for saturation or mass fraction after adaptation). Both of these transforms can be applied after the coefficient array is assembled by multiplying columns in the coefficient array corresponding to the transformed variable. These transforms are

$$\frac{\partial()}{\partial \ln\chi} = \frac{1}{\chi}\frac{\partial()}{\partial\chi} \tag{3-61}$$

$$\frac{\partial()}{\partial \tanh\chi} = \operatorname{sech}^2(\chi)\frac{\partial()}{\partial\chi} \tag{3-62}$$

The reverse transform is easily obtained after solution.

9/3/99 Uptake/dispersal relationships.

SAS

A transfer function for uptake was developed for a 1D system last April. In actuality, uptake should be developed in a radial system. Dispersal from the leaf surfaces to the far field can also be treated in a radial system or in a cascade of radial systems (leaf to canopy, canopy to far field). The leaf to far field system is simpler, but doesn't account for clumping; perhaps in a highly diffusive system clumping doesn't matter.

As shown by Bear (1979), steady diffusive flux between two concentric cylinders (e.g., far field and well) is

$$Q = Aq_r = 2\pi r B K \partial\phi/\partial r = \text{constant} \tag{3-63}$$

where Q is radial flux, A is area, q_r is specific radial discharge, B is cylinder length, K is conductivity, ϕ is potential, and r is radius. This can be rearranged and integrated to yield

$$\frac{Q}{2\pi B} \ln\left(\frac{R}{r_w}\right) = \int_{\phi_w}^{\phi} K \, \mathrm{d}\phi. \tag{3-64}$$

When K is a constant, flux into the well is defined as

$$Q = 2\pi B K \ln\left(\frac{r_w}{R}\right)(\phi - \phi_w). \tag{3-65}$$

When K is assumed exponential [the Gardner approximation: $K = K_o \exp(\alpha\phi)$ for negative ϕ], flux into the well is defined as

$$Q = 2\pi B \ln\left(\frac{r_w}{R}\right)\left[\frac{K(\phi) - K(\phi_w)}{\alpha}\right]. \tag{3-66}$$

When there are two concentric cylinders, each with a constant K (say K_s for soil and K_p for plant wall), flux continuity requires that

$$2\pi B K_s \ln\left(\frac{r_w}{R}\right)(\phi_s - \phi_w) = 2\pi B K_p \ln\left(\frac{r_p}{r_w}\right)(\phi_w - \phi_p). \tag{3-67}$$

In the case

$$Q = ac(h - h_1) = bc(h_1 - h_2), \tag{3-68}$$

simplification and rearrangement yields

$$Q = \frac{abc}{a+b}(h - h_2). \tag{3-69}$$

Defining $Y_s = K_s \ln(r_w/R)$ and $Y_p = K_p \ln(r_p/r_w)$,

$$\phi_w = \frac{Y_s\phi_s + Y_p\phi_p}{Y_s + Y_p}, \tag{3-70}$$

and rearranging yields

$$Q = 2\pi B \left(\frac{Y_s Y_p}{Y_s + Y_p}\right)(\phi_s - \phi_p) = 2\pi B Y_e(\phi_s - \phi_p). \tag{3-71}$$

This relationship can be used directly for the uptake function. A particularly straightforward conceptual model for uptake within a 1D slice has N vertical cylinders uniformly distributed in the horizontal plane (note that gravity is not important at the scales being considered). With the assumption that the transport roots have little resistance compared to the soil/plant-wall system, the plant pressure can be assumed spatially uniform within the volume. Uptake length root density can be defined as

$$\rho_{ru} = \frac{NB}{AB}, \tag{3-72}$$

where ρ_{ru} is uptake root length density [L/L^3], B is the slice thickness [L], and A is the area of the slice [L^2]. The radius from root to far field is calculated by assigning equal area to each root, yielding

$$\pi R^2 = A/N = \frac{1}{\rho_{ru}} \tag{3-73}$$

$$R = \left(\frac{1}{\pi\rho_{ru}}\right)^{1/2} \tag{3-74}$$

Thus, the exchange radius is simply related to the uptake biomass.

Total transfer flux within the slice is

$$Q_{tot} = 2\pi N B Y_e(\phi_s - \phi_p), \tag{3-75}$$

and specific transfer flux is

$$\begin{aligned} q = \frac{Q_{tot}}{AB} &= \frac{2\pi N B Y_e}{AB}(\phi_s - \phi_p) \\ &= 2\pi\rho_{ru} Y_e(\phi_s - \phi_p). \end{aligned} \tag{3-76}$$

This relationship should work for generic volumes (not just slices in a 1D model). Typically a model would specify the uptake-root radii and plant-wall conductivity, adjusting Y_e and ρ_{ru} according to changes in soil conductivity and biomass.

The simple model for dispersal is similar to the model for uptake, except that the exchange surfaces are assumed to be spheres uniformly distributed throughout a volume V. Each sphere represents 2 stomates. By analogy to the uptake reasoning, steady diffusive flux between two concentric spheres (*e.g.*, far field and stomate) is

$$Q = Aq_r = 4\pi r^2 K \partial\phi/\partial r = \text{constant}. \tag{3-77}$$

This can be rearranged and integrated to yield (assuming K constant)

$$\frac{Q}{4\pi K}\left(\frac{1}{r_w} - \frac{1}{R}\right) = \phi - \phi_w, \tag{3-78}$$

so flux into the stomate is

$$\begin{aligned} Q &= 4\pi \left(\frac{Rr_w}{R - r_w}\right) K(\phi - \phi_w) \\ &\approx 4\pi r_w K(\phi - \phi_w) \end{aligned} \tag{3-79}$$

where the simplification occurs if $r_w \ll R$.

The value for R can be estimated by equating the volume of a sphere with radius R to the total volume divided by the number of stomate pairs, or

$$\frac{4\pi R^3}{3} = \frac{V}{N_s}, \tag{3-80}$$

where N_s is the total number of stomates in the volume V. Each plant has a characteristic number of stomates per leaf area, λ_s. When the leaf biomass is characterized by a leaf area density, ρ_l,

$$N_s = \lambda_s \rho_l V, \tag{3-81}$$

yielding an estimate for R of

$$R = \left(\frac{3}{4\pi\lambda_s\rho_l}\right)^{1/3} \tag{3-82}$$

A stomate is actually a 2D cavity, not a sphere. Assuming that a stomate pair is equivalent to one sphere (one stomate on each side of the leaf), equality of areas yields

$$A = 2(\pi r_s^2) = 4\pi r_w^2 \tag{3-83}$$

$$r_w = r_s/\sqrt{2} \tag{3-84}$$

Typical values from Kozlowski and Pallardy (1997) are $r_s = 3 \times 10^{-6}$ m, $\lambda_s = 3 \times 10^8$ m^{-2}, and $LAI = 2$ (where LAI represents the value for the canopy). Assuming a slab thickness of

0.1 m, $\rho_l = LAI/0.1 \approx 20$ m^{-1}. Let r_c is the radius of a disk containing the canopy (assume 0.5 m) and R_f is the far field for the disk (assume 2 m). Plugging in, $r_w \approx 2 \times 10^{-6}$ m, while $R \approx [3/(4\pi)(3 \times 10^8)(20)]^{1/3} \approx 3 \times 10^{-4}$ m. Clearly $r_w \ll R$ for the example, and flux from the stomate to the far field in the canopy must be dominated by the resistance at the stomate itself.

Specific transfer flux (flux per volume) is represented by

$$q = \frac{(N_s/2)4\pi r_w K}{V}(\phi - \phi_w) \tag{3-85}$$

yielding a specific transfer flux in the form

$$\begin{aligned} q &= \frac{\lambda_s \rho_l V 2\pi r_w K}{V}(\phi - \phi_w) \\ &= 2\pi r_w \lambda_s \rho_l K(\phi - \phi_w). \end{aligned} \tag{3-86}$$

Interestingly, the specific transfer flux is independent of the distance to the far field.

If the transfer is assumed to occur only within the plant canopy, which is represented by a disk, equating the cylinder formula to the flux produced in the disk yields

$$Q = 2\pi BK \ln\left(\frac{r_c}{R}\right)(\phi - \phi_c) = (2\pi r_c^2 B)2\pi r_w \lambda_s \rho_l K(\phi_c - \phi_w). \tag{3-87}$$

Using the relationships

$$\begin{aligned} a &= \ln\left(\frac{r_c}{R}\right) \\ b &= 2\pi r_c^2 r_w \lambda_s \rho_l \\ c &= 2\pi BK \end{aligned} \tag{3-88}$$

yields

$$Q = 2\pi BK \frac{ab}{a+b}(\phi - \phi_w). \tag{3-89}$$

Using the same typical values for estimates, $b = 2\pi(0.5)^2(2\times10^{-6})(3\times10^8)(20) \approx 2\times10^4$. Obviously $a \ll b$, so the transfer from the canopy to the far field is the rate-limiting step instead of transfer from stomates to the canopy. However, application requires a relationship between biomass and the ratio between canopy radius and far-field radius.

9/5/99 More dispersal relationships.

One conclusion from the prior analysis is that transfer rates may be greatly overpredicted if stomates are considered uniformly distributed throughout an atmospheric slice near the ground surface,

rather than localized within a canopy, since transfer rates from individual stomates were found to be independent of far-field distance. An unsettling implication of the disk analysis is that transfer is not affected by the number of stomates, which should be flat wrong. However, diffusion rates within the canopy would have to be orders of magnitude smaller within the canopy than within the inter-canopy areas to make the two resistances comparable. Presumably boundary-layer effects would provide reduction in diffusion rates just at the leaf surface, especially since the length scale for diffusion from stomate to canopy is about 1 mm, where the boundary layer is presumably strongest. Note that for 300 stomates/mm^2, there are many stomates within the effective radius for each stomate and the point estimate is misleading. Instead, we can return to the leaf scale to perform the analysis.

There are two types of leaves to consider, needles (*e.g.*, pine, ephedra) and plates (most other species). The needle case will be handled using cylinders, similarly to the uptake root analysis. The plate case will be handled using spheres, similarly to the stomate analysis.

Cylinder

Assume that each leaf is represented by a vertical cylinder extending from the top to the bottom of the individual slices, just like the uptake root analysis. A cylinder has a characteristic inner and outer radius, r_p and r_w, characterizing an outer wall punctured by stomates. Each needle has a characteristic length, b, so each cylinder consists of $n_n = B/b$ needles stacked atop each other, where B is the thickness of the canopy layer under consideration. Treating the leaf as a two-layer system within the canopy (leaf wall and far field), specific flux within a volume within the canopy is represented by

$$q = 2\pi\rho_{cd} Y_e(\phi_a - \phi_p) \tag{3-90}$$

$$Y_e = Y_a Y_p/(Y_a + Y_p)$$

$$Y_a = K_a \ln(r_w/R_c)$$

$$Y_p = K_p \ln(r_p/r_w) \tag{3-91}$$

where ρ_{cd} represents an equivalent dispersal length density within the canopy, R_c is the far field radius within the canopy, K_a is the conductivity of the far field, and K_p is the conductivity of the plant wall. The ρ_{cd} parameter is related to the more commonly measured parameters LAI (leaf

area per unit ground surface area) and r_c through surface area equality within a slice,

$$(2\pi r_w)N_c B = LAIA(A_c B)/V_c \tag{3-92}$$

$$\rho_{cd} = \frac{N_c B}{A_c B}, \tag{3-93}$$

where A_c is the area of the canopy, V_c is the volume of the canopy, and N_c is the number of cylinders in the canopy slice. Substitution yields

$$2\pi r_w \rho_{cd} = LAI(A/V_c) \tag{3-94}$$

$$\rho_{cd} = \frac{LAIA}{2\pi r_w V_c} \tag{3-95}$$

By assigning equal plan-view area to each leaf cylinder,

$$R_c = \left(\frac{1}{\pi \rho_{cd}}\right)^{1/2}. \tag{3-96}$$

For the purposes of estimation, assume $r_w = 1$ mm, $LAI = 0.1$ (averaged over plant support area), $H_c = 1$ m, $b = 1$ cm, $B = 10$ cm, $r_c = 0.5$ m, and $A = 10$ m^2. With these approximations, $\rho_{cd} \approx 200$ m/m^3 and $R_c \approx 0.04$ m. Using a typical air conductivity of $K = 1.5$ cm/s and typical stomatal conductivities of 0.15 and 1.5 cm/s (based on Table 12.1 by Kozlowski and Pallardy (1997)), $0.1K < Y_p < K$ and $Y_a \approx 2K$, or $0.1K < Y_e < (2/3)K$. Presumably desert vegetation would have conductivies in the lower part of the conductivity range.

The horizontal canopy to far field flux continuity requires

$$Q = 2\pi BK \ln\left(\frac{r_c}{R}\right)(\phi - \phi_c) = (A_c B)2\pi \rho_{cd} Y_e(\phi_c - \phi_w). \tag{3-97}$$

Using the relationships

$$\begin{aligned} a &= \ln\left(\frac{r_c}{R}\right) \\ b &= A_c \rho_{cd} Y_e / K \\ c &= 2\pi BK \end{aligned} \tag{3-98}$$

yields

$$Q = 2\pi BK \frac{ab}{a+b}(\phi - \phi_w). \tag{3-99}$$

Using the same typical values for estimates, $a \approx -2$ and $b = 0.785(200)(0.1\text{to}0.7)$ (implying $16 < b < 110$). Again $a \ll b$, so the transfer from the canopy to the far field is the rate-limiting step instead of transfer from needles to the canopy. Note that if the diffusion within the canopy

accounted for boundary layer effects, K within the canopy would be significantly smaller than K outside the canopy. If this effect were 1 to 2 orders of magnitude, both intercanopy and intracanopy diffusion would be of the same order of magnitude. Also note that the value of LAI represents a well-watered condition. When $Y_p = 0.1K$, a drop of one order of magnitude in LAI makes the leaf and far field resistances of the same order of magnitude, while a drop of two orders of magnitude makes the local resistance dominant. An extra order of magnitude drop is required for the other extreme.

If eddy diffusion is invoked, K is linearly proportional to wind velocity, which in turn logarithmically varies with distance from a surface. At the surface, molecular diffusion is the only active mechanism for transporting vapor (0.25 cm^2/s); eddy diffusion tens of meters from the surface may be orders of magnitude larger.

Sphere

Assume that each leaf is represented by a sphere with radius r_w. A characteristic sphere radius is found by equating surface areas,

$$\frac{4\pi r_w^2}{3} = 2A_l \tag{3-100}$$

$$r_w = \left(\frac{3A_l}{2\pi}\right)^{1/2} \tag{3-101}$$

where A_l is the area of one side of the leaf. From the stomate analysis, flux for one leaf is

$$Q = 4\pi \left(\frac{R_d r_w}{R_d - r_w}\right) K(\phi - \phi_w). \tag{3-102}$$

The value for R_d can be estimated by equating the volume of a sphere with radius R_d to the total volume divided by the number of leaves,

$$\frac{4\pi R_d^3}{3} = \frac{V}{N_l}, \tag{3-103}$$

where V is the volume of the canopy slice ($A_c B$) and N_l is the total number of leaves in the volume V. It is convenient to define a leaf area density within the canopy as total leaf area divided by canopy volume, or

$$\rho_{ac} = \frac{LAIA}{V_c}, \tag{3-104}$$

where V_c is the canopy volume. Using this density, N_l can be estimated by

$$N_l = \rho_{ac}\frac{BA_c}{2A_l}. \tag{3-105}$$

Substituting,

$$\frac{4\pi R_d^3}{3} = \frac{V}{\rho_{ac}V/(2A_l)} = \frac{2A_l}{\rho_{ac}} \tag{3-106}$$

$$R_d = \left(\frac{3A_l}{2\pi\rho_{ac}}\right)^{1/3} \tag{3-107}$$

For the purposes of estimation, assume $A_l = 1$ cm^2, $LAI = 0.1$ (support areal average), $V_c = 0.3$ m^3, $B = 0.1$ m, $r_c = 0.5$ m, and $A = 10$ m^2. With these approximations, $r_w \approx 0.7$ cm, $\rho_{ac} \approx 1.3$ m^2/m^3, $N_l \approx 500$, $V \approx 0.08$ m^3, and $R_d \approx 3.3$ cm. Neither R_d nor r_w can be neglected in determining flux in this case.

The canopy to far field flux continuity requires

$$Q = 2\pi BK\ln\left(\frac{r_c}{R}\right)(\phi - \phi_c) = 4\pi\left(\frac{R_d r_w}{R_d - r_w}\right)KN_l(\phi_c - \phi_w). \tag{3-108}$$

Using the relationships

$$\begin{aligned} a &= \ln\left(\frac{r_c}{R}\right) \\ b &= 2\left(\frac{R_d r_w}{R_d - r_w}\right)\left(\frac{\rho_{ac}A_c}{2A_l}\right) \\ c &= 2\pi BK \end{aligned} \tag{3-109}$$

yields

$$Q = 2\pi BK\frac{ab}{a+b}(\phi - \phi_w). \tag{3-110}$$

Using the same typical values for estimates, $a \approx -2$ and $b \approx 70$. Again, $a \ll b$, so the transfer from the canopy to the far field is the rate-limiting step instead of transfer from leaves to the canopy. With one to two orders of magnitude drop in LAI, the two components are of comparable magnitude; with three orders of magnitude drop, plant resistance is dominant.

One more approach might be examined, extending the concepts used here. The approach uses a cascade of leaf to branch cylinder, branch cylinder to canopy, and canopy to far field. This begins to get complex and the payback may be limited.

9/6/99 More dispersal relationships. SAS

Generic relationship

When conductivity is constant within the canopy and far field, both the cylinder and the sphere relationships boil down to the form

$$Q = 2\pi B K_a \frac{ab}{a+b}(\phi - \phi_w), \tag{3-111}$$

where

$$\begin{aligned} a &= \ln\left(\frac{r_c}{R}\right) \\ b_c &= 2\pi r_c^2 \rho_{cd} Y_e / K_a \\ Y_e &= Y_a Y_p / (Y_a + Y_p) \\ Y_a &= K_a \ln(r_w / R_c) \\ Y_p &= K_p \ln(r_p / r_w) \\ b_s &= 2\left(\frac{R_d r_w}{R_d - r_w}\right)\left(\frac{\rho_{ac} A_c}{2A_l}\right) \end{aligned} \tag{3-112}$$

where b_c is b for the cylinder case and b_s is b for the sphere case. Conductivity in these cases represents a vapor eddy diffusion coefficient (although some checking needs to be done to get the right units).

Boundary layer theory suggests that the mean velocity field increases away from a fixed surface. The increase can be described as a power law (Brutsaert, 1982),

$$\bar{u} = C_p u_* (z/z_0)^m \tag{3-113}$$

$$u_* = (\tau_0/\rho)^{1/2} \tag{3-114}$$

where u_* is the friction velocity. For neutral conditions $C_p \approx 5.5$ to 6.0 and $m = 1/7$. The parameter z_0 can be as small as 0.001 cm for mud flats and ice; presumably individual leaves are similarly smooth.

As discussed earlier, steady diffusive flux between two concentric cylinders (*e.g.*, far field and well) is

$$Q = Aq_r = 2\pi r B K \partial\phi/\partial r = \text{constant}, \tag{3-115}$$

which can be rearranged to provide

$$\frac{Q}{2\pi B}\int_{r_w}^{R}\frac{1}{rK}\,\mathrm{d}r = \phi - \phi_w. \tag{3-116}$$

Diffusivity is often considered proportional to mean velocity, or $D = \alpha\bar{u}$. When $K = \beta(r - r_w)^m$ (blithely using the 1D expression in radial coordinates),

$$\frac{Q}{2\pi B}\int_{r_w}^{R}\frac{1}{\beta r(r - r_w)^m}\,\mathrm{d}r = \phi - \phi_w. \tag{3-117}$$

Approximating the r term in the integral as the mean of the limits yields

$$\frac{Q}{2\pi B}\int_{r_w}^{R}\frac{1}{\beta r(r - r_w)^m}\,\mathrm{d}r \approx \frac{Q}{\pi B\beta(1-m)(r_w + R)}(R - r_w)^{1-m} = \phi - \phi_w. \tag{3-118}$$

9/8/99 More dispersal relationships.

The relationships developed to date have made me uneasy because of the insensitivity of resistance to leaf area. I expect that a shrub would only put out enough leaves to start reaching the point of no return, not slam past the point by orders of magnitude. Why would a shrub put out so many leaves that there is no marginal benefit in adding an additional leaf? I discussed this issue with Dani Or and he brought up the point that my integrations thus far neglected consideration of the path from the far field of individual leaves to the canopy perimeter. In effect, I placed all leaves at the perimeter, although the volume relations are not right for this case.

Let's look at the effect of uniformly spreading leaves throughout the volume without regard to canopy. This assumption was looked at with the stomates to some extent. The assumption is that the layer is well mixed, so the analysis does not depend on the details of the canopy distribution.

Using the stomate analysis, we find

$$Q_l = 4\pi\left(\frac{Rr_w}{R-r_w}\right)K(\phi-\phi_w) \tag{3-119}$$

$$\frac{4\pi}{3}R^3 = \frac{V}{N_l} = \frac{V}{V\rho_l/A_l} = \frac{A_l}{\rho_l} \tag{3-120}$$

$$R = \left(\frac{3A_l}{4\pi\rho_l}\right)^{1/3} \tag{3-121}$$

$$r_w = \left(\frac{A_l}{4\pi}\right)^{1/2} \tag{3-122}$$

$$q = \left(\frac{N_l}{V}\right)Q_l = \frac{4\pi\rho_l}{A_l}\left(\frac{Rr_w}{R-r_w}\right)K(\phi-\phi_w)$$

$$\approx \frac{\rho_l K}{r_w}(\phi-\phi_w) = \rho_l K\left(\frac{4\pi}{A_l}\right)^{1/2}(\phi-\phi_w) \tag{3-123}$$

where A_l is now total surface area for a typical leaf, ρ_l is the leaf area per unit volume on an areal basis, and a subscript w represents the leaf surface. Generally $r_w \ll R$, as with the stomate analysis, leading to the last approximation. The last form is satisfyingly simple and linearly dependent on leaf area density; the fuller form is not quite linearly dependent on leaf area density. An offline example suggests that the fuller form is appropriate once LAI (defined for the canopy) starts getting larger than 1; however, the approximate form is only 12 percent too small for $LAI = 10$ in the example.

9/13/99 More dispersal relationships.

The previous analysis can be adapted for the case where just the canopy is concerned. In this case,

$$q = \frac{4\pi\rho_{lc}}{A_l}\left(\frac{Rr_w}{R-r_w}\right)K(\phi-\phi_w) = \lambda K(\phi-\phi_w) \tag{3-124}$$

$$R = \left(\frac{3A_l}{4\pi\rho_{lc}}\right)^{1/3} \tag{3-125}$$

$$r_w = \left(\frac{A_l}{4\pi}\right)^{1/2} \tag{3-126}$$

where A_l is total surface area for a typical leaf, ρ_{lc} is the leaf area per unit volume within the canopy, λ is a transfer coefficient, and a subscript w represents the leaf surface.

Let's return to the idea of overall transfer from plant to far field. The dispersal relationship above is only step one. Step two is dispersal from within canopy to the canopy edge, and step three is dispersal from the canopy edge to far field (analyzed before).

The step two analysis has a difficulty, in that strictly speaking dispersal depends on the local value of ϕ, which varies throughout the canopy. Assuming dispersal takes place uniformly throughout the canopy (q = constant), however, integration is straightforward assuming a cylindrical slice with thickness B within the canopy

$$\frac{1}{r}\frac{\mathrm{d}}{\mathrm{d}r}\left(r\frac{\mathrm{d}\phi}{\mathrm{d}r}\right)+\frac{q}{K}=0, \tag{3-127}$$

where K is the conductivity in the canopy. This can be integrated to yield

$$\frac{\mathrm{d}\phi}{\mathrm{d}r}+\frac{qr}{2K}=0 \tag{3-128}$$

$$\phi-\phi_0+\frac{qr^2}{4K}=0 \tag{3-129}$$

Evaluating at the canopy edge,

$$\phi_0=\phi_c+\frac{qr_c^2}{4K} \tag{3-130}$$

$$\phi_c-\phi+\frac{q}{4K}(r_c^2-r^2)=0 \tag{3-131}$$

where r_c is the radius of the canopy. Further assuming that an effective canopy ϕ can be used to provide an equivalent q, define ϕ_m as ϕ at the radius enclosing half of the canopy area, or $r_m^2=r_c^2/2$. Plugging in results in the relationships

$$\phi_c-\phi_m+\frac{\lambda K}{4K}(\phi_w-\phi_m)(r_c^2-r_m^2)=0$$

$$\phi_m\left(1+\frac{\lambda r_c^2}{8}\right)=\phi_c+\phi_w\frac{\lambda r_c^2}{8}$$

$$\phi_m=\alpha\phi_c+(1-\alpha)\phi_w$$

$$\alpha=\frac{1}{1+(\lambda r_c^2/8)}$$

$$q=\lambda K[\phi_w-\alpha\phi_c-(1-\alpha)\phi_w]=\frac{\lambda K}{1+(\lambda r_c^2/8)}(\phi_w-\phi_c) \tag{3-132}$$

$$\phi_c-\phi+\frac{2\lambda}{8+\lambda r_c^2}(\phi_w-\phi_c)(r_c^2-r^2)=0 \tag{3-133}$$

$$\phi_0=\phi_c+\frac{2\lambda r_c^2}{8+\lambda r_c^2}(\phi_w-\phi_c) \tag{3-134}$$

The total flux at a particular radius r is

$$Q=-2\pi KB\frac{\partial\phi}{\partial r}=\frac{2\pi rBq}{2}=\frac{8\pi rB\lambda K}{8+\lambda r_c^2}(\phi_w-\phi_c). \tag{3-135}$$

Flux continuity at the canopy fringe for the canopy relationship and for a cylinder between the canopy and far field requires (flux defined as positive from leaf to far field)

$$Q = 2\pi BK \ln\left(\frac{R_f}{r_c}\right)(\phi_c - \phi) = \frac{8\pi r_c B\lambda K}{8 + \lambda r_c^2}(\phi_w - \phi_c). \tag{3-136}$$

Using the relationships

$$\begin{aligned} a &= \ln\left(\frac{R_f}{r_c}\right) \\ b &= \frac{4\lambda r_c}{8 + \lambda r_c^2} \\ c &= 2\pi BK \end{aligned} \tag{3-137}$$

yields

$$Q = 2\pi BK\frac{ab}{a+b}(\phi - \phi_w). \tag{3-138}$$

Using typical values for estimates ($r_c = 0.5$ m, $R_f = 2$ m, $A_l = 1$ cm^2, $\rho_{lc} = 3$ m^2/m^3), calculated values are $r_w = 2.8 \times 10^{-3}$ m, $R_w = 2. \times 10^{-2}$ m (leaf far field radius), $\lambda = 1.2 \times 10^3$ m^{-2}, $a = 1.4$, and $b = 7.8$. These values provide a restriction factor $ab/(a+b)$ that is fairly insensitive to leaf area density. For sensitivity to leaf area, b should be significantly smaller than a; b is linearly dependent on ρ_{lc}. If the ratio of canopy radius to far field radius increases, sensitivity to leaf area increases.

9/14/99 Other dispersal issues.

Transpiration is dependent on the difference between vapor density at the leaf and far field vapor density. It is typically assumed that the vapor density at the leaf surface is the saturated vapor density at the leaf temperature. In the sparse canopies of most desert shrubs, air and leaf temperature should be fairly close. Using the air temperature for leaf transpiration should provide a reasonable estimate of leaf vapor density.

9/17/99 Eddy diffusivity.

The formulation provided thus far uses the terminology of conductivity [L/T] and potential [L] to give a volume flux. Mass transfer is better stated in terms of vapor density.

Bare-soil evaporation in *breath* has used the idea of a logarithmic velocity profile to provide a quasi-steady two-point conductance (soil and far atmosphere, such as 2 m elevation). Conductance is iteratively determined based on wind speed and atmospheric stability. If transpiration is included at discrete elevations, the profile must include elevation-dependent velocity and thus elevation-dependent conductivity. This becomes more problematic as vegetation is included, as vegetation not only modifies the velocity profile through roughness but provides a source of vapor and energy. It may be desirable to discretize the profile in some way, which would require local values of conductivity.

Brutsaert (1982) discusses various approaches to characterizing transport of momentum, heat, and vapor in the lower atmosphere, and some of the explanation here is lifted from his text.

The lower atmosphere is broken into several layers. In the immediate vicinity of the surface, turbulence is affected by the roughness elements and may be damped by viscous effects. Brutsaert (1982) terms the lower layer the *interfacial (transfer) sublayer*. In smooth flow (*e.g.*, over ice or mud) it is called the *viscous sublayer*, with thickness on the order of $30\nu/u_*$, where ν is the kinematic viscosity and u_* is the friction velocity ($u_* = \sqrt{\tau/\rho}$), τ is momentum flux (stress), and ρ is density. Over a rough surface, the interfacial sublayer is called the *roughness sublayer*, with thickness on the order of the mean height of the roughness obstacles. If the rough surface is porous or permeable to the air stream, the interfacial sublayer can be called the *canopy sublayer*. Molecular diffusivities for vapor and heat are of the same order as kinematic viscosity, so in the interfacial sublayer scaling lengths for vapor, sensible heat, and momentum are very similar.

The next layer up is the *surface sublayer*, with the lowermost portion termed the *dynamic sublayer*. The dynamic sublayer extends to roughly 1 to 10 m above the surface, depending on atmospheric stability; the entire surface sublayer extends to about 10 m above the surface. In the dynamic sublayer, density stratification is negligible so that stability is not a concern and profiles are logarithmic.

Above the surface sublayer, the *defect sublayer* extends to an elevation of about 100 to 1000 above the surface, and the free atmosphere lies above. None of the vapor density measurements available for simulation are within the defect sublayer; most are at 2 m above the surface, at the top edge border of the dynamic sublayer. Accordingly, the defect layer and the free atmosphere will not be considered further.

The dynamic sublayer is the most tractable analytically. From dimensional analysis,

$$\frac{u_*}{z(\mathrm{d}\bar{u}/\mathrm{d}z)} = \kappa \tag{3-139}$$

where $\bar{u}$ is mean horizontal wind speed and κ is von Kármán's constant (roughly 0.4). Direct integration yields

$$\bar{u}_2 - \bar{u}_1 = \frac{u_*}{\kappa} \ln\left(\frac{z_2}{z_1}\right). \tag{3-140}$$

The zero-velocity intercept is called z_{0m}, the momentum roughness parameter. If the surface is rough, an offset distance d is used in the similarity formulation, yielding

$$\bar{u}_2 - \bar{u}_1 = \frac{u_*}{\kappa} \ln\left(\frac{z_2 - d}{z_1}\right). \tag{3-141}$$

Note that this relationship breaks down when $z \leq d$, and is not correct when z is slightly larger than d. The relationship for $\bar{u}$ when $z - d \gg z_{0m}$ is

$$\bar{u} = \frac{u_*}{\kappa} \ln\left(\frac{z - d}{z_{0m}}\right). \tag{3-142}$$

Other analyses replace $(z - d)$ with $(z - d + z_{0m})$.

A similar analysis for vapor flux (surface to air), E, yields

$$E = -\frac{a_v \kappa u_*}{\ln\left(\frac{z_2 - d}{z_1 - d}\right)}(\rho_{v2} - \rho_{v1}) \tag{3-143}$$

where ρ_v is the (mean) vapor density and a_v is the ratio of water and momentum von Kármán constants ($a_v \approx 1$ is thought reasonable for practical purposes). The vapor roughness length, z_{0v}, is defined as the zero intercept of $(\rho_{vs} - \rho_v)$ data plotted against $\ln(z - d)$, where ρ_{vs} is the surface value of ρ_v. The relationship for ρ_v when $z - d \gg z_{0v}$ is

$$E = -\frac{a_v \kappa u_*}{\ln\left(\frac{z - d}{z_{0v}}\right)}(\rho_v - \rho_{vs}) \tag{3-144}$$

A similar analysis for sensible heat flux (surface to air), H, yields

$$H = -\frac{a_h \kappa u_* \rho c_p}{\ln\left(\frac{z_2 - d}{z_1 - d}\right)}(\theta_2 - \theta_1) \tag{3-145}$$

where θ is the (mean) potential temperature, a_h is the ratio of heat and momentum von Kármán constants ($a_h \approx 1$ is thought reasonable for practical purposes), and c_p is the specific heat for constant pressure. The heat roughness length, z_{0h}, is defined as the zero intercept of $(\theta_s - \theta)$ data plotted against $\ln(z - d)$, where θ_s is the surface value of θ. For most practical purposes, θ can be replaced by $\bar{T}$ or T for short. The relationship for T when $z - d \gg z_{0h}$ is

$$H = -\frac{a_h \kappa u_* \rho c_p}{\ln\left(\frac{z_2 - d}{z_1 - d}\right)}(T - T_s) \tag{3-146}$$

When considering effects in the canopy sublayer, it is convenient to use the vertical continuity relationship for momentum,

$$-\frac{\mathrm{d}\tau}{\mathrm{d}z} + D_f = 0, \tag{3-147}$$

where τ is the horizontal shear stress and D_f is the momentum sink term (drag experienced by the foliage per unit volume of air. It is generally assumed that shear stress is proportional to velocity gradient through

$$\tau = \rho K_m \frac{\mathrm{d}\bar{u}}{\mathrm{d}z}, \tag{3-148}$$

where K_m is the eddy viscosity [L^2/T].

In the dynamic sublayer, $D_f = 0$, implying τ is a constant, denoted by τ_0. Eliminating $\mathrm{d}\bar{u}/\mathrm{d}z$ from Equation 3-139 and Equation 3-148 yields the relationship

$$K_m = \frac{\kappa \tau_0}{\rho u_*}(z-d) = \frac{\kappa^2 \bar{u}_2}{\ln[(z_2-d)/z_{0m}]}(z-d) \tag{3-149}$$

for K_m within the dynamic sublayer. Eddy diffusivities for vapor and sensible heat may be slightly larger than for momentum, but for practical purposes the differences may be neglected.

In a canopy, D_f is assumed proportional to $\bar{u}^2$ through

$$D_f = \frac{A_f \mathrm{Cd} \rho}{2} \bar{u}^2 \tag{3-150}$$

where A_f is the surface area (both sides) of leaves per unit volume of air and C_d is a drag coefficient. A_f is related to leaf area index (one-sided area of leaves per unit ground surface area) through

$$2LAI = \int_0^{h_0} A_f \, \mathrm{d}z. \tag{3-151}$$

Depending on the assumptions for K_m and $A_f\mathrm{Cd}$, one gets different profiles for velocity. The exponential profile for $\bar{u}$ is obtained by assuming $K_m \propto |\mathrm{d}\bar{u}/\mathrm{d}z|$ and $A_f\mathrm{Cd}$ is constant (essentially a uniform canopy):

$$\bar{u} = \bar{u}(h_0)\exp(-a_w \xi), \tag{3-152}$$

where a_w is an extinction coefficient and $\xi = (h_0 - z)/h_0$. The eddy viscosity relationship for this case is expressed as

$$K_m = K_m(h_0)\exp(-a_m \xi), \tag{3-153}$$

where $K_m(h_0)$ is the value of K_m at h_0 and $a_m = (2a_d - a_w)$ is an extinction coefficient that probably is close to a_d and a_w. Measurements suggest that a_w increases with both canopy density and canopy flexibility. Reported values for a_w are between 0.4 and 0.8 for sparse rigid elements (citrus orchard, wooden pegs, bushel baskets); between 1 and 2 for moderately dense semirigid elements (corn, rice, larch, christmas trees, sunflower, and plastic strips); and between 2 and 4 for dense flexible elements (wheat, oats, immature maize). A series of measurements for maize during a growing season suggest that $a_w \propto h_0^m$, where h_0 is in cm, m is in the range of approximately 1/3 to 1/2, and the proportionality constant is roughly 5 to 6 for $m = 1/2$ and 2.3 for $m = 1/3$. Another analysis suggests that

$$a_w = \frac{A_k h_0}{h_0 - d}, \tag{3-154}$$

where A_k is slightly smaller than or equal to 1. For a dense canopy, $d \approx 2h_0/3$, suggesting $a_w \approx 3$.

Brutsaert (1982) suggests that a workable approximation is to join the canopy sublayer with the dynamic sublayer at h_0, yielding

$$\begin{aligned} K_m(h_0) &= \kappa u_*(h_0 - d + z_{0m}) \\ &= \frac{\kappa^2 \bar{u}_2}{\ln[(z_2 - d + z_{0m})/z_{0m}]}(h_0 - d + z_{0m})\bar{u}(h_0) \qquad = \frac{u_*}{\kappa}\ln\left(\frac{h_0 - d}{z_{0m}}\right) \end{aligned} \tag{3-155}$$

Turbulent transfer of a scalar inert mixture is governed by

$$-\frac{\mathrm{d}F}{\mathrm{d}z} + S_f = 0, \tag{3-156}$$

where F is the vertical specific flux of the mixture and S_f is the source term from the foliage. With the assumption that the profile for a scalar is roughly similar to that of momentum, the eddy diffusivity profile for a uniform canopy is expressed as

$$K_c = K_c(h_0)\exp(-a_s\xi), \tag{3-157}$$

where $K_c(h_0)$ is the value of K_c at h_0 and a_s is an extinction coefficient that is of the same order of magnitude as a_m and a_w. Various values for a_s are reported ranging from 2.2 through 4.25, all for dense canopies. The lowest value is the lowest end of a range for wheat; the highest is for a pine forest. Presumably a_s would be smaller for sparse desert vegetation.

Most of the available information on vegetation is for dense canopies. Claassen and Riggs (1993) examined the roughness length and displacement height for Sonoran desert vegetation, dominated by creosote bush. For these vegetation, they found that $z_{0m} \approx 0.145h_0$, in agreement with Brutsaert (1982) observations, but $d \approx 0$, suggesting that the roughness elements are sparsely

spaced. Further, the roughness elements in the Sonoran desert vegetation were found to be approximately uniformly distributed through the canopy. These results are likely to be fairly typical of vegetation scenarios through those associations likely to be present at YM that are now at lower elevations than piñon-juniper, and perhaps even for piñon-juniper.

Based on the above information, it may be sufficient to simply use a formulation for evapotranspiration that includes only the canopy and dynamic sublayers. This is always adequate when the measurement point is at 1 m elevation above the surface and is adequate under neutral conditions when the measurement point is even as high as 50 to 100 m elevation. There should be relatively little error for a measurement point of 2 m elevation (typical of YM observations) even when the atmosphere is very unstably stratified, although Brutsaert (1982) notes that under stable conditions the logarithmic profile is not representative. The advantage of neglecting stability considerations is that no iteration is necessary to calculate eddy diffusivities.

References

Abramowitz, M. and I. A. Stegun. 1972. *Handbook of Mathematical Functions.* New York, NY: Dover Publications, Inc.

Bear, J. 1979. *Hydraulics of Groundwater.* New York, NY: McGraw-Hill.

Beatley, J. C. 1974. Phenological Events and Their Environmental Triggers in Mojave Desert Ecosystems. *Ecology 55*, 856–863.

Bennie, A. T. P. 1996. Growth and Mechanical Impedance. In Y. Waisel, A. Eshel, and U. Kafkafi (Eds.), *Plant Roots: The Hidden Half*, pp. 453–470. New York, NY: Marcel Dekker, Inc.

Bird, R. B., W. E. Stewart, and E. N. Lightfoot. 1960. *Transport Phenomena.* New York, NY: John Wiley & Sons.

Brutsaert, W. 1982. *Evaporation into the Atmosphere: Theory, History, and Applications.* Dordrecht, The Netherlands: Kluwer Academic Publishers.

Caldwell, M. M. 1994. Exploiting Nutrients in Fertile Soil Microsites. In M. M. Caldwell and R. W. Pearcy (Eds.), *Exploitation of Environmental Heterogeneity by Plants*, Chapter 12, pp. 325–347. San Diego, CA: Academic Press.

Claassen, H. C. and A. C. Riggs. 1993. *An Estimate of the Roughness Length and Displacement Height of Sonoran Desert Vegetation, South-Central Arizona.* Water-Resources Investigation Report 92-4065, United States Geological Survey, Denver, CO.

Fitter, A. H. 1994. Architecture and Biomass Allocation of Root Systems. In M. M. Caldwell and R. W. Pearcy (Eds.), *Exploitation of Environmental Heterogeneity by Plants*, Chapter 11, pp. 305–323. San Diego, CA: Academic Press.

Kozlowski, T. T. and S. G. Pallardy. 1997. *Physiology of Woody Plants* (Second ed.). New York, NY: Academic Press.

McMichael, B. L. and J. J. Burke. 1996. Temperature Effects on Root Growth. In Y. Waisel, A. Eshel, and U. Kafkafi (Eds.), *Plant Roots: The Hidden Half*, pp. 383–396. New York, NY: Marcel Dekker, Inc.

Moreshet, S., B. Huang, and M. G. Huck. 1996. Water Permeability of Roots. In Y. Waisel, A. Eshel, and U. Kafkafi (Eds.), *Plant Roots: The Hidden Half*, pp. 659–678. New York, NY: Marcel Dekker, Inc.

Nobel, P. S. 1996. Ecophysiology of Roots of Desert Plants, with Special Emphasis on Agaves and Cacti. In Y. Waisel, A. Eshel, and U. Kafkafi (Eds.), *Plant Roots: The Hidden Half*, pp. 823–844. New York, NY: Marcel Dekker, Inc.

Sonnenthal, E. L., C. F. Ahlers, and G. Bodvarsson. 1997. Fracture and Fault Properties for the UZ Site-Scale Flow Model. In G. S. Bodvarsson, T. M. Bandurraga, and Y. S. Wu (Eds.), *The Site-Scale Unsaturated Zone Model of Yucca Mountain, Nevada, for the Viability Assessment*, LBNL-40376, Berkeley, CA, pp. 7-1–7-33. Lawrence Berkeley Laboratory.

Waisel, Y., A. Eshel, and U. Kafkafi (Eds.). 1996. *Plant Roots: The Hidden Half* (Second ed.). New York, NY: Marcel Dekker, Inc.

Entries into Scientific Notebook #163 for the period November 16, 1995 to October 1, 1999, have been made by Stuart Stothoff — Randall M. Fedors 10/27/99 for SAS

No original text entered into this Scientific Notebook has been removed — Randall M. Fedors 10/27/99 for SAS

This Notebook appears to comply with QAP-0.01.
E. C. Pearcy
11/3/99

1/12/99 Final version of caprock paper.

The following document is identical in content to a document resubmitted to the Journal of Hydrology. The original document was submitted in March, 1998; two reviewers for the journal provided reviews that raised questions and requested clarification. The reviewer comments were addressed in this document. The document was reformatted to place figures and tables into the scientific notebook numbering scheme, in appropriate locations; no text was otherwise altered. Also, note that the references show up in the reference list at the end of the project section.

THE EFFECT OF VEGETATION ON INFILTRATION IN SHALLOW SOILS UNDERLAIN BY FISSURED BEDROCK

Stuart A. Stothoff, Stothoff Environmental Modeling, Houston, TX 77006, USA[1]
Dani Or, Department of Plants, Soils, and Biometeorology, Utah State University, Logan, UT 84322-4820, USA[2]
David P. Groeneveld, Resource Management, Inc., Telluride, CO 81435, USA[3]
Scott B. Jones, Department of Plants, Soils, and Biometeorology, Utah State University, Logan, UT 84322-4820, USA[4]